GAS SORPTION IN ENGINEERED CARBON NANOSPACES

A Dissertation

presented to

the Faculty of the Graduate School

at the University of Missouri

In Partial Fulfillment
of the Requirements for the Degree

Doctor of Philosophy

by
JACOB W. BURRESS

Dr. Peter Pfeifer, Dissertation Supervisor

AUGUST 2009

The undersigned, appointed by the Dean of the Graduate School, have examined the Dissertation entitled

GAS SORPTION IN ENGINEERED
CARBON NANOSPACES

presented by Jacob Burress, a candidate for the Degree of Doctor of Philosophy, and hereby certify that, in their opinion, it is worthy of acceptance.

_____

Professor Peter Pfeifer

_____

Associate Professor Carlos Wexler

_____

Professor Galen Suppes

_____

Professor Paul Miceli

_____

Professor Haskell Taub

_____

Professor Frederick Hawthorne

I dedicate this thesis to my loving wife, Molly.

Trust in the Lord with all your heart

And lean not on your own understanding;

In all your ways acknowledge him,

And he will make your paths straight.

Proverbs 3:5, 6

ACKNOWLEDGEMENTS

TABLE OF CONTENTS

LIST OF FIGURES

LIST OF TABLES

LIST OF SYMBOLS AND ABBREVIATIONS

Symbol or Abbreviation	Units	Description
AGLARG		Atlanta Gas Light Adsorbent Research Group
ANG		Adsorbed natural gas, typically 500 psig maximum tank pressure
$\alpha(T)$	Å^2 or nm^2	Surface area per site, Area per adsorbed molecule
BET		Brunauer, Emmett, Teller
C		BET constant
CNG		Compressed natural gas, typically 3,600 psig maximum tank pressure
D	Å or nm	Pore dimension (width of slit)
DOE		Department of Energy, United States of America
E_B	kJ/mol	Binding energy
EDS		Energy dispersive spectroscopy
$f(D)$		Relative distribution of pore widths
FESEM		Field emission scanning electron microscopy
h	$6.626 \times 10^{-34}\,\text{m}^2\,\text{kg s}^{-1}$	Planck's constant
HTP-1V		Hydrogen manometric instrument, HTP1-V Mark II, produced by Hiden Isochema
IGA		Hydrogen gravimetric instrument, Intelligent Gravimetric Instrument, produced by Hiden Isochema
k	$1.381 \times 10^{-23}\,\text{m}^2\,\text{kg s}^{-2}\,\text{K}^{-1}$	Boltzmann's constant
LAI		Langmuir adsorption isotherm
LN2		Liquid nitrogen
M_{Ads}	g	Mass of absolute adsorbed gas

M_C	g	Mass of evacuated chamber
$M_{C,G}$	g	Mass of sample cell with gas to be analyzed ($G = H_2$, CH_4) at desired temperature and pressure
$M_{C,S}$	g	Mass of evacuated sample cell with outgassed sample
$M_{C,S,G}$	g	Mass of chamber, sample and gas
M_{Ads}^{Ex}	g	Mass of excess adsorbed gas
M_{H_2}	g	Mass of the H_2 molecule
M_{Mono}	g	Mass of one monolayer of adsorbed gas
MOF		Metal organic frameworks
M_S	g	Sample mass
M_{Stored}	g	Mass of gas stored in the pores, includes both adsorbed and non-adsorbed gas
N		Number of gas admolecules on the adsorbent
N_A		Avogadro's constant
N_{Mono}		Number of admolecules constituting a monolayer
NG		Natural gas
NGV		Natural gas vehicle
NLDFT		Non-local density functional theory
p	bar	Pressure of gas
p_0	bar	Saturation pressure of the gas species in subcritical adsorption (coexistence pressure of bulk liquid/gas at a given temperature)
Pd		Palladium
psi		Pounds per square inch
PSD		Pore size distribution(s)
ϕ		Porosity
ϕ_{Nano}		Nanoporosity
ρ_{Ads}	g/cm^3	Density of adsorbed film
$\rho_{Apparent}$	g/cm^3	Apparent density, all pores included (also referred to as monolith density)
ρ_{Gas}	g/cm^3	Density of the bulk gas (adsorptive)
$\rho_{Skeletal}$	g/cm^3	Skeletal density
$\rho_{Initial}^{ST}, \rho_{Final}^{ST}$	g/cm^3	Densities of the gas in the supply tank before and after adsorption, respectively

$\rho_{\text{Final}}^{\text{TT}}$	g/cm^3	Density of the final gas in the test tank
QSDFT		Quenched solid density functional theory
SEM		Scanning electron microscopy
Σ	m^2/g	Specific surface area for mass sample
T	K	Temperature
TEM		Transmission electron microscopy
$\theta(p,T)$		LAI Coverage
V_{Apparent}	cm^3	Apparent volume, taken as convex hull of monolith
V_{Ads}	cm^3	Volume of the adsorbed film
V_{Nanopore}	cm^3	Volume of nanopores
V_{Skeletal}	cm^3	Skeletal volume
V^{ST}	cm^3	Volume of the supply tank
$V_{\text{TotalPore}}$	cm^3	Total open pore volume
V^{TT}	cm^3	Volume of the test tank
ν_x, ν_y, ν_z	Hz	Vibrational frequencies of admolecule
$V(x,y,z)$	kJ	Adsorption potential at position (x,y,z), where z is the coordinate perpendicular to the surface, and x, y are the coordinates parallel to the surface
$\chi(T)$	bar^{-1}	Langmuir constant

Abstract

Vehicular storage of gaseous fuels is a key enabling technology for the two pillars of a non-petroleum based transportation economy as envisaged under various federal and state alternative fuel plans: 1) natural-gas vehicles (internal combustion engines) and 2) hydrogen fuel cell vehicles—. My research focuses on the development of nanoporous carbons as high-capacity storage materials for natural gas (methane) and molecular hydrogen in on-board fuel tanks for next-generation clean vehicles. The carbons are produced in a multi-step process from corncob, have surface areas of up to 3500 m^2/g, porosities of up to 0.8, and store, by physisorption, exceptional amounts of methane and hydrogen. Adsorbent-based storage materials are attractive due to their low operating pressure (relative to compressed gas), reversibility, ease of fueling, and absence of thermal management issues. Nanopores generate high storage capacities by high surface area to volume ratios, and by hosting deep potential wells through overlapping substrate potentials from opposite pore walls, with binding energies approximately twice the binding energy in wide pores.

The best gravimetric and volumetric storage capacities, among the carbons investigated in this thesis, are 1) 250 g CH_4/kg carbon and 130 g CH_4/liter carbon (199 V/V) at 35 bar and 293 K and 2) 80 g H_2/kg carbon and 47 g H_2/liter carbon at 50 bar and 77 K. This is the first time the DOE methane storage target of 180 V/V at 35 bar and ambient temperature has been reached and exceeded. The hydrogen values compare favorably with the 2010 DOE targets for hydrogen, excluding cryogenic components.

Methane and hydrogen storage capacities were measured on custom-built gravimetric and manometric instruments, and validated on instruments in external laboratories.

To shed light on the mechanisms leading to the exceptional storage capacities attained, extensive characterization of the surface and pore structure of samples was performed. Characterizations include surface areas and pore-size distributions from nitrogen adsorption at 77 K (subcritical adsorption, <1 bar); pore-size distribution from methane adsorption at 293 K (supercritical adsorption, <35 bar); spatial organization of pores from small-angle x-ray scattering, scanning electron microscopy, and transmission electron microscopy; and chemical composition from energy-dispersive x-ray spectroscopy. Surface areas and pore volumes in selected intervals of pore size were correlated (a) with process parameters for the carbon production, and (b) with methane and hydrogen storage capacities, to identify carbon production procedures that lead to superior storage capacities.

For hydrogen, surface areas and pore volumes were used to convert experimental storage isotherms into surface coverage. Results were compared with statistical mechanical models for supercritical adsorption of hydrogen on carbon surfaces and with molecular dynamics simulations. From fits of the experimental coverage to the theoretical coverage, key parameters controlling adsorption at the atomic level—such as binding energies and the nature of adsorption sites—can be deduced. In two case studies, it was found that 40% of surface sites reside in pores of width ~0.7 nm and binding energy ~9 kJ/mol, and 60% of surface sites reside in pores of width >1.0 nm and binding energy ~5 kJ/mol. The findings, including the prevalence of only two distinct binding energies, are in excellent agreement with results from molecular dynamics simulations. It

was furthermore found that we can experimentally distinguish between the situation in which molecules do (mobile adsorption) or do not (localized adsorption) move parallel to the surface, how such lateral dynamics affect the hydrogen storage capacity, and how the two situations are controlled by the vibrational frequencies of adsorbed hydrogen molecules parallel and perpendicular to the surface: in the two case studies, adsorption is mobile at 293 K, and localized at 77 K. These findings support the hypothesis that hydrogen storage capacities in nanoporous carbons can be optimized by suitable engineering of the nanopore space and demonstrate potential engineering methods.

Chapter 1: Motivation and Research Problem

1.1 Motivation

In recent years, the search for inexpensive, abundant energy sources has been a prominent public policy concern. The challenges of energy shortages, greenhouse gases and air pollution have compelled the public and private sectors to invest in the development of alternative energy sources. The U.S. Department of Energy (DOE) has mandated a transition from conventional sources of energy (fossil fuels, uranium) to non-conventional sources (biofuels, non-fossil natural gas, hydrogen) [1]. There is broad consensus that the use of a combination of these non-conventional fuel sources will be required to meet energy demand[2].

The transportation sector is a major consumer of energy in the U.S., constituting 29.1% of energy consumption in 2007, see figure 1.1.1. Therefore, alternative fuel research for vehicular use has become a keystone in the future U.S. energy economy. According to the State Alternative Fuels Plan of the California Air Resources Board and California Energy Commission, adopted October 31, 2007, in response to Assembly Bill 1007, the State of California will take action to increase its use of natural gas (NG, methane, CH_4) as motor fuel from 0.6% to 19% (aggressive scenario) of the state's on-road transportation fuels by 2050 [3, 4]. According to the 2006 Hydrogen Posture Plan [5] of the DOE and U.S. Department of Transportation, a projected 37% of light-duty vehicles in the U.S. will be hydrogen fuel cell vehicles by 2050.
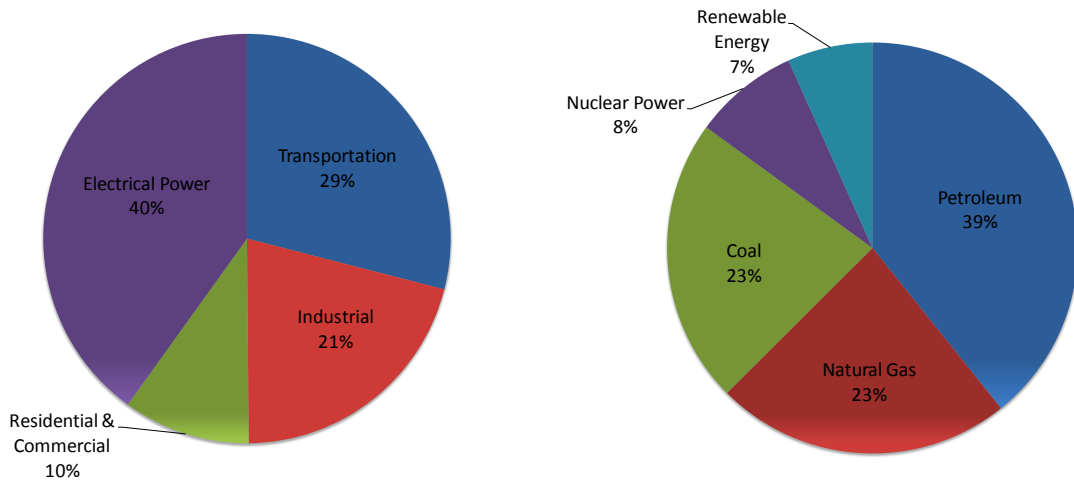
Figure 1.1.1. Breakdown of 2007 U.S. Energy consumption by sector on the left and by source on the right [6].

Hydrogen and methane both meet the "No Net Material Increase in Emissions" standard [5-8]. In other words, NG vehicles produce no ozone or smog, and up to 40% less greenhouse gases than gasoline or diesel vehicles. NG can reduce the US' dependence on foreign oil (85% of the NG consumed in the US is produced domestically; 12% comes from Canada). It is cheaper than gasoline or diesel at the pump, and can also be produced from renewable sources in the form of biomethane (e.g. from landfills, sewage treatment plants, manure).

A substantial number of natural gas vehicles are currently in circulation in the U.S., predominately in use as municipal fleet vehicles. However, most current natural-gas vehicles run on compressed natural gas (CNG), with on-board NG stored in bulky, heavy-walled cylinders at 250 bar (3600 psig). Likewise, hydrogen fuel cell vehicles under development store hydrogen in cylinders at 350-700 bar. Such high-pressure tanks are difficult to integrate within the space available in a passenger car and deliver limited fuel storage capacity, limiting driving range. On-board storage constitutes a major barrier

to the use of NG and hydrogen for advanced transportation and to the transition to non-petroleum transportation fuels.

The development of a viable hydrogen-based economy depends on overcoming numerous scientific and technological barriers. In particular, for vehicular use, the DOE has identified three major challenges to the successful adoption of hydrogen-powered vehicles [7]:

- Hydrogen production costs must be substantially lowered (and long-term renewable sources for the energy required for its production must be identified and developed);

- Fuel cell costs must be substantially reduced (Using hydrogen in internal combustion engines significantly lowers their efficiency, compounding problems for production and storage);

- Onboard hydrogen storage systems must be capable of delivering a driving range of 300 miles (~500 km) without major detrimental effects to vehicle cost, safety or cargo capacity.

Of the three challenges, perhaps the most difficult to solve is the development of on-board storage due to the various constraints imposed on the system (e.g. cost and safety, volume and mass limitations, operation in a wide range of temperatures, charging times, reusability of the materials).

At ambient conditions, unlike liquid gasoline- or alcohol-based fuels, hydrogen gas exhibits very low energy density per unit volume. Traditionally, this issue was solved either by liquefaction at cryogenic conditions (e.g., as used in spacecraft),
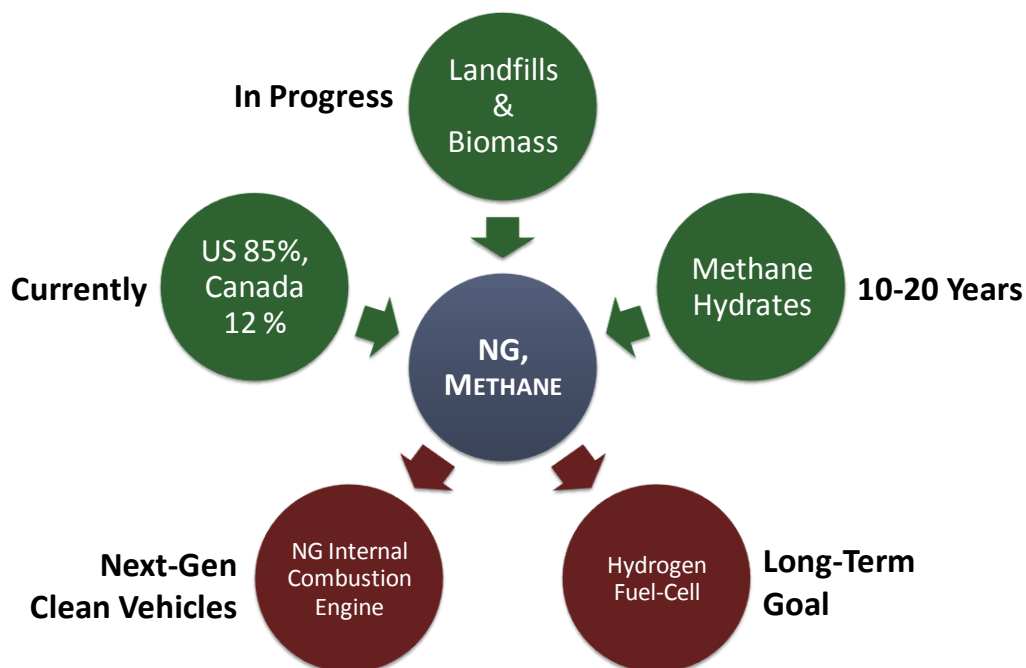
Figure 1.1.2. Sources and uses for natural gas.

or by storing the gas at very high pressures (e.g., as used in some test vehicles). In addition to the practical difficulties of storing hydrogen at extreme conditions, a significant amount of energy is lost during liquefaction or compression (~1/3 and ~1/5 of the heating value of H_2). Adsorbent-based storage materials, therefore, show promise because of their reversibility, ease of fuelling, and absence of thermal management issues. However no material presently comes close to the 2010 DOE storage targets of 60 g H_2/kg tank and 45 g H_2/liter tank at low-pressure, room-temperature conditions.

To meet the DOE's hydrogen storage goals, the hydrogen-carbon binding energy on nonporous carbon, ~5 kJ/mol, must be improved [8]. Significantly higher storage can be achieved in activated carbon by surface functionalization: (a) via creation of nanometer-sized pores which dramatically raise the surface area for adsorption (3,000 m2/g, or more) and create deeper potential wells (almost doubling the adsorption energy) [9]; and/or (b) by doping with elements capable of strengthening the hydrogen-substrate

interaction (e.g. boron, iron, nitrogen, intercalated fluoride ions, platinum and palladium)[9-11].

For both fuels, the optimal, on-board tank [8, 10] is a lightweight, flat-panel (conformable) tank, positioned under the floor or in another unused space of an automobile, with driving range of more than 300 miles, capable of refueling in less than 3 minutes, and requiring minimal auxiliary on/off-board equipment and infrastructure.

1.2 Statement of Research Problem

The objective of my research as part of the Alliance for Collaborative Research in Alternative Fuel Technology (ALL-CRAFT, http://all-craft.missouri.edu/) is to replace bulky cylindrical, heavy-walled compressed gas tanks (3600 psi) with a flat, lightweight tank for adsorbed gas storage (500 psi). The flat tank design, made possible by the low pressure in the adsorbed gas tank, is a critical design feature that enables the tank to be mounted under the floor or in other unused space of a car. The tank will make natural gas and hydrogen vehicles a widely attractive, practical, clean alternative to gasoline or diesel vehicles. Low storage pressure also reduces fueling costs. Tank pressure of 500 psi is equivalent to pressure in natural gas pipeline pressure, eliminating the need for costly compression of natural gas from 500 psi to 3600 psi an is necessary for compressed natural gas tanks.

The uniqueness of the ALL-CRAFT project is that it brings together researchers from chemistry, chemical engineering, mechanical engineering and physics disciplines. Novel experimental methods were used in this project and were further developed upon as the project advanced to both improve accuracy as well as capability in material characterization and to increase the understanding of the physical nature of the gas-

surface system. This project will answer outstanding questions about the physisorption of methane and hydrogen. These questions include the following:

- Is corncob a superior precursor for carbon production for purposes of adsorbed gas storage?

- How does surface area affect gas uptake?

- Which pore width ranges result in the highest capacity for methane and hydrogen uptake? Are adsorbed hydrogen molecules characterized by localized or mobile (i.e. free to move on the surface) sorption?

- Can the area that an adsorbed hydrogen effectively occupies on a carbon surface be determined experimentally?

- Can the 5 kJ/mol binding energy of hydrogen to graphite be improved through the engineering of carbon nanospaces?

Chapter 2 reviews previous research that informs the investigation of physisorption and the use of activated carbon as a storage medium. Chapter 3 introduces a theoretical framework that allows for the development of testable hypotheses regarding material synthesis, activation and optimization of storage materials. Chapter 4 details the microscopy, compositional and sorption measurement methods used in hypothesis testing. Experimental results are presented in Chapter 5. Chapter 6 draws conclusions regarding pore structure, optimization of engineered storage materials and experimental determination of adsorption physics. Chapter 7 specifies several avenues for future research.

Chapter 2: Background

2.1 Physisorption for Methane and Hydrogen Storage

Gas sorption has been used throughout the years in many practical ways: gas separation; drying processes of gases and solid materials; cleaning processes of air, water, and soil; adsorption based energetic processes; air-conditioning refrigerating processes; gas storage processes; and the characterization of porous solid materials. The research presented will concentrate on gas storage processes and characterization of porous materials [11].

There is a wide range of materials that have been explored for physisorbed gas storage: carbons, zeolites, silicas, calixerines, metal organic frameworks (MOF), are amongst them. In recent years, carbons and MOF's have been singled out as some of the best materials for gas storage [12-15]. In order for a material to be useful as a gas storage material, the sample characteristics need to be optimized and balanced as necessary. Some of these characteristics include, but are not limited to:

- Non-prohibitive cost,
- High mass of gas stored for mass of material,
- High mass of gas stored for volume of material,
- Reversibility,
- Durability,
- Fast gas kinetics.

The necessity for these attributes is reflected in U.S. Department of Energy's hydrogen storage goals, see table 2.1.1. The optimization of these characteristics is typically rather complicated, and research must be conscientious of these qualities during material design and synthesis. An example of one complication that arises is the relationship between the mass stored for mass of the material and the mass stored for volume of the material. The mass of gas stored for mass material depends inversely on the apparent density of the sample; whereas the mass of gas stored for volume of material depends directly on the apparent density of the sample. Therefore, modifying the sample's apparent density to improve one of these values will be at the cost of the other. Similar situations will most certainly arise as each of these properties is optimized.

Table 2.1.1. Summary of DOE targets for hydrogen as of March 24, 2009 [16].

	2010	2015	Ultimate
System gravimetric capacity (g H_2/kg system)	45	55	75
System volumetric capacity (g H_2/L system)	28	40	70
Storage system cost ($/kg H_2 stored)	133	67	TBD
Min/max delivery temperature (°C)	-40/85	-40/85	-40/85
Cycle life, 0.25 tank to full (# of cycles)	1000	1500	1500
Minimum delivery pressure, fuel cell (atm*)	4	3	3
Minimum delivery pressure, internal combustion engine (atm)	35	35	35
Maximum delivery pressure (atm)	100	100	100
System fill time (kg H_2/min)	1.2	1.5	2.0

*1 atmosphere ≈ 1.013 bar

The DOE has not generated goals for the storage or delivery of methane since 2001. Despite, the lack of specific guidance from the DOE, the storage of methane still remains an area of large interest to the private sector. For a comparison of the methane and hydrogen storage goals, see table 2.1.2. In 2001, the DOE used one measure of

8

methane storage that it did not continue to use for later hydrogen storage goals. This measure is the volume of gas stored for volume of material. This quantity uses the density of the gas at laboratory reference pressure and temperature, 1 bar and 298 K. There are two ways to understand this quantity. First, it is used to calculate the size of an enclosure at 1 bar and 298 K necessary to store the same amount of gas as in the sample. Second, if the gas is assumed to be ideal, it reveals the pressure at which an equivalent volume would have to be pressurized in order to store the same amount of gas. For example, if the volume stored for volume sample were 180, in order to store the equivalent amount of gas that was stored in a 1 liter container, it would take a 180 liter container at 1 bar and 298 K or a 1 liter container at 180 bar and 298 K.

Table 2.1.2. Summary of DOE targets for methane (2001) and hydrogen (2010).

	Mass of gas stored for mass sample*	Mass of gas stored for volume sample*	Volume of gas stored for volume of sample
Methane: DOE 2000 target, 35 bar and 298 K	-	117 g/L	180 L/L
Hydrogen: DOE 2010 target, 293 K	45 g/kg	28 g/L ‡	344 L/L †

*Hydrogen targets are for tank, not sample, †Not an actual DOE storage goal, value calculated from ‡ using the density of hydrogen at 1 bar and 298 K.

The DOE's funding of natural gas storage research led to the institution of many research groups in academia, private sector, and government, see table 2.1.3. In 2001, no group had yet met the DOE storage goal. Additionally, the low comparative cost of gasoline to natural gas in the late 1990s led to a weakening of public and private interest in natural gas research. These circumstances, combined with the lack of funding from the DOE, led to many of these groups discontinuing methane research and the closure of some of the groups.

Table 2.1.3. Comparative characteristics of large ANG projects up to 2006 [14].

Parameters and Conditions	AGLARG (Atlanta Gas Light Adsorbent Research Group)	EU FP5 LEVINGS program (coordination by FIAT)	Oak Ridge National Laboratory (ORNL)	Honda Motors	University of Petroleum China (UPC)		Brazilian Gas Technology Center (CTGÁS)
Years	1990-1999	1997-2000	?-2000	From 2000	1994-1995		From 2000
Investigation Method	Chrysler B-van, Dodge Dakota Truck	FIAT Marea, On-board, field testing	Laboratory Investigations	Tank development Adsorbent laboratory tests	Car XIALI 713IU On-board, field testing		Laboratory investigation on full-size prototype
Pressure (bar)	35-40	35-40	35	35	50	125	35-40
Tank Uptake V/V (mL/L)	150 in lab, 142 onboard	123	150	155	100-110	170-180	130-150
Tank Delivery V/V to Engine	~135	107	-	-	-	-	-
Adsorbent presumed cost	Prohibitive	High, but about 10 times less than AGLARG	Supposedly very high	Supposedly similar to AGLARG	-	-	-
Vessel (tank) design features	Multicell of extruded aluminum	Multicell of steel tubes	Small laboratory vessel of volume 0,05 L.	Multicell	-	-	Cylindrical form with volume 30 liters

In April 2004, the DOE Energy, Efficiency and Renewable Energy division (DOE-EERE) established three Hydrogen Storage Centers of Excellence, with a fourth having been in 2009. The four centers are the Hydrogen Sorption Center of Excellence, Chemical Hydrogen Storage Center of Excellence, Metal Hydride Center of Excellence and, most recently, the Hydrogen Storage Engineering Center of Excellence. Each center
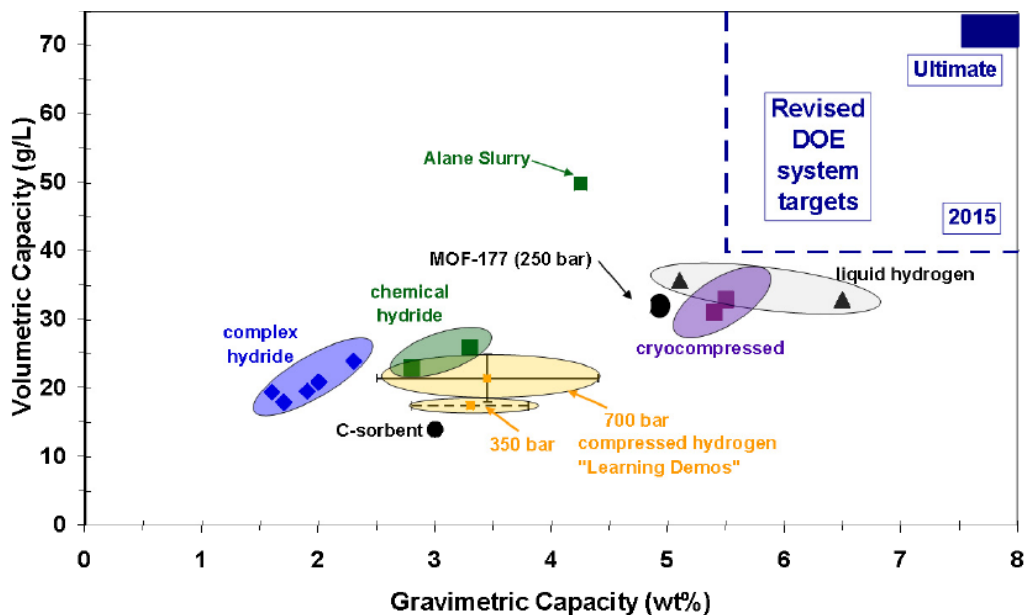
Figure 2.1.1. Summary of hydrogen sorption materials as of 2009 DOE Annual Merit Review Meeting [16].

is comprised of research groups in academia, government laboratories and the private sector. ALL-CRAFT, see section 2.3, became a member of the DOE Sorption Center of Excellence in 2008.

2.2 Activated Carbons for Gas Storage

One class of materials showing continued potential as methane and hydrogen gas storage media is activated carbon. Carbon-based materials, due to their low cost and weight, have long been considered as suitable physisorption substrates for the reversible storage of gases. Activated carbons are typically amorphous carbons produced from either lignocellulose (plant) material, coal, or pyrolyzed polymers. These starting materials (precursors) are either activated chemically (hydrochloric acid, potassium hydroxide, amongst others) or physically (steam, carbon dioxide, amongst others). Two distinctive characteristics of activated carbons are the large amount of micropores and the resulting large surface areas (500-3500 m^2/g). Both of these attributes make activated

11

carbon attractive as a gas storage media. Additionally, if the gas being stored is properly purified of other gases before entering the storage tank, activated carbons are very durable throughout repeat loading and unloading of gases. Furthermore, the distribution of pore sizes and the ability to control the pore size distribution through various activation parameters provides activated carbons good gas kinetic properties.

There have been several groups that have produced activated carbons for the exploration of their storage capabilities for both methane [17-20] and hydrogen [21, 22] gases. These carbons, however, did not meet the DOE goals for natural gas or hydrogen. The binding energy of methane with carbon is high enough, ~15 kJ/mol [23], that the storage goals can be met through modification of the pore structure alone. For hydrogen storage, however, the binding energy between hydrogen and carbon is too low, ~5 kJ/mol [24], for simple modification of the pore structure to be sufficient to reach the storage goals. Therefore, it has been predicted that the doping of the activated carbon with molecules that have a higher hydrogen binding energy, e.g. boron, will be necessary.

2.3 ALL-CRAFT

In 2002 Pfeifer et al. [25] discovered nearly space-filling fractal networks of carbon nanopores in certain activated carbons made from olive pits. These carbons were activated using steam activation. Dr. Pfeifer proposed that modifying the hierarchical nature of the carbons could dramatically increase the gas uptake. The Alliance for Collaborative Research in Alternative Fuel Technology was created in October of 2004 to investigate hierarchical, activated carbon for methane storage. ALL-CRAFT is a partnership between the University of Missouri, the Midwest Research Institute, the

Figure 2.3.1 Overview of methane project with depiction of carbon manufacture process starting with waste corncob. Image Courtesy of the National Science Foundation, by Nicole Rager Fuller.

National Renewable Energy Lab and other groups in academia and the private sector.

Prior to ALL-CRAFT, the assumption was that the carbon precursor needed be a high density material, e.g. olive or peach pits. In the ALL-CRAFT project, corncob was chosen because it is an abundant raw material native to the Midwest. The novel activated carbons were produced in Dr. Galen Suppes' laboratory in the Chemical Engineering Department at the University of Missouri. The chemical engineering group has made significant progress with these new activated carbons. Additionally, a different method of activation was chosen. Instead of steam activation, the primary method for activation was through the use of potassium hydroxide (KOH). The use of KOH for carbon activation is well-founded [26-32] for a variety of precursor materials. As will be seen later in this paper, the carbons proved highly successful for methane storage. As part of

the early methane project, a fleet vehicle in Kansas City was retro-fitted with an adsorbed natural gas (ANG) tank utilizing the carbon produced from corncob, see figure 2.3.2.

Furthermore, with the outstanding interest of the DOE in hydrogen storage, the project started looking at these carbons for hydrogen storage as well. Due to limitations of carbon as a hydrogen storage material, ALL-CRAFT has expanded its research to include the doping of carbon materials with boron and the exploration of the effect of other impurities.

Figure 2.3.2 Kansas City fleet vehicle (left) using carbon monoliths produced from waste corncob as ANG storage.

Chapter 3: Conceptual Framework

3.1 Interaction of Gases with Solid Surfaces

3.1.1 Intermolecular forces

The forces near the surface of a solid can take many forms, e.g. London dispersion forces and dipole interactions amongst others. The sum of all the attractive forces between the gas molecules and the solid surface is the van der Waals interaction (force). These attractive forces are able to condense gases into high density film layers. The characteristic strength of the gas-surface interaction is called the binding energy, E_B. The binding energy depends on molecular species involved as well as geometry of the surface [33].

The sum of the repulsive and attractive forces between two atoms is often approximated by the Lennard-Jones 12-6 potential, typically given in the form

$$\Phi_{12-6}(z) = 4\varepsilon\left[\left(\frac{\sigma}{z}\right)^{12} - \left(\frac{\sigma}{z}\right)^{6}\right], \tag{3.1}$$

where ε is the depth of the potential well and σ is the interparticle distance at which the potential is zero, see figure 3.1.1 [33, 34]. In principle the magnitude of the depth of the potential well should always be larger than the binding energy of the gas with the surface. This is because the quantum mechanical ground state needs to be taken into consideration in order to determine the actual binding energy from the depth of the potential well. Additionally, the potential given by (3.1) is only for two interacting particles. When multiple particles are involved, the potential will be the sum of all the interactions. For
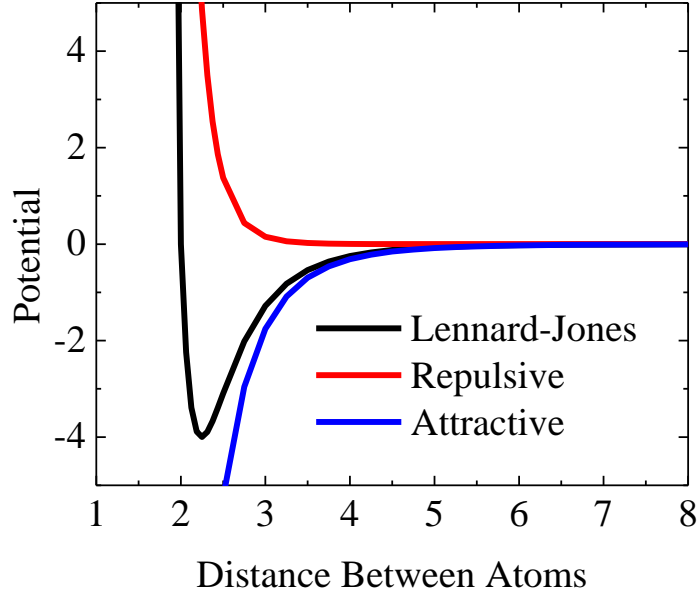
Figure 3.1.1. Plot of a model Lennard-Jones potential as well as its attractive and repulsive parts, with ε of 4 and σ of 2.

the interaction of a gas molecule and the surface of a graphene sheet, the interactions

between all the carbon atoms and gas molecule need to be taken into consideration. For a

gas molecule interacting with a solid surface (treating the solid as continuous and with

semi-infinite thickness), the potential is given as [34]

$$\Phi_{9-3}(z) = \frac{2}{3}\pi n \sigma_{GS}^3 \varepsilon_{GS} \left[\frac{2}{15}\left(\frac{\sigma_{GS}}{z}\right)^9 - \left(\frac{\sigma_{GS}}{z}\right)^3 \right]. \tag{3.2}$$

Equation (3.2) often referred to as the Lennard-Jones 9-3 potential. In equation (3.2) z is

the perpendicular distance between the gas molecule and the solid, n is the number

density of the solid, σ_{GS} is the finite distance between the solid and the gas molecule

where the potential is zero, and ε_{GS} is the depth of the potential. The attractive part of

the potential drops off as $\Phi(z) \propto z^{-3}$ compared to $\Phi(z) \propto z^{-6}$ for two interacting particles.

When only a single sheet of solid atoms are taken into account (e.g. a single sheet of graphene), the potential drops off as $\Phi(z) \propto z^{-4}$ [34].

Using Lennard-Jones potentials to model the surface of the graphene can provide information about the approximate binding energy of gases with the surface, as well as the frequency of vibrations of an atom in the adsorbed layer. This will be used in later sections to determine values needed for the isotherm fitting routine to ascertain the binding energy of hydrogen molecules in the carbon nanospaces.

3.1.2 Physisorption Modeling

When modeling the adsorption of gases onto solid surfaces, the gas-solid system is broken down into a 3 phase approximation. These phases are the adsorbate, adsorptive and adsorbent, see figure 3.1.2 [33]. The adsorbate is the gas in the adsorbed phase; the adsorptive is the non-adsorbed (bulk) gas; and the adsorbent is the solid material. The adsorption of gases, gas molecule transitioning from adsorptive to adsorbate state, is an exothermic process; whereas the desorption of gases, gas molecule transitioning from adsorbate to adsorptive state, is an endothermic process.

There are several schools of thought as to how adsorbates should be classified [11, 33]. Ultimately, each of these classifications falls into one of two categories: monolayer or multilayer adsorption. Monolayer sorption is characterized by the formation of only a single layer of adsorbate film. One example of when monolayer sorption occurs is when the adsorbate-adsorbent interactions are large compared to the adsorbate-adsorbate interactions. Multilayer sorption is characterized by the formation of multiple layers of adsorbate film. One example of multilayer adsorption is when the
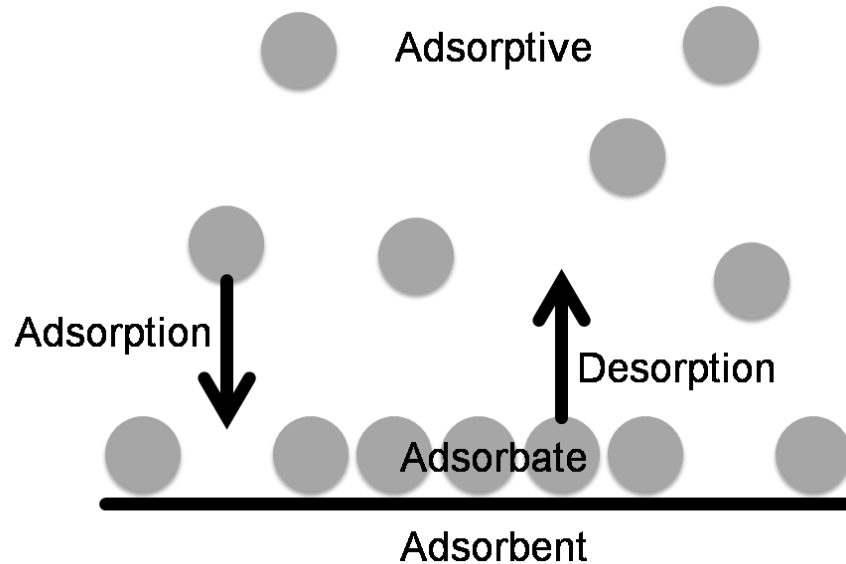
Figure 3.1.2. Three phase approximation for adsorption.

adsorbate-adsorbate interaction is comparable in strength to the adsorbate-adsorbent interaction.

For subcritical gases, this monolayer sorption occurs when the gas pressure is well below the liquid-gas transition pressure for the given temperature, p_0, also referred to as the the saturation pressure. Additionally, as the pressure is brought up from vacuum, and the adsorbate film begins to form; the adsorbate molecules are assumed to have liquid density. As the pressure is increased, multiple layers of adsorbate will begin to form, multilayer sorption. When the gas pressure approaches the liquid-gas transition pressure the number of adsorbate layers grow quickly and can be approximated as approaching infinity.

Supercritical gases are almost exclusively monolayer adsorbates. In this scenario, the adsorbate-adsorbent interaction is generally significantly stronger than the adsorbate-adsorbate interaction. Additionally, the binding energy is normally not strong enough to hold multiple layers adsorbed. In contrast to subcritical gases, the adsorbate does not

form as liquid density film. The admolecules are assumed to be spread over the surface. As the pressure of the system is increased, the density of the adsorbed monolayer will increase.

3.1.3 Sorption inside Pores

One final aspect of sorption to be discussed is the effect on the adsorbate-adsorptive interaction due to small pores. These pores can take many shapes, although they are generally assumed or approximated as either slit or cylindrical in shape. Activated carbons used in this research are assumed at small length scales, on the order of nanometers, to be made of parallel sheets of graphene, in other words, slit-shaped, see figure 3.1.3. Pore size is denoted by the pore dimension, D, which for cylindrical pores is the pore diameter and for slit-shaped pores is the distance between the pore walls. Pores are divided into three primary categories, determined by their pore dimension: micropores ($D \leq 2nm$), mesopores ($2nm < D \leq 50nm$), and macropores ($D > 50nm$). These pore dimensions are defined such that mesopores include the pore dimensions for which
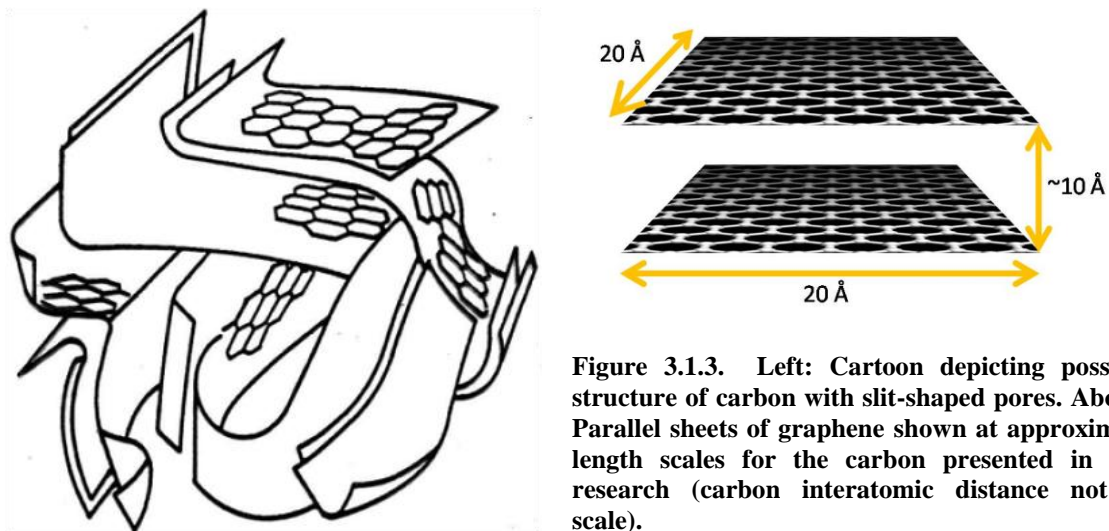
Figure 3.1.3. Left: Cartoon depicting possible structure of carbon with slit-shaped pores. Above: Parallel sheets of graphene shown at approximate length scales for the carbon presented in this research (carbon interatomic distance not to scale).

capillary condensation can occur [33]. Additionally, for the purposes of this research, an additional category of nanopores ($D < 1nm$) will also be considered.

Narrow, slit-shaped pores can have two noticeable effects on the sorption of gases. First, the van der Waals potentials from both sides of the pore superimpose and the binding energy will increase. Therefore, the narrower the pore is, the higher the cumulative binding energy from both surfaces. Assuming that the pore is narrow as to only allow one layer of gas to adsorb, the binding energy can be approximated as almost twice the binding energy of one surface. For supercritical adsorptives, a higher binding energy will result in a higher adsorbate density.

Second, narrow pores will physically limit the number of adsorbate layers. As can be seen in the adsorbed methane depicted in figure 3.1.4 for methane, the pore width plays an important role in both the density of the adsorbate as well as the number of layers that are able to become adsorbed. Although a 6 Å pore has the highest density adsorbate due to the higher binding energy, it does not have the highest number of adsorbate molecule for volume or for mass. Additionally, a 22 Å is wide enough to contain methane in both the adsorbate and adsorptive phases.

For the purposes of gas storage, the optimum pore will be one that fits the most layers of adsorbate at the highest density. The optimum pore dimension for methane at

Figure 3.1.4. Cartoon depicting methane molecules adsorbed in slit-shaped carbon (black) pores of different width. The width of a methane molecule is ~3.7 Å. Pore widths are ~6 Å (above left), ~11 Å (above right), and ~22 Å (left). Note molecule (lighter in shade) in the adsorptive state in the middle of the 22 Å pore.
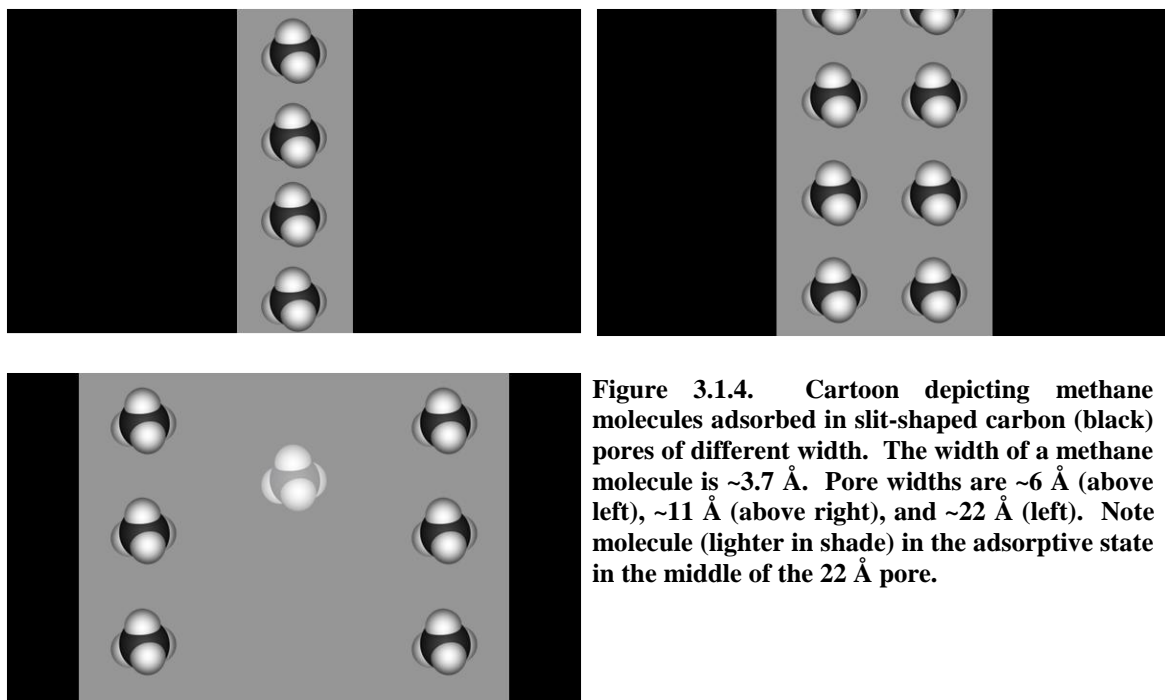
room temperature in carbon from molecular simulations was found to be 1.1 nm [35]. It could be assumed that the optimum pore width for hydrogen will be smaller than the value for methane since hydrogen is a smaller molecule, ~2.4 Å width. If the hydrogen is assumed to form only one adsorbed layer on each carbon surface, this would lead to an optimum pore width of ~7Å, i.e. two adsorbed layers. However, if some recent simulations prove correct, hydrogen at 77 K may form three adsorbed layers in pores of width ~11 Å, with the middle layer being less dense, see figure 3.1.5. If this is correct, then a pore width of ~11 Å will be the optimum pore width for methane at room temperature and hydrogen at 77 K.

Finally, for subcritical gas sorption, for example sub-atmospheric nitrogen sorption at 77 K, the width of the pore will determine at what pressure the pore will be
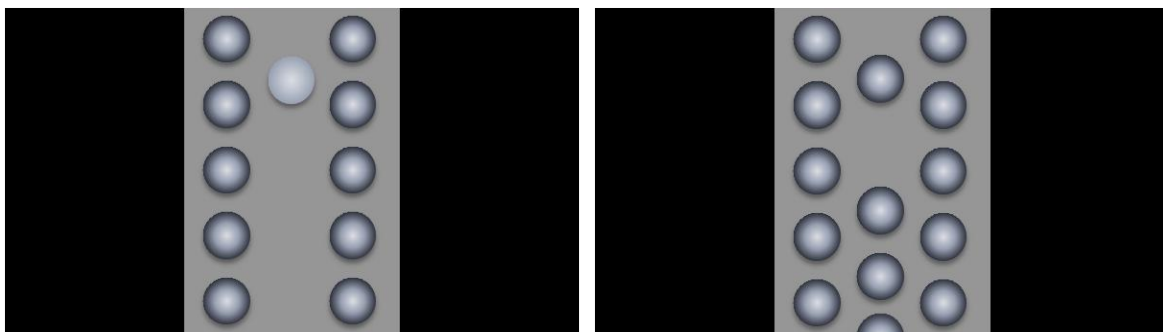
Figure 3.1.5. Cartoons depicting 77 K hydrogen molecules adsorbed in slit-shaped carbon (black) pores of width ~11 Å. The width of a hydrogen molecule is ~2.4 Å. Left: Only one layer adsorbed on each surface, note molecule (lighter in shade) in the adsorptive state in the middle. Right: Three total layers adsorbed, with a less dense middle layer.

filled. Therefore, the pore size will affect how the sorption isotherm needs to be analyzed. The International Union of Pure and Applied Chemistry (IUPAC) have devised an isotherm classification system of six different categories [36]. However, for this research attention will concentrate on type I and type IV isotherms. Although supercritical gas sorption isotherms are generally type I isotherms, these six categories are most useful when applied to subcritical gas sorption. Additionally, for some materials, capillary filling will result in a hysteresis between the adsorption and desorption branches. The hystereses have been classified into four groups; denoted H_1, H_2, H_3, and H_4. For this research, only type H_4 hystereses have been seen.

A type I isotherm rises very steeply and then plateaus. This is indicative of highly microporous samples. It has been recommended to subdivide type I isotherm into two categories: type Ia and Ib [33]. A type Ia isotherm occurs for samples that predominantly have small micropores, i.e. nanopores. For nanoporous materials, the strong binding due to the two slit walls being close together dominates the adsorption. These pores can fit at most two layers of adsorbate. This means that the nanopores will be filled at very low

22
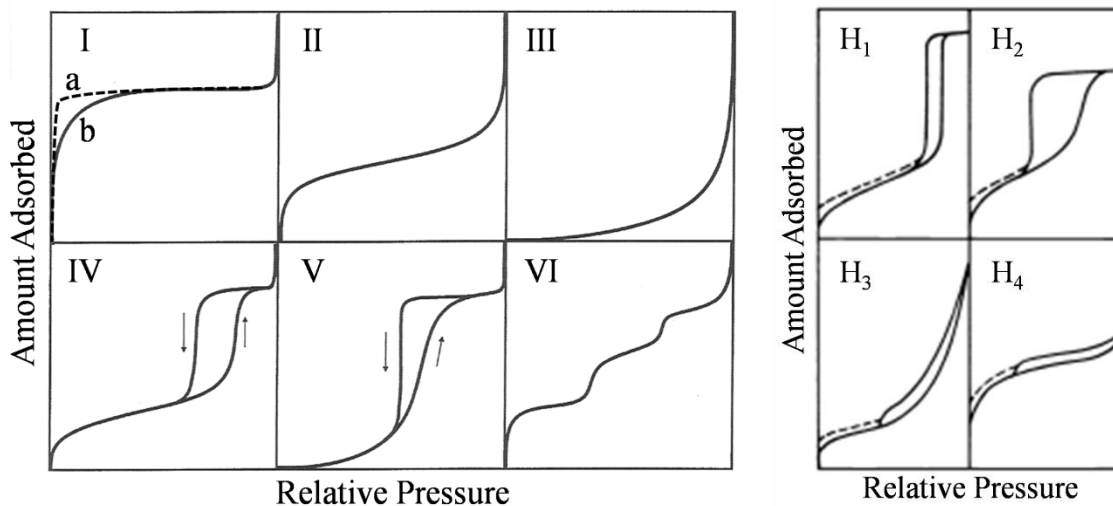
Figure 3.1.6. Left: six main categories of isotherms as determined by IUPAC. Isotherms of primary consequence for this research are type I and IV. Also note the two subcategories of the type I isotherm, labeled a and b. Right: four categories of hysteresis loops as determined by IUPAC. Only hysteresis loop encountered in this research is type H₄. Source: adapted from Rouquerol et. al. [33].

pressures. This effect is called primary micropore filling. A type Ib isotherm, however, generally occurs for microporous samples with larger micropores ($1nm < D < 2nm$). In these samples, the adsorbate-adsorbate interactions start to have more influence on the gas behavior. This is often called cooperative micropore filling. Furthermore, a true type I isotherm will not display a hysteresis in its adsorption-desorption branches.

The other isotherm category of consequence for this work is a type IV isotherm. These isotherms occur for sorption in mesoporous samples. The fundamental aspect of a type IV isotherm is that it will generally display a hysteresis between the adsorption-desorption branches, as seen in figure 3.1.6. A type IV isotherm displaying a type H₄ hysteresis is indicative of a micro/mesoporous material with slit-shaped pores. The hysteresis is due to capillary filling and depletion.

23

3.2 Langmuir Theory of Gas Adsorption

Three adsorptive theories will be used to analyze the experimental results of this project: the Langmuir theory; Brunauer, Emmett, Teller (BET) theory and density functional theory (DFT). The Langmuir theory of gas adsorption is the least complex of the three models and was first published in 1918 [37]. This model is based on four assumptions:

1. There are a fixed number of sites on which gas adsorption may occur,

2. Monolayer adsorption, one admolecule per site,

3. Surface is energetically homogeneous, and

4. The only interactions are between the gas and the surface, no gas-gas interactions.

The Langmuir Adsorption Isotherm (LAI) equation, statistical mechanical model derived from the Hamiltonian of a system with the above assumptions, is given by

$$\theta(p,T) = \frac{\chi(T)p}{1+\chi(T)p},$$

$$0 \le \theta \le 1,$$

(3.3)

where θ is the coverage of the monolayer adsorbate given as the fraction of sites occupied by admolecules, p, is the pressure of the system, and $\chi(T)$ is the temperature dependent Langmuir constant. This equation yields an IUPAC type I isotherm.

The coverage can only have values ranging from 0 to 1 representing no adsorbate and a full monolayer of adsorbate respectively. The Langmuir constant is also referred to as the Henry's law constant as it gives the slope of the linear behavior of the isotherm at low pressures. The Langmuir constant incorporates the strength of adsorbate-adsorbent interaction. As a consequence, a larger adsorbate-adsorbent interaction leads to a larger
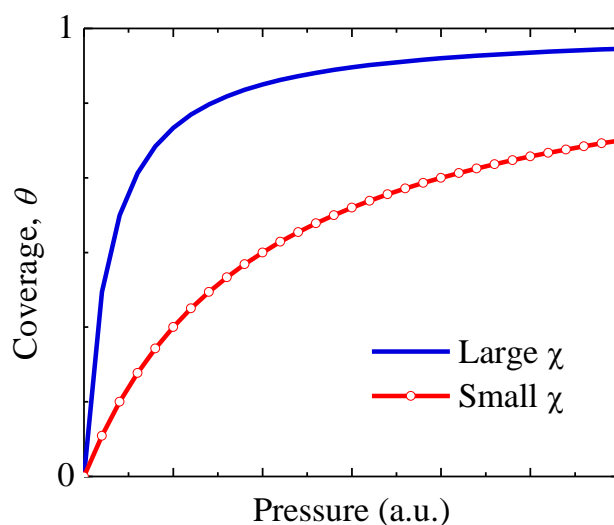
Figure 3.2.1. LAI's showing the χ dependence of the coverage. A larger χ value will lead to a more steeply rising isotherm.

χ value, and which produces a steeper isotherm, see figure3.2.1.

There are two different scenarios of adsorbate behavior on the sorbent surface: localized and non-localized (mobile). Despite the homogenous assumption of the Langmuir theory; empirically, the two models are understood in regards to a sorbent with a heterogeneous interaction potential. If the energy of the adsorbate is less than or comparable to the depth of the energy well, see figure 3.2.2, the adsorbate molecule will be bound in the well and will therefore be localized on the surface. If the adsorbate molecule has an energy comparable to the depth of the potential, then it will be able to move from one well to the other, but will still generally be localized in one site. If, however, the adsorbate molecule has energy higher than the sorbent potential, then it is free to move along the surface unhindered. These two distinct models—localized adsorption and mobile adsorption—can be used to estimate $\chi(T)$. In localized adsorption,
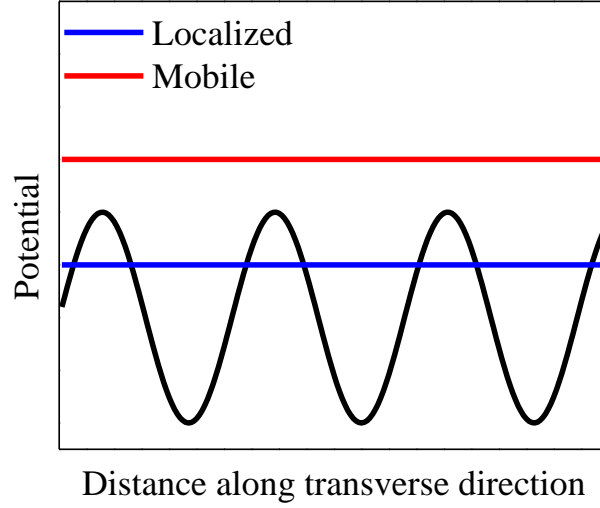
Figure 3.2.2. Corrugated surface potential with adsorbate energies for localized and mobile sorption.
the hydrogen admolecule has three vibrational degrees of freedom and oscillates around a minimum of the potential, $V(x, y, z)$ (adsorption potential), where z is the coordinate perpendicular to the surface, and x, y are the coordinates parallel to the surface. The vibrational frequencies in the three directions, ν_x, ν_y, ν_z are usually of the order of 10^{12} Hz, and as a rule $\nu_x \approx \nu_y < \nu_z$. In mobile adsorption, the molecules still vibrate in the z direction, but have free translational motion in the x, y plane.

The two scenarios yield [38]:

Localized:

$$\chi(T) = \exp\left[\frac{E_B}{N_A kT}\right] \cdot \left[\frac{h^6}{(8\pi M_{Gas})^3 (kT)^5}\right]^{1/2} \cdot \left[\sinh\left(\frac{h\nu_x}{2kT}\right)\sinh\left(\frac{h\nu_y}{2kT}\right)\sinh\left(\frac{h\nu_z}{2kT}\right)\right]^{-1} (3.4)$$

Mobile:

$$\chi(T) = \alpha(T)\exp\left[\frac{E_B}{N_A kT}\right] \cdot \left[\frac{h^2}{8\pi M_{Gas}(kT)^3}\right]^{1/2} \cdot \left[\sinh\left(\frac{h\nu_z}{2kT}\right)\right]^{-1} \qquad (3.5)$$

In these expressions, $E_B > 0$, is the binding energy, defined as the depth of the minima of the potential energy $V(x, y, z)$ per mole of H_2; M_{Gas} is the mass of one admolecule; N_A is Avogadro's constant; k is Boltzmann's constant; and h is Planck's constant. The surface area per site, $\alpha(T)$, is temperature-dependent because adsorbed molecules can be densely packed at low temperature, but require a larger area at higher temperature because of thermal motion in the x, y direction.

It is apparent from equations (3.4) and (3.5) that the Langmuir constant $\chi(T)$ is large if the binding energy is large, the surface area per site is large, the vibrational frequencies are small, and/or the temperature is low.

For the purposes of experiment, the mass of the adsorbed layer is the quantity generally measured, not the coverage. Therefore equation (3.3) can be modified into experimentally more appropriate variables as

$$M_{Ads}(p,T) = M_{Mono}\theta(p,T) = M_{Mono}\frac{\chi(T)p}{1 + \chi(T)p}, \tag{3.6}$$

where M_{Mono} is the mass of one monolayer of adsorbate and $M_{Ads}(p,T)$ is the pressure and temperature-dependent mass of the adsorbed layer. If the surface area per mass of sample (specific surface area), Σ, is known, then the mass of a monolayer of adsorbate can be given as

$$M_{Mono} = \frac{M_{Gas} \cdot \Sigma \cdot M_S}{\alpha(T)}, \tag{3.7}$$

where M_S is the mass of the sample. From comparison of equations (3.6) and (3.7), and the fact that the largest value of the adsorbed mass is the mass of the monolayer, it follows that

$$\alpha(T) \leq M_{\text{Gas}} \cdot \Sigma \cdot \frac{M_{\text{S}}}{M_{\text{Ads}}(p,T)}, \tag{3.8}$$

for any given pressure and temperature. Equation (3.8) allows the experimental determination of a maximum value for the cross-sectional area of the admolecule. In this project, the Langmuir theory of gas sorption will be applied exclusively to supercritical hydrogen sorption.

3.3 Brunauer, Emmett, Teller Theory

Brunauer, Emmett, Teller (BET) theory is an extension of the Langmuir theory. The BET theory of gas adsorption was first published in 1938 [39]. This model is based on four assumptions:

1. There are a fixed number of sites on which gas adsorption may occur,

2. Allows for multilayer sorption, with the number of layers approaching infinity at saturation pressure,

3. Surface is energetically homogeneous, and

4. Allows for absorbent-adsorbate interactions as well as adsorbate-adsorbate interactions perpendicular to the surface, i.e. no lateral adsorbate-adsorbate interactions.

The BET theory allows for multiple layers of adsorbate, with the number of layers approaching infinity as the pressure approaches the saturation pressure for the adsorptive, p_0 [38-40]. The BET isotherm is given by the equation,

$$M_{\text{Ads}}(p,T) = M_{\text{Mono}} \cdot C(T) \cdot \frac{p}{p_0} \cdot \left\{ \left[1 - \frac{p}{p_0} \right] \left[1 + \left(C(T) - 1 \right) \frac{p}{p_0} \right] \right\}^{-1} \tag{3.9}$$

In this expression, M_{Ads} is the pressure and temperature-dependent mass of the adsorbate, M_{Mono} is the mass of an adsorbate monolayer, C is the BET constant, p is the pressure and p_0 is the saturation pressure of the gas. Equation (3.9) gives an IUPAC type II isotherm. Similar to the Langmuir constant, the BET constant incorporates the strength of the adsorbate-adsorbent interaction. The BET model is generally used in its linear form (3.9) given by,

$$\frac{p}{M_{\text{Ads}}\left(p_0 - p\right)} = \frac{1}{C \cdot M_{\text{Mono}}} + \frac{C-1}{C \cdot M_{\text{Mono}}} \frac{p}{p_0}. \tag{3.10}$$

From the slope and y-intercept of (3.10), the cross-sectional area of the admolecule, α, and the mass of the sample, M_{S}, the surface area for mass of sample, Σ, can be calculated as

$$\Sigma = \frac{M_{\text{Mono}} \cdot \alpha}{M_{\text{Gas}} \cdot M_{\text{S}}}. \tag{3.11}$$

Equation (3.11) gives the BET or nominal surface area of the sample. For the research presented, BET theory will be applied exclusively to subcritical nitrogen sorption. The cross-sectional area for an adsorbed nitrogen molecule has an accepted value of 0.162 nm^2 [41]. BET surface area is useful as a reference for material properties, but has been shown to be limited for predominantly microporous samples [33]. It is best applied to isotherms just below the pressure at which the full monolayer is formed, generally from $0.1 < p/p_0 < 0.3$. However, for primarily microporous samples, the monolayer is formed at much lower pressures. Therefore, for this research, a pressure range of $0.01 < p/p_0 < 0.03$ will be adopted.

3.4 Density Functional Theory

The Langmuir and BET theories of gases both present some limitations when applied to strongly microporous materials and materials with varied pore structure. A more recent method of analyzing experimental isotherms and modeling gas behavior is density functional theory [42-44]. Density functional theory presents an opportunity to better model gas behavior in micropores. This is a statistical mechanical approach using the grand canonical ensemble. In this ensemble, the thermodynamic, grand, potential of the system, Ω, is given by

$$\Omega = F - \sum \mu_i N_i , \qquad (3.12)$$

where, F is the Helmholtz free energy, μ_i is the chemical potential of component i and N_i is the number of molecules of component i. If the fluid is assumed to be a single component in an external potential $\Phi(r)$, then the grand potential can be written as [33]:

$$\Omega[\rho(r)] = F[\rho(r)] + \int dr \rho(r) [\Phi(r) - \mu]. \qquad (3.13)$$

The grand potential and the Helmholtz free energy are both functions of the local fluid density, $\rho(r)$. The energy is minimized in order to get the equilibrium density profile. The equilibrium density profile is determined for different pore dimensions, D, through the potential $\Phi(r)$, and at different pressures, through varying the chemical potential μ. This allows for the simulation of theoretical adsorption isotherms and for fitting experimental isotherms through the generalized adsorption isotherm [33],

$$N(p) = \int_{D_{MIN}}^{D_{MAX}} \rho(p, D) f(D) \, dD. \qquad (3.14)$$

In this expression, D is the pore dimension (width of slit), $N(p)$ is the experimental isotherm, $\rho(p,D)$ is the isotherm of a single pore dimension found by DFT and $f(D)$ is the

continuous distribution of these pore dimensions which provides the pore size distribution. For applications to experimental isotherms, the density profile is generally normalized to sorption in materials with known pore structure.

3.4.1 Non-local Density Functional Theory

For this research, two DFT models were used to determine the pore size distribution of the materials: non-local density functional theory (NLDFT) for slit-shaped carbons and quenched solid density functional theory (QSDFT). Non-local density functional theory gets its name from the short-range smoothing functions that are applied to the density profile. These became necessary due to the unrealistic effects of the mean-field approach to the adsorbate [33]. For this theory, the carbon is assumed to be slit-shaped graphitic pores. Therefore in order to calculate the density profile from (3.13), the Steele 10-4-3 potential, Φ_{Steele}, is used for the external potential, Φ.

$$\Phi_{Steele}(z) = 2\pi\rho_{Carbon}\varepsilon_{GS}\sigma^2 \left\{ 0.4\left[\frac{\sigma}{z}\right]^{10} - \left[\frac{\sigma}{z}\right]^4 - \frac{\sigma^4}{\left[3\Delta\left(0.61\Delta + z\right)^3\right]} \right\} \tag{3.15}$$

In equation (3.15), ρ_{Carbon} is the number density of carbon atoms for graphite (114 nm^{-3}), ε_{GS} is the potential energy depth of the gas-solid interaction, σ is the distance at which the potential is zero, z is the distance from the graphite surface, and Δ is the distance between the graphitic planes (0.335 nm) [45]. This potential is then modified to produce the potential in the pores, Φ_{pore},

$$\Phi_{pore}(z) = \Phi_{Steele}(z) + \Phi_{Steele}(H - z) \tag{3.16}$$

where H is the distance between carbon atom center-to-center.

31

For this research NLDFT will be applied to subcritical nitrogen sorption isotherms and supercritical methane sorption isotherms.

3.4.2 Quenched Solid Density Functional Theory

NLDFT assumes that the sorbent is smooth and homogenous throughout and therefore the adsorbent only acts as the source for the external potential. This means that surface roughness and heterogeneity of the solid are not taken into account. This is not necessarily the case for heterogeneous materials similar to the materials in this research. One result of these shortcomings is that NLDFT will result in layering transitions that do not occur in disordered systems; the consequence of which is a minima artifact in the pore size distribution at approximately 1 nm, see figure 3.4.1. Quenched solid density functional theory (QSDFT) was created to overcome these limitations [46].

In QSDFT, the sorbent molecules are treated as components in the system, see (3.12), instead of just as the surface potential. This allows for heterogeneity of the solid as well as surface roughness. The material used to normalize the pore size distribution
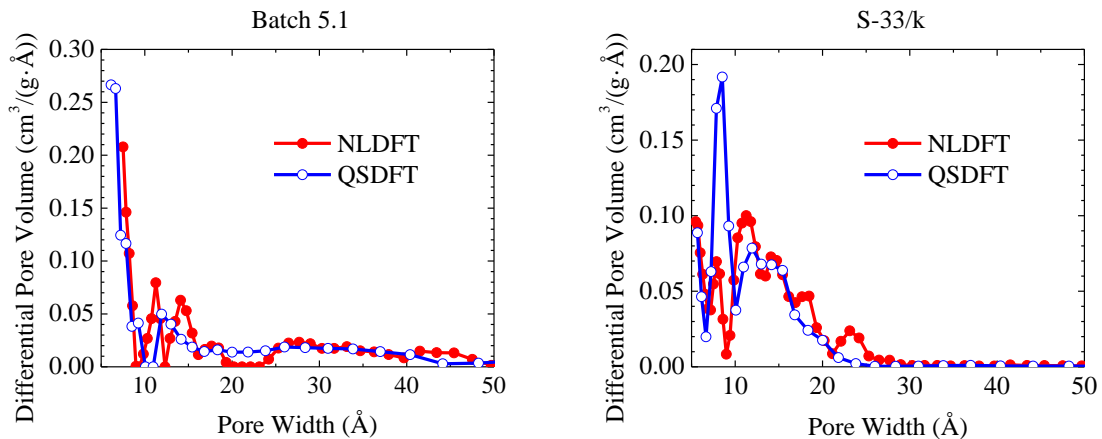
Figure 3.4.1. Pore size distributions for two samples. Left: Batch 5.1 and Right: S-33/k. Note the smoothing pore size distributions for QSDFT as well as the minima artifact in the NLDFT at 10 Å for S-33/k

calculation for QSDFT is generally a disordered carbon-black. For this research QSDFT is applied exclusively to subcritical nitrogen sorption.

3.5 Hypothesis I: Carbon Precursors

Primarily, this project will concentrate on activated carbons produced from corncob precursor. One premise with highly KOH activated carbons is that they lose the original structure of the precursor. If this were true, then activated carbon made from different precursors with the same activation procedure should have similar pore characteristics. Despite this premise, comparison of the pore characteristics for different precursors will reveal that the final pore structure is strongly determined by the precursor chosen.

3.6 Hypothesis II: KOH Activation Effect on Pores

The generally held belief amongst carbon researchers is that during the activation process, KOH gets in between the small sheets of graphene that constitute the carbon. The chemical activation is described by the reactions:

$$2C + 6KOH \rightarrow 2K + 3H_2 + 2K_2CO_3$$
$$yK_2CO_3 + zC \xrightarrow{heat} 2yK + (y+z)CO_x$$
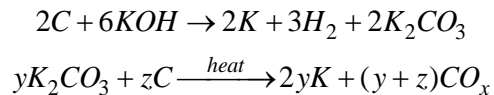
The gases created during the activation (hydrogen, carbon monoxide, carbon dioxide) force the sheets apart [47]. Therefore, it is assumed that the higher the KOH concentration, the more the sheets will be separated and the larger the pore dimension.

3.7 Hypothesis III: Pore Optimization for Gas Storage

The third hypothesis to be tested is that there must be a concentration of KOH that provides the largest values for gas storage. Since there is a pore dimension that should

give the highest amount of adsorbed gas; there should be an optimum concentration of KOH.

Additionally, the amount of stored gas depends on porosity, ϕ, (see appendix A and C). This implies that two samples may have the same volume of optimal pore dimension pores, but have different amounts stored if their porosities are different. Therefore, there may be a concentration of KOH which does not relate to the largest volume of optimum pores, but does relate to the largest amount of gas stored.

3.8 Hypothesis IV: Pore Optimization for Surface Area

A quantity which is of interest not only for gas storage, but also for other activated carbon uses is the surface area for mass sample, Σ. The smaller the pores, the more they will contribute to the surface area of the samples. Due to this nature of the surface area, the samples that have the largest nanoporosity, ϕ_{Nano}, should have the largest surface areas. Nanoporosity is defined to be the percentage of the apparent sample volume (see figure 4.3.3 and table 4.3.1) that is taken up by pores of pore dimension less than 1 nanometer.

3.9 Hypothesis V: Adsorption Physics

By applying the Langmuir model described in section 3.2, additional physics of adsorption of methane and hydrogen will be discovered. This further understanding of the physics behind the adsorption of these gases will lead to new ways of optimizing the samples. By comparison of experimental isotherms to theoretical generated isotherms, the adsorbed gas behavior, i.e. localized or mobile, will be determined for the cases of room temperature methane and hydrogen and 77 K hydrogen. Once this is known, the

34

binding energies of the samples can be found by fitting (3.3) to the experimental

isotherms and then solving (3.4) and/or (3.5). Further, an experimental limit to the area

per adsorbed molecule, $\alpha(T)$ can be found using inequality (3.8).

Chapter 4: Methods and Procedures

The unusual nature of the samples (high gas uptake, high surface areas, high porosity, trace elements) requires special attention to be paid during analysis. Numerous methods were chosen to determine both qualitative and quantitative characteristics of the activated carbons and their engineered pore spaces.

4.1 Electron Microscopy Methods

Electron microscopy determined the qualitative characteristics of the carbon samples. Both scanning and transmission electron microscopy studies were performed. Each method has its advantages. Scanning electron microscopy (SEM) can reveal information about the surface topography and regions of different chemical species. Transmission electron microscopy (TEM) can reveal information about the pore network and information about the interior of the sample.

Scanning electron microscopy Field emission scanning electron microscopy (FESEM) was performed using a Hitachi S-4700 FESEM. The FESEM work was completed with use of both the secondary electron (Everhart-Thornley) detector and the backscattered electron detector. Secondary electrons give superior depth of field and will therefore display the topography of the sample, whereas backscattered electrons exhibit atomic number dependence and therefore show regions of differing average atomic number, figure 4.1.1. Scanning electron microscopy (SEM) typically requires samples to
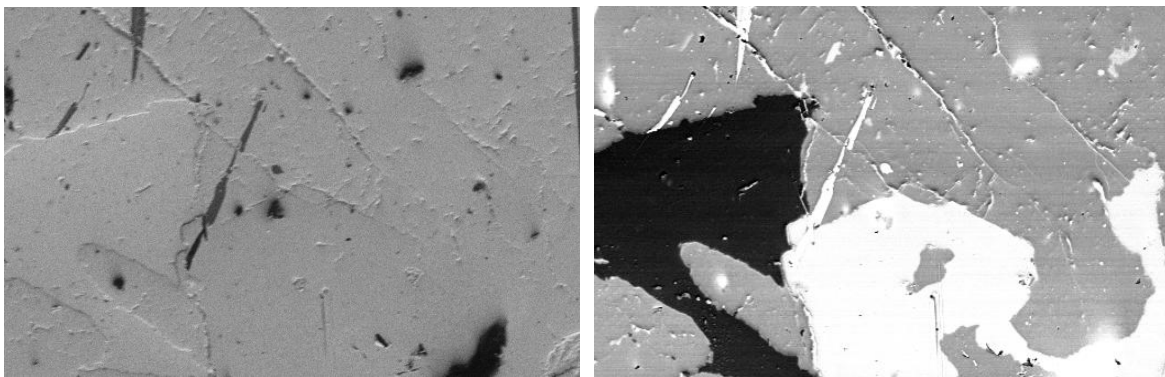
Figure 4.1.1. The same region of sample being investigated with secondary electron detection (left) and back-scatter electron detection (right). Notice the average atomic number dependence of the back-scatter electrons shown as regions of white, gray and black.

be coated with a conducting material (e.g. carbon, gold or platinum), since our materials are close to pure carbon (> 95%) no coating was required or used. Ultra high resolution mode was used with the beam energy set to 5 kV and a small working distance (3-4 mm).

In addition to FESEM work, samples were analyzed with transmission electron microscopy (TEM). TEM analysis is used to explore the pore space of the samples at high magnifications. Additionally, the presence of iron in some of the samples (see later sections) raised the question whether the iron was atomically dispersed in the samples, or in clusters of iron atoms, which is typically the case. TEM has the ability to image iron clusters and therefore determine the size of the iron clusters. This analysis was done on a JEOL 1200EX TEM instrument. Samples were prepared for analysis in two ways. Samples were set in a resin and then microtomed. A diamond knife was used to achieve thicknesses of ~50 nm. The microtomed slices were then placed on a copper grid for use in the TEM. Samples were also prepared by mixing powdered sample with isopropyl alcohol and then a drop of the carbon-alcohol suspension was placed on one of the copper TEM grids and allowed to dry. The TEM was set to 100 and 120 kV.

4.2 Chemical Composition Analysis Methods

Three methods of chemical composition analysis were performed: energy dispersive spectroscopy (EDS), x-ray fluorescence spectroscopy (XRF) and inductively coupled plasma atomic emission spectroscopy (ICP-AES).

Chemical composition analysis was completed using the energy dispersive x-ray spectroscopy (EDS) detector on the Hitachi S-4700 FESEM, housed at the University of Missouri Electron Microscopy Core. The working distance was set within the range of 11 to 12 mm. EDS analyzes the characteristic x-rays given off by the sample during SEM. EDS can give a qualitative and quantitative report about the elemental composition of the sample. The chemical species are determined from the proportions of each element and the geometry of the region being probed. The lowest atomic number element that could have been determined from the analysis performed was beryllium, this limit is set by the maximum beam energy of the instrument and the design of the EDS detector. Another constraint on EDS analysis is that the probing region is small and only probes ca. 1 to 2 µm into the sample surface. Therefore EDS is useful for determining the characteristics of small parts of the samples, but is ineffective at determining the bulk chemical characteristics of the sample.

XRF was completed by researchers at IMG-Centre d'Analyse Minérale at the Universite de Lausanne, France using a Pananalytical PW 2400, wavelength dispersive XRF-spectrometer. XRF analyzes the energy of the secondary (fluorescent) x-rays emitted when the sample is exposed to gamma rays or high-energy x-rays. Similar to EDS, XRF is considered a surface technique. Lighter elements can typically only be

detected within the first few microns of the sample. Additionally, the lowest atomic number element XRF can reasonably detect is magnesium.

An outside firm was hired to carry out ICP-AES on select samples. In order for ICP to be performed, the sample is first burnt and the ashes are used for analysis. This unfortunately eliminates the possibility of learning about the elemental composition of the carbon matrix, as well as destroys the sample. Therefore, ICP is typically coupled with other techniques to learn more about the C, H, O, and N content. The ICP instrument uses inductively couple plasma to break down the compounds in the ash and ionize the elements. As the molecules lose electrons and recombine, light is given off at characteristic wavelengths. ICP has the ability to measure the concentration of every element besides argon since it is used to create the plasma.

4.3 General Features of Gas Sorption Measurements

4.3.1 Manometry and Gravimetry

There are two main categories of gas sorption measurements: manometry and gravimetry. The two different methods derive their names from what is being measured. In manometry, pressure measurements are used to determine the gas sorption quantities. This method is also known as volumetry, which is a legacy term derived from the original experiments using the volume of liquid mercury to determine the change in the gas volume. The terms volumetry and volumetric instruments are still widely used [33]. For this work, the term manometry will be used for the sake of accuracy. Alternative to manometry is gravimetry, where the quantity measured is mass. Each methodology has advantages and disadvantages.

4.3.2 Sorption Measurement Quantities

When performing gas uptake measurements with these two methods, three different measures of adsorption are used: absolute adsorption, excess adsorption and total amount stored. These terms are commonly found in the literature and often confused. Absolute adsorption is defined to quantify the amount of adsorbate exclusively on the surface of the adsorbent. This quantity is often used because it is the direct output of most statistical mechanics theories and molecular simulations [48]. The absolute adsorption mass will only increase or plateau with increased pressure.

In contrast to the absolute adsorbed mass, Gibb's excess or excess adsorbed mass is defined as the mass of adsorbate film minus the mass of an equal volume of adsorptive. The term excess relates to the idea that this amount of gas is in excess of what would be in the pores if there were no adsorbent potential. At low pressures (< 1 bar) excess and absolute adsorption are similar, but at high pressures they can differ significantly. One key difference between the two measurements is the behavior of excess adsorbed quantities as the adsorptive density approaches the adsorbate density. It is obvious from figure 4.3.1 that if the density of the adsorbate were equal to the adsorptive, the excess quantity would be zero. As such unlike the behavior of absolute adsorbed mass, an excess adsorption isotherm will peak and then decrease as the pressure increases. If the
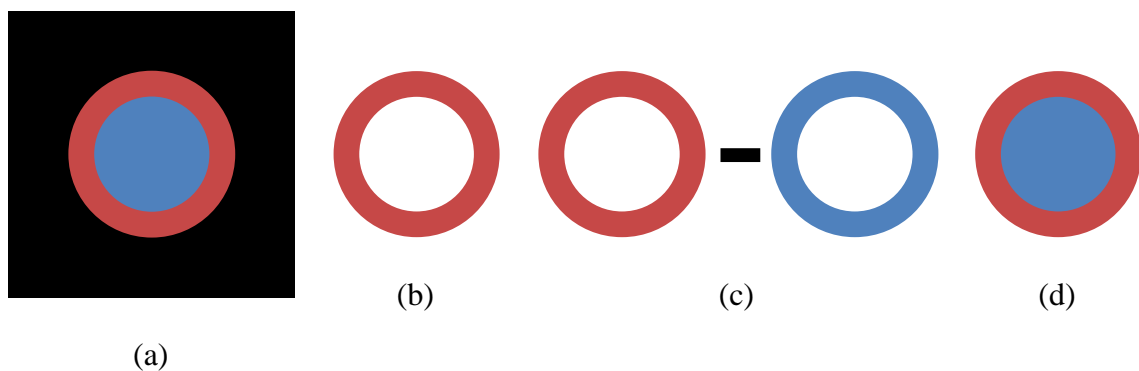
Figure 4.3.1. (a) Cartoon of carbon (black) pore with adsorbate film (red) and adsorptive gas (blue) (b) Absolute adsorption (c) Gibb's excess adsorption (d) Amount gas stored.

density of the adsorptive is larger than the density of the adsorbate, the excess quantity will go negative. Another feature of excess adsorption is that its value depends on the placement of the Gibb's dividing surface. The common position for the Gibb's dividing surface is along the surface of the sample as determined by gas pycnometry. The common gas used for pycnometry is helium. Unfortunately the use of helium pycnometry has two drawbacks. First, some samples adsorb helium even at reasonably low pressures and room temperature. In order to overcome this issue, high-temperature pycnometry is used, sometimes requiring temperatures as high as 500 °C. Secondly, the volume that the helium sees might not be the same as the volume that the adsorptive gas being measured will see. Therefore, it has been suggested that gas pycnometry should be done with a gas with a similar virial coefficient as the sorption gas to be measured [33].

Finally, the quantity of most interest from a practical point of view is the total amount stored, defined to include both adsorbed and non-adsorbed molecules in the porous materials, in other words, gas in both adsorbate and adsorptive phases. The total amount stored will only increase with increased pressure. At high pressures, the adsorptive density starts to play a larger role and as such the total amount stored should

41

start to increase approximately linearly as the adsorptive gas density increases approximately linearly. Experimentally, only excess adsorption or total amount stored can be directly determined in either gravimetric or manometric measurements [33, 48]. The value normally determined is the Gibb's excess amount. Figure 4.3.1 illustrates the differences between these three different measures of adsorption.

4.3.3 Volumes and Densities

For gas sorption experiments there are certain volumes and densities that can be found or need to be assumed for the sample. For the sake of consistency, these terms will be defined in this section. The majority of samples that were analyzed as part of this research were powders. Figure 4.3.2 depicts an individual grain and multiple grains in a container. In a sample there can be both open and closed pores. An open pore means that the pore is accessible from the outside of the grain, whereas a closed pore is completely surrounded by the solid carbon matrix. When there are multiple grains, there is an additional volume that occurs between them called the inter-particle void volume. The definition and practicality of the inter-particle void volume is often uncertain. For the purposes of this project, the inter-particle void volume will be assumed to be included in the open pore volume. The volumes listed can be used to determine characteristic volumes for the samples and there corresponding densities found using the mass of the sample.

The true density of the material uses only the solid carbon matrix volume. This is

(a)   (b)
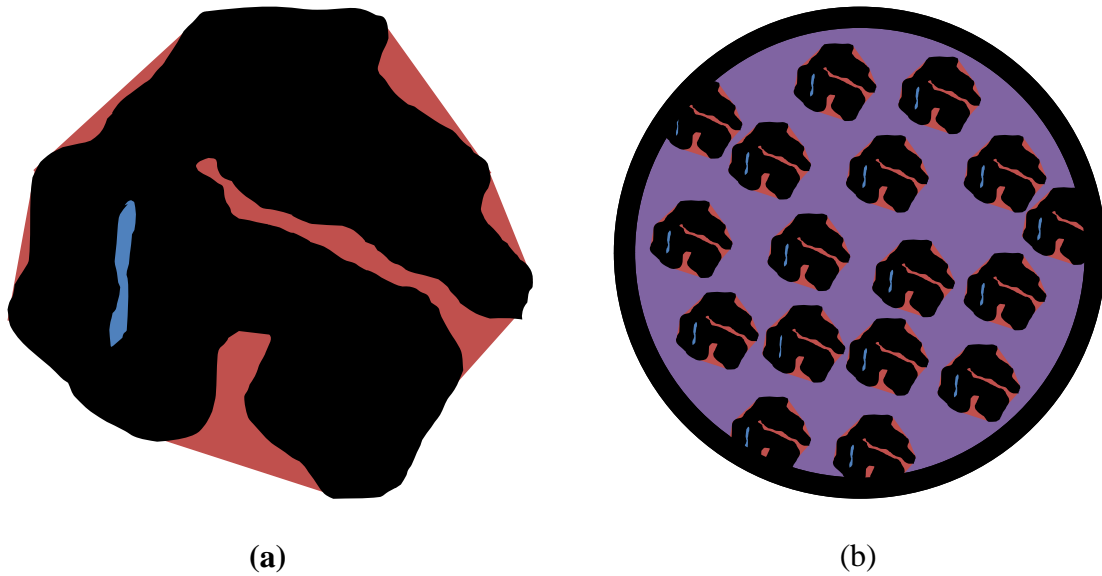
Figure 4.3.2. (a) Cartoon of a single carbon grain depicting open pore volume (red), closed pore volume (blue) and solid material volume (black). (b) Multiple carbon grains showing the same volumes as in (a) with the addition of the inter-particle void volume (purple).

sometimes also referred to as the theoretical density because there are few experiments

that it can be determined from. The next density is the skeletal density, $\rho_{Skeletal}$. The

skeletal volume includes the true and closed pore volumes. The activated carbons used in

this project more-than-likely contain few if any closed pores. The fact that the skeletal

density is lower than the theoretical density for the carbons can be explained by defects in

the carbon matrix. The skeletal density is generally determined through gas sorption

manometry using a non-adsorbing gas, for example helium. As mentioned in section

4.3.2, helium does have some drawbacks. Therefore it is advisable to always mention the

method by which the skeletal density was found. It is the skeletal density which will be

needed to calculate the excess amount adsorbed. In order to calculate the total amount

stored the density of interest is the apparent density, $\rho_{Apparent}$. The apparent volume of

the sample includes the carbon matrix and the volume of both open and closed pores.

The apparent volume of a grain can be considered to be the volume enclosed in a convex

hull of the grain. It is generally calculated from the total open pore volume, $\dfrac{V_{\text{OpenPore}}}{M_{\text{S}}}$, as

determined by subcritical nitrogen experiments, section 4.4.4, and assuming the skeletal

density of the carbon is $\rho_{\text{Skeletal}} \cong 2.0 \dfrac{\text{g}}{\text{cm}^3}$.

$$\rho_{\text{Apparent}} = \left(\rho_{\text{Skeletal}}^{-1} + \frac{V_{\text{OpenPore}}}{M_{\text{S}}} \right)^{-1} \tag{D.1}$$

The final volume to be considered is the bulk powder volume. The bulk powder

volume includes the carbon matrix volume, open and closed pores as well as the inter-

particle void volume. For use only with powders, this volume is often difficult to

determine as it depends entirely on how the powder is packed. It is for this reason that

the inter-particle void volume is included in the open pore volume. It follows that the

bulk powder density will be approximated as the apparent density of the sample. Table

4.3.1 summarizes these volume and densities.

Table 4.3.1. Names of densities used, and the volumes included in that density

Density	Solid Material Volume	Closed Pore Volume	Open Pore Volume
True	X		
Skeletal	X	X	
Apparent	X	X	X

In addition to these characteristic sample densities, the porosity of the sample is

defined by these volumes. The porosity is defined as the fraction of the apparent volume

that is occupied by open pores. The porosity, ϕ, can be calculated from the skeletal

density, ρ_{Skeletal}, and the volume of open pores for mass sample, $\dfrac{V_{\text{OpenPore}}}{M_{\text{S}}}$ as

$$\phi = \left[1 + \left(\rho_{\text{Skeletal}} \cdot \frac{V_{\text{OpenPore}}}{M_{\text{S}}} \right)^{-1} \right]^{-1}. \tag{4.2}$$

The full derivation is shown in Appendix A. The skeletal density and volume of open pores for mass sample are both experimentally determinable quantities. A modification to the porosity is the nanoporosity. This is simply defined to be the fraction of the apparent volume that is occupied by pores under 1 nm in pore dimension.

4.4 Manometric Subcritical Nitrogen Sorption Methods

Nitrogen adsorption allows the characterization of pores in the micropore regime and mesopore regime [43]. Nitrogen adsorption experimental isotherms from 10^{-6} to 1 bar and 77 K (subcritical temperature and pressure) were run on select activated carbons using a Quantachrome Instruments Autosorb 1-C manometric instrument.

4.4.1 Autosorb: Sample Preparation

The Autosorb 1-C has two cells in the LN2, the sample cell and a reference cell. The reference cell, also called the p_0 cell, is used to determine the vapor pressure of the liquid nitrogen. This value is used as the saturation pressure of the nitrogen. The other cell is the sample cell, see figure 4.1.1. This cell contains the sample to be analyzed. For the Autosorb 1-C to determine a high-quality isotherm, the approximate surface area of the sample should be between 10 and 25 m^2. The higher the surface area in the cell, the longer the system will take to reach equilibrium. Since the Autosorb uses a liquid nitrogen bath to maintain 77.3 K, the experiment will end when the liquid nitrogen finishes evaporating, generally 30+ hours. Therefore, high surface area materials need to be analyzed with small amounts of sample. For the materials to be presented, surface

areas in excess of 1,000 m^2/g are typical. This means that a typical amount of sample used needs to be approximately 25 mg.

Before any gas uptake measurements can take place, the sample must be outgassed to remove any moisture or other contaminants. This is true for any gas uptake measurements included the different methods discussed in the following sections. When outgassing a sample, there are two primary variables to be considered: temperature and time. The higher the temperature, the less time it will take for the sample to finish outgassing. Therefore the highest temperature appropriate should be used. Care needs to be taken in how that temperature is reached, however. If the temperature is raised too quickly, then three harmful scenarios can occur. First, the quick raise in temperature will cause the moisture in the sample to leave very quickly, which increases elutriation of the sample. Secondly, the moisture and other gases being removed from the samples may have too much energy as they leave the sample and can damage the pore structure. Finally, the highest temperature used may be near a temperature of concern for the sample if it has any gas present. For example, the temperature at which activated carbon burns is about 410 °C. Therefore, if the final temperature is 400 °C, oxidation of the carbon will still occur if sufficient time was not allowed for all the oxygen to be removed. A typical outgassing procedure for the Autosorb is as follows: 1 hour each at room temperature, 60 °C, 80 °C, 120 °C, 200 °C, followed by several hours at 400 °C. The time at 400 °C is determined by watching the pressure rise when the vacuum valve is closed. Too fast a rise reveals the material has not finished outgassing.

Additional care also needs to be taken when choosing the sample cell. Various cells are available with different diameter stems and with or without bulbs. Additionally,

air sensitive sample can be tested with the cell seal assembly which automatically closes every time the cell is removed from an outgassing or analysis port. For the materials in this research, a narrow stemmed, bulbed cell is preferred. The large bulb is necessary for the sample to be exposed to as much gas as possible. Additionally, the narrow stem will allow for faster equilibration at lower pressures, e.g. 10^{-6} bar. The mean free path of the gas should be much larger than the stem inner diameter. This will increase the number of collisions with the cell and allow the gas to reach the sample much faster. The narrow stem also eliminates the dead-volume around the sample; which decreases the uncertainties in the uptake calculations. Unfortunately, a narrow stem diameter will also lead to more sample being elutriated, so care needs to be taken to protect the valves and transducer in the system.

4.4.2 Autosorb: Dosing Procedure

The final sample cell equilibrium pressures are set by the user. For surface areas the isotherm will go from ~0.01-0.03 bar, but for more detailed analysis the isotherm will range from ~10^{-6} to 0.99 bar. In order to determine whether the gas has finished adsorbing, the instrument applies two settings: the equilibration time and tolerance. The tolerance sets a pressure band about the target pressure set by the user. The dosing
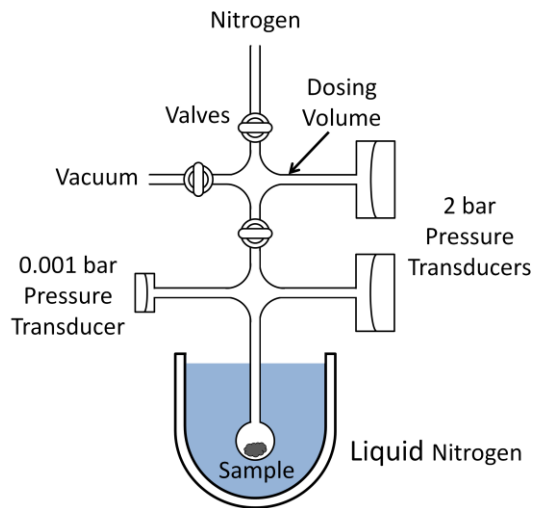
Figure 4.4.1. Left: cartoon depicting the functionality of the Autosorb 1-C. Right: Autosorb 1-C showing analysis station (left dewar), cold-trap (right dewar), and two outgassing stations (2 ports on right).

procedure begins with the system building nitrogen pressure in the dosing volume, figure 4.4.1, to the top of the tolerance band. Once the specified pressure is attained, the sample cell valve is opened and the nitrogen dose is allowed to expand into the sample cell. The instrument then waits the equilibration time. After which, it determines whether the pressure has broken the tolerance band. If the pressure breaks the tolerance band the system has not reached the equilibrium pressure requested. An additional dose of nitrogen is added by closing the valve, pressurizing the dosing volume again, and then reopening the valve. This is repeated until the pressure remains within the tolerance band after the equilibration time. At this point, the uptake is calculated and the next desired pressure is attempted.

4.4.3 Autosorb: Critical Features

This method will be identified as a dosing-manometric method. There are advantages and disadvantages to this approach. The advantages are that final equilibrium pressures for the isotherm can be set by the user and the highest pressure attainable can be set to the maximum pressure of the dosing volume. The major drawback of this technique is that the uptake at a given pressure depends on the calculated uptake at the previous pressure. This results in successive errors. Therefore, dosing-manometric instruments need to pay special care to the pressures being measured. This is why the Autosorb 1-C has an additional 1 mbar transducer for lower pressures.

Furthermore, the instrument has two primary temperature regions: inside the dewar at 77 K and the remainder of the set-up at room temperature. Thermal transpiration will occur because the stem diameter is less, sometimes much less, than the mean free path of the gas. The consequence of thermal transpiration is that pressure at either end of the stem will actually differ. At very low pressures, this pressure difference is given by the Knudsen equation [49],

$$\frac{p_{\text{Cell}}}{p_{\text{Gauge}}} = \sqrt{\frac{T_{\text{Cell}}}{T_{\text{Gauge}}}} \tag{4.3}$$

where, $p_{\text{Cell}}, T_{\text{Cell}}$ are the pressure and temperature, respectively, of the sample cell; and $p_{\text{Gauge}}, T_{\text{Gauge}}$ are the pressure and temperature, respectively, at the pressure transducer. For the subcritical nitrogen sorption measurements, the sample cell is at 77 K and the transducers are ~300 K. This results in the sample cell pressure being almost half of the gauge pressure. For intermediate pressures, the Knudsen equation is no longer valid and

an empirical equation is generally used to determine the pressure difference. The most popular empirical equation is the Takaishi and Sensui equation [50],

$$\frac{p_{Cell}}{p_{Gauge}} = 1 + \frac{\sqrt{T_{Cell}/T_{Gauge}} - 1}{10^5 AX^2 + 10^2 BX + C\sqrt{X} + 1}$$

$$X = \frac{1.5 p_{Gauge} d}{T_{Cell} + T_{Gauge}}$$

(4.4)

where, A, B, C are empirically determined constants for each individual gas and d is the diameter of the tube. The Autosorb analysis program, however, uses the Liang equation [51],

$$\frac{p_{Cell}}{p_{Gauge}} = \frac{\alpha\varphi^2\chi^2 + \beta\varphi\chi + 1}{\alpha\varphi^2\chi^2 + \beta\varphi\chi + \sqrt{T_{Cell}/T_{Gauge}}}$$

$$\chi = 0.133 p_{Gauge} d$$

(4.5)

where, α, β are constants determine for helium and φ is the correction for use with other gases and only depends on the molecular diameter of that gas. The Liang equation is used for its versatility for use with other gases. Instead of having to determine all new coefficients as in (4.4) the only new quantity needed is the molecular diameter of the new gas.

Not only does this temperature gradient create issues with determining the pressure at the sample. It also needs to be taken into consideration for calculation of the volumes needed for the uptake calculation. The Autosorb manages this by performing helium pycnometry both with and without the sample cell in the liquid nitrogen bath. This may be satisfactory for most samples, but high-surface are activated carbons are known to adsorb helium at room temperature nonetheless 77 K. Therefore, it is advised

50

for future research to determine how the isotherm should be modified to correct for any errors in the helium pycnometry.

4.4.4. Autosorb: Sample Characteristics Determined

The final nitrogen adsorption/desorption isotherms are used to determine the pore characteristics of the sample and the nominal surface area. Although the isotherms are technically excess sorption isotherms, since the pressure is low, they are assumed to be approximately the same as absolute sorption isotherms. NLDFT and QSDFT can therefore be applied to isotherms that contain adsorption data points from 10^{-6} to 1 bar and desorption data points from 1 bar to 0.1 bar. These two methods are performed using the computer kernels provided with the Autosorb software. The results of the DFT analysis are differential and cumulative pore volume and surface area plots and tables. This data will be used to determine the pore volumes between certain ranges and for determination of the nanoporosity. Additionally, BET theory is applied to the data between $0.01 \rightarrow 0.03 \, p/p_0$. The final data point resulting from the nitrogen isotherm is the total open pore volume for mass sample. This is the value used to calculate the porosity via equation (4.2), assuming a skeletal density of $\rho_{\text{Skeletal}} = 2.0 \, g/cm^3$. In general, nitrogen sorption isotherms are reported as volume of nitrogen at standard temperature and pressure (STP) versus reference pressure p/p_0. The primary assumption of subcritical nitrogen isotherms is that the adsorbate density is the same as the liquid density of nitrogen. Therefore, the volume at STP refers to the volume that the liquid nitrogen in the pores would take up if it were allowed to evaporate and expand so as to reach STP.

51

The assumption is made that at very high relative pressure, almost $p/p_0 = 1$, all of the

pores are completely filled with liquid nitrogen. Therefore the open pore volume can be

found by

$$\frac{V_{\text{OpenPore}}}{M_{\text{S}}} = \frac{\rho_{\text{STP}}}{\rho_{\text{LN2}}} \cdot \frac{V_{\text{STP}}}{M_{\text{S}}} \tag{4.6}$$

where, $\dfrac{V_{\text{STP}}}{M_{\text{S}}}$ is the value at the highest pressure taken, ρ_{STP} is the density of nitrogen at

standard temperature and pressure, and ρ_{LN2} is the density of liquid nitrogen.

4.5 Manometric Supercritical Hydrogen Sorption Methods

The measurement of the sorption of hydrogen gas introduces many more

complications to the experiments. First, hydrogen is a small, lightweight molecule. This

means that experimental set-ups are prone to leaks. Furthermore, the low mass of the

molecule makes it difficult to attain reliable results from gravimetry. Therefore, the best

hydrogen uptake instruments are manometric.

Secondly, hydrogen is known to react readily with many materials.

Consequently, the normal use of polymeric o-ring, vco-type, fittings could result in leaks.

The use of metal o-ring, vcr-type, fittings is suggested. Additionally, it is best to restrict

any wetted parts in the system to stainless steel, gold or other inert metals. Stainless steel

is commonly used for set-ups. Unfortunately hydrogen is known to embrittle stainless

steel [52, 53]. For that reason, it is best to have set-up be designed for pressures

significantly higher than the maximum pressure to be used. One final issue related to the

reactivity of hydrogen is the need for ultra-high purity hydrogen gas. Hydrogen can

combine with oxygen in the lines to form water. As a consequence, it is best to use ultra-high purity hydrogen (99.999% hydrogen) and to include a filter or molecular sieve immediately before the dosing or reservoir volumes.

The last issue surrounding hydrogen sorption experiments for activated carbons is the low binding energy between hydrogen and carbon, ~5 kJ/mol. As a result, hydrogen measurements at room temperature are often difficult due to the small amount of excess adsorbed. Keeping these constraints in mind, two different manometric hydrogen sorption instruments were used.

4.5.1 Rapid-screening Hydrogen Sorption Instrument

The need for more results drove the design and implementation of a rapid-screening hydrogen sorption (RHS) instrument. The HTP1, discussed in sections 4.5.2-4.5.6, can take multiple days to perform a single analysis. Consequently, samples need to be screened first so as not to take up too much instrument time. The RHS is another dosing-manometric instrument, see figure 4.5.1. The sample analysis takes place completely at room temperature, eliminating thermal transpiration effects.

Sample preparation is similar to the methane gravimetric technique discussed in later sections. Sample amounts as large as 3 grams can be measured on the RHS. Generally, as much sample as possible is used in order to decrease uncertainties. The sample is first outgassed at room temperature for 10 minutes followed by 2 hours at 400 °C. Some of the samples are air sensitive so the sample cell is prepared in a nitrogen atmosphere glove box.
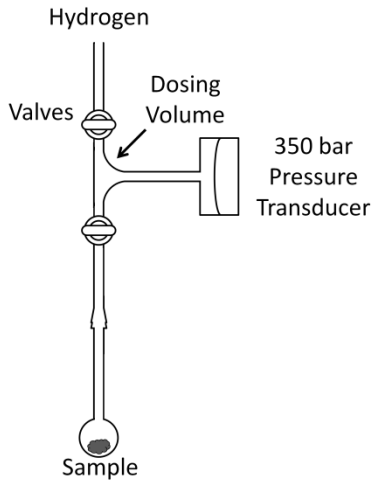
Figure 4.5.1. Left: Cartoon model of the rapid-screening hydrogen sorption apparatus. Right: Picture of the rapid-screening hydrogen sorption apparatus.

Given that the RHS is designed to measure samples quickly, only one dose is performed. Typically the dose is prepared at 70 bar and then allowed to expand into the sample cell. This creates a large amount of elutriation of the sample which was under vacuum. For that reason, a 2 micron filter was placed between the sample and the remainder of the set-up. Another result of the large pressure difference is an increase in the equilibration time. The equilibration time for this set-up is simply the amount of time the user waits before recording the equilibrium pressure. A large change in gas pressure leads to a significant change in its temperature. As a consequence adequate time needs to be given for the temperature to equilibrate with the room temperature. The excess hydrogen uptake for mass sample, M_{Ads}^{Ex}/M_S, is calculated using

$$M_{Ads}^{Ex}/M_S = \frac{\rho_{Initial}^{Dosing} \cdot V^{Dosing} - \rho_{Final}(V^{Dosing} + V^{SampleCell})}{M_S} + \frac{\rho_{Final}}{\rho_{Skeletal}} . \qquad (4.7)$$

54

$\rho_{\text{Initial}}^{\text{Dosing}}$ and ρ_{Final} are the density of the hydrogen adsorptive in the dosing volume before the valve is opened, and in the dosing and sample cell volume after the cell is opened, respectively. The densities are determined using the NIST Chemical Webbook [54]. V^{Dosing} and $V^{\text{SampleCell}}$ are the dosing and sample cell volumes, respectively. To calibrate these volumes, hydrogen pycnometry is performed using a stainless steel cylinder of known volume. The skeletal density, ρ_{Skeletal}, is assumed to be $\rho_{\text{Skeletal}} \cong 2.0 \, ^{\text{g}}\!\big/\!_{\text{cm}^3}$. Detailed derivation of equation (4.7) can be found in Appendix D, with the additional assumption that the final adsorptive densities in the dosing volume and sample cell are the same. The values from RHS measurements on different samples are used to decide which samples will have more systematic analyses performed.

4.5.2 Hiden Isochema HTP1-V Mark II

The second hydrogen manometric instrument is a Hiden HTP1-V Mark II (HTP1), produced by Hiden Isochema, see figure 4.5.2. The HTP1 has the capability to run hydrogen measurements up to 100 bar and at any temperature between 77 K and 775 K. For temperature below room temperature, liquid nitrogen is flowed through a collar around the sample cell. A heating mantle is used to maintain the temperature between 77 K and room temperature. For temperatures higher than room temperature, no liquid nitrogen is used, simply the heating mantle. In addition to these features, the HTP1 also utilizes a gold-plated sample cell both for issues of hydrogen with stainless steel and for samples which may be reactive themselves.

4.5.3 HTP1: Sample Preparation

The typical sample amount analyzed on the HTP1 is 100 mg. The sample can be outgassed one of two ways: by the HTP1 or externally. The HTP1 has its own outgassing procedure where the user can program how the sample is heated by the heating mantle and the duration at each temperature. This has the benefit of the sample not being exposed to air after outgassing. Unfortunately, certain samples may contain volatile compounds that should not get into the HTP1 station. The Autosorb instrument has a cold-trap to protect the turbo-pump and the remainder of the instrument, whereas the HTP1 does not. Another drawback for the use the HTP1 on-board outgassing comes in the determination of the sample mass. The sample mass is determined by taking the difference of the mass of the HTP1 cell with sample after outgassing and the mass of the HTP1 cell alone. This requires removal of the HTP1 cell from the HTP1 set-up after the hydrogen analysis and the cell mass by the analytical balance. Unfortunately the samples typically adsorb moisture and even nitrogen fairly quickly, raising doubt about the true sample mass. The other method of outgassing is to outgas the HTP1 cell inside one of the gravimetric sample cells see figure 4.7.1. This allows a better measurement of the sample mass because the gravimetric sample cell can be weighed on the precision balance. This may not outgas the sample quite as well as on-board simply because the vacuum used is only a roughing pump. Additional care also needs to be taken not to increase the temperature too high because there may be enough gas left in the gravimetric cell to cause tarnishing of the gold-plated HTP1 cell.

4.5.4 HTP1: Dosing Procedure

The HTP-1 is another dosing-manometric instrument, see figure 4.5.2. The primary difference between the dosing procedure used by the Autosorb and the HTP1 is how the pressures to be measured are assigned. The Autosorb allows the user to set the final equilibrium pressures in the sample cell. The HTP1, however only allows the user to program the initial pressure in the dosing volume. The initial dosing volume pressure is approximately twice the final equilibrium pressure. Typically, the user sets the temperature for the isotherm, the initial dosing pressures for the desired data points and the amount of time to wait before taking a measurement for each of these pressures. The HTP1 pressurizes the dosing volume, waits for the temperature of the dosing volume to equilibrate, and then opens the sample cell valve. The instrument waits the equilibration time and then takes a measurement. The sample cell valve is then closed and the dosing
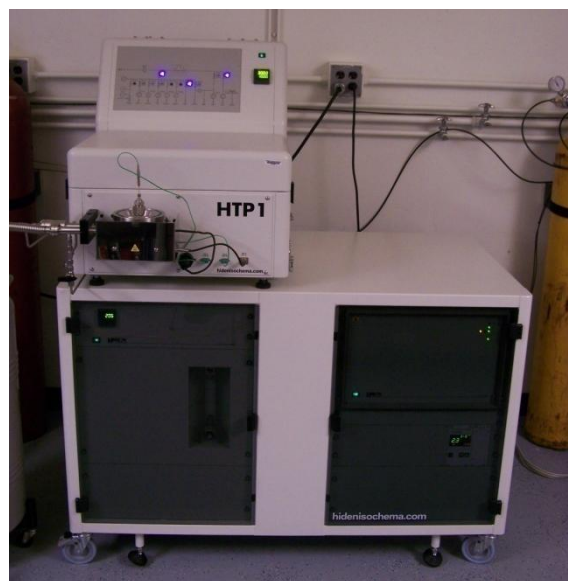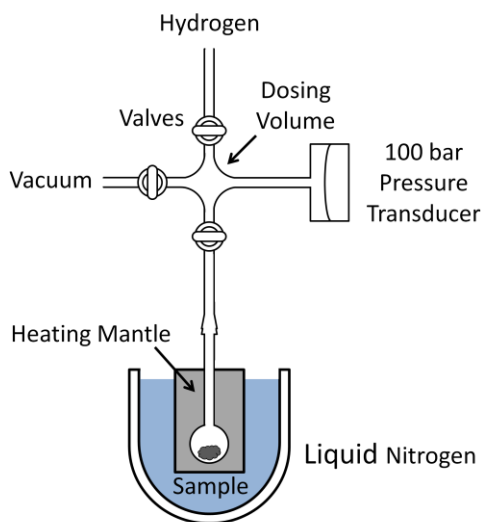
Figure 4.5.2. Left: Cartoon model of the HTP1 apparatus. Right: Picture of the HTP1 apparatus.

volume is pressurized to the next desired pressure. The dosing procedure is repeated for the remainder of the pressures.

4.5.5 HTP1: Critical Features

When performing analysis with the HTP1, there are many issues to keep in mind. This is a dosing-manometric instrument and as such results in successive uncertainties in the uptake measurements. The HTP1 only has one 100 bar transducer which has an uncertainty of ±0.05 bar. For pressures at or below 1 bar, the uncertainty becomes quite high. This is not as large of an issue as previously assumed because the measured uptake at these pressures is relatively small compared to the rest of the isotherm. Consequently, the effect the uncertainty at these low pressures should be negligible at higher pressures.

The HTP1 handles the temperature gradient between the sample and the pressure transducer through a fractional volume. The fractional volume is determined by analyzing isotherms performed on a non-adsorbing calibration volume. The adsorption should be zero, so the dosing and sample cell volumes are modified using the fractional volume. This is a novel, albeit complicated, means to handle the thermal gradient.

One final feature of the HTP1, is the performance of helium pycnometry to determine the skeletal volume of the sample. Unfortunately, the helium pycnometry is performed only at room temperature. Consequently, samples which are known to adsorb helium at room temperature are found to have unphysical skeletal densities. These skeletal densities are larger than the skeletal density of pure graphite, which is assumed to be the theoretical maximum for activate carbons. One method to avoid this issue is to

again assume the skeletal density is $\rho_{Skeletal} \cong 2.0\,{}^g\!/\!{}_{cm^3}$ and calculate the skeletal volume from the sample mass.

4.5.6 HTP1: Sample Characteristics Determined

The HTP1 is used to determine excess hydrogen for mass sample isotherms from 1 to 100 bar, typically at 80 K and room temperature. The excess adsorption calculations use the compressibility of the gas to calculate the density of the adsorptive from the modified ideal gas law

$$pV = nZRT .\qquad\qquad(4.8)$$

p, V, n, Z, and T are the gas pressure, volume, number of moles, compressibility factor, and temperature respectively. R is the ideal gas constant. This is an adequate approximation for the behavior of hydrogen.

From these excess adsorption isotherms and input from the subcritical nitrogen sorption measurements, the amount stored, and absolute adsorption can be determined. Furthermore, these isotherms can be analyzed to determine hydrogen sorption physics.

4.6 Manometric Supercritical Methane Sorption Methods

The manometric supercritical methane sorption apparatus, also called the methane test fixture, is used to measure methane sorption on full carbon monoliths (briquettes), see figure 4.6.1. The monoliths are 3 inches in diameter and usually are around 1 inch in thickness. Monoliths may be preferred to powder for methane storage because of ease of use and a higher volumetric storage capacity. The methane test fixture performs uptake analysis at room temperature and pressures from 2 to 35 bar.

Figure 4.6.1. Picture of carbon monolith and corncob precursor.

4.6.1 Manometric Methane: Sample Preparation

The carbon monoliths are generally between 60 and 100 grams in mass. Prior to outgassing the briquette's dimensions are determined using vernier calipers. For briquettes, this geometric volume is used for the apparent volume of the sample and makes determining the apparent density relatively simple. The briquette is outgassed in a vacuum oven at ~200 °C. It is allowed to cool inside the vacuum oven. Once removed, the briquette is massed using a precision balance and then placed in the test fixture.

4.6.2 Manometric Methane: Reservoir Procedure

This instrument is the only reservoir-type manometric instrument currently in use by the laboratory. The difference between the two methods is that instead of a valve between the dosing volume and the sample chamber; there is a regulator between the reservoir volume and the sample chamber, see figure 4.6.2. This allows the reservoir to maintain a high pressure and regulate it down to the pressure at which the analysis is to
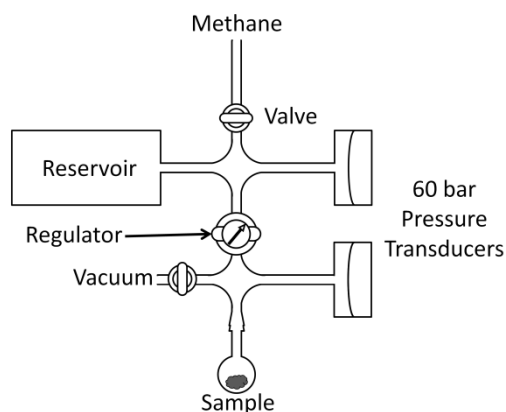
Figure 4.6.2. Left: Cartoon model of the test fixture apparatus. Right: Picture of the test fixture apparatus.

be performed. For an analysis, the reservoir is pressurized to 55 bar and then the regulator is adjusted to allow the desired pressure of methane into the sample chamber. Once the adsorption reaches equilibrium, the regulator then adjusts the sample chamber to the next desired pressure.

The advantage of a reservoir-type manometric set-up is the lack of the successive uncertainties. Each measurement has only the uncertainty of that measurement and does not depend on any of the prior measurements. The disadvantage of this method is that the maximum pressure that analysis can be performed at is lower than the maximum pressure of the reservoir. This is determined by the ratio of the sample chamber and reservoir volumes. As such the difference in maximum pressure can be substantial.

4.6.3 Manometric Methane: Critical Features

Similar to the other types of manometric instruments, the volumes of the reservoir and the sample chamber need to be determined accurately. In this case, the volumes were determined using liquid displacement of ethanol. The pressure transducers do not have to be as sensitive as with the dosing type instruments, but it is still best to have them as

accurate as possible. The transducers are read into a computer via LabVIEW which also performs the desired calculations.

One important characteristic of performing experiments with this apparatus is the time for equilibration. Although the methane should flow into the monolith fairly quickly, the exothermic effect of adsorption leads to temperature fluctuations. It takes longer for the monolith to cool, so ample time needs to be given for equilibration.

4.6.4 Manometric Methane: Sample Characteristics Determined

The purpose of the test fixture analysis is simply to see how well the monoliths store methane. A detailed derivation of the manometric equations used is given in appendix D. The total amount of methane stored is given by

$$M_{\text{Stored}} = V^{\text{Reservoir}} \left(\rho_{\text{Initial}}^{\text{Reservoir}} - \rho_{\text{Final}}^{\text{Reservoir}} \right) - \rho_{\text{Final}}^{\text{SampleChamber}} \left(V^{\text{SampleChamber}} - V_{\text{Apparent}} \right), \quad (4.9)$$

where $V^{\text{Reservoir}}$ is the volume of the reservoir, $\rho_{\text{Initial}}^{\text{Reservoir}}, \rho_{\text{Final}}^{\text{Reservoir}}$ are the densities of the methane in the reservoir before and after adsorption, respectively, $\rho_{\text{Final}}^{\text{SampleChamber}}$ is the density of the final adsorptive gas in the sample chamber, $V^{\text{SampleChamber}}$ is the volume of the sample chamber and V_{Apparent} is the apparent volume of the briquette determined from geometric measurements of the briquette. The densities are determined using the pressure and temperature of the gas and the NIST density table. The amount stored is the more straightforward measurement, but the excess adsorption can also be determined simply by replacing the apparent volume with the skeletal volume.

4.7 Gravimetric Supercritical Methane Sorption Methods

In addition to the manometric methane sorption measurements on full briquettes, methane uptake on powder samples is measured using a gravimetric technique. Gravimetric analysis is typically performed in an apparatus that uses a microbalance. This has drawbacks because only a small sample (<100 mg) is tested and buoyancy corrections are both necessary and complicated. Since the samples tested are on the order of grams, a new method of gravimetry can be performed. By using this new method, detailed procedure in appendix B, gram-sized samples can be analyzed, and any buoyancy correction is negligible. Figure 4.7.1 shows the sample cell and the 35 bar experimental set-up. Additionally, a 250 bar apparatus was built, figure 4.7.2, to see if the ANG storage would still be better than compressed natural gas (CNG). Since most natural gas storage and natural gas vehicles run at 3600 psi, 250 bar, the carbon may be useful for current natural gas storage. The 250 bar set-up also allows determination of the maximum in the excess sorption isotherm as well as extrapolating to zero excess
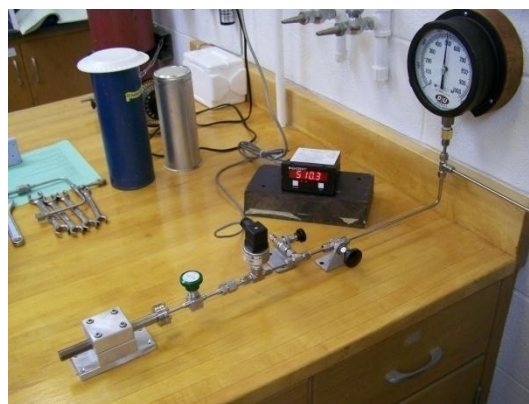
Figure 4.7.1. Left: Methane gravimetric procedure sample cell, ruler is 20 cm long. Right: Methane 35 bar gravimetric experimental set-up.

Figure 4.7.2. Left: 250 bar gravimetric methane uptake apparatus. Right: Gas booster to attain 250 bar methane.

adsorbed mass. These values can be used to determine more about the adsorbed methane physics.

4.7.1 Gravimetric Methane: Sample Preparation

Typical samples are on the order of grams, anything less than 0.5 grams and the uncertainty becomes a concern. The sample is massed using the precision balance before outgassing to verify that some moisture and air was removed afterwards. A typical outgassing is 10 minutes under vacuum at room temperature followed by 2 hours at 400 °C. Glass wool is used above the sample to reduce elutriation of the powder into the sample valve.

4.7.2 Gravimetric Methane: Gravimetric Method

A detailed experimental procedure for this set-up is given in appendix B. In order to calculate the gas uptake values, four mass measurements are required: the evacuated sample cell, M_C , the sample cell with the gas to be analyzed (CH_4) at the desired temperature and pressure, $M_{C,G}$, the evacuated sample cell with outgassed sample, $M_{C,S}$,

and the sample cell with sample and gas to be analyzed at the desired temperature and pressure, $M_{C,S,G}$. Using these four mass measurements the gas uptake is determined.

$$M_{Ads}^{Ex} = M_{C,S,G} - M_{C,G} - \left(M_{C,S} - M_C\right)\left(1 - \frac{\rho_{Gas}}{\rho_{Skeletal}}\right) \qquad (4.10)$$

$$M_{Stored} = M_{C,S,G} - M_{C,G} - \left(M_{C,S} - M_C\right)\left(1 - \frac{\rho_{Gas}}{\rho_{Apparent}}\right) \qquad (4.11)$$

The density of the non-adsorbed gas, ρ_{Gas}, is obtained from the NIST Chemical WebBook and is determined for the specific pressure and temperature of the gas [54]. The other two densities used to determine the mass of excess adsorbed gas and stored gas, respectively, are the skeletal density, $\rho_{Skeletal}$, and the apparent density, $\rho_{Apparent}$, of the sample, see section 4.3.3 for an explanation of the volumes included in these densities. The skeletal density is determined using helium pycnometry, amorphous carbons will have a skeletal density $1.9 \leq \rho_{Skeletal} \leq 2.3 \frac{g}{cm^3}$. The apparent density is determined using the skeletal density and the porosity of the sample, see appendix A.

4.7.3 Gravimetric Methane: Critical Features

Similar to the requirement of manometric instruments to have accurate pressure transducers, the key to a good gravimetric experiment are the mass measurements. One issue inherent to most gravimetric apparatus is buoyancy correction. Fortunately, the total buoyancy correction when applied to this set-up is negligible, see appendix f. The primary constraint on this set-up is that every piece of the sample cell must be the same through-out the experiment. Therefore any copper gasket or polymeric o-ring must be

the same one throughout the entire experiment. This becomes a concern as it increases the chance for leaks.

4.7.4 Gravimetric Methane: Sample Characteristics Determined

The two set-ups primary purpose is to determine the amount of methane stored for mass sample and for volume sample. This is useful to determine the quality of the carbon as a methane sorbent. Yet, methane isotherms can also determine the sample pore structure and some information about the methane sorption physics.

In order to properly apply certain theories to the experimental data, the excess adsorbed gas needs to be converted to absolute adsorbed gas. There are two assumptions that can be used to determine the mass of the absolute adsorbed gas. It can be assumed that either we know the volume of the adsorbed film, V_{Ads}, or that we know the density of the adsorbed film, ρ_{Ads}. In order to use the volume method, we assume that the volume of the adsorbed film is approximately equal to the volume of the nanopores (pores less than 1 nm in pore dimension), V_{Nanopore}, in the sample. In order to determine the nanopore volume of the sample, a subcritical nitrogen isotherm analysis is performed on the sample, see section 4.5. The nanopore volume is then determined via density functional theory [55]. In order to use the density method, the density of the adsorbed layer is determined using molecular dynamics or Monte Carlo simulations. The detailed derivation is in appendix C.

$$M_{\text{Ads}} = M_{\text{C,S,G}} - M_{\text{C,G}} - \left(M_{\text{C,S}} - M_{\text{C}} \right)\left(1 - \frac{\rho_{\text{Gas}}}{\rho_{\text{Skeletal}}} \right) + V_{\text{Nanopore}}\rho_{\text{Gas}} \qquad (4.12)$$

$$M_{\text{Ads}} = \left[M_{\text{C,S,G}} - M_{\text{C,G}} - \left(M_{\text{C,S}} - M_{\text{C}} \right)\left(1 - \frac{\rho_{\text{Gas}}}{\rho_{\text{Skeletal}}} \right) \right]\left(1 - \frac{\rho_{\text{Gas}}}{\rho_{\text{Ads}}} \right)^{-1} \qquad (4.13)$$

Once the excess sorption isotherm has been converted to absolute sorption, two types of sample characterization can be performed. NLDFT can be applied to the isotherm to determine the pore sized distribution. Also, the Langmuir theory can be applied to determine the methane binding energy.

Chapter 5: Experimental Results

5.1 Electron Microscopy Results

Both field emission scanning electron microscopy (FESEM) and transmission electron microscopy (TEM) analysis was performed on three samples: briquette 46, S-33/k, and S-56. These analyses were meant to be only qualitative in nature, revealing more information about the structure of the carbons. Secondary electron images of sample S-33/k from the Hitachi S-4700 FESEM instrument are shown in figure 5.1.1. The 10,000x image reveals that the sample has very few macropores, only one seen in the center of the image. The same macropore can be seen in the other image at 130,000x. The zoomed in image of the ~200 nm wide macropore reveals that it is an entrance to a porous network.

The microtomed slice of S-56 for use on the TEM were also analyzed with the FESEM, see figure 5.1.2. These images reveal that S-56 is markedly more macroporous than
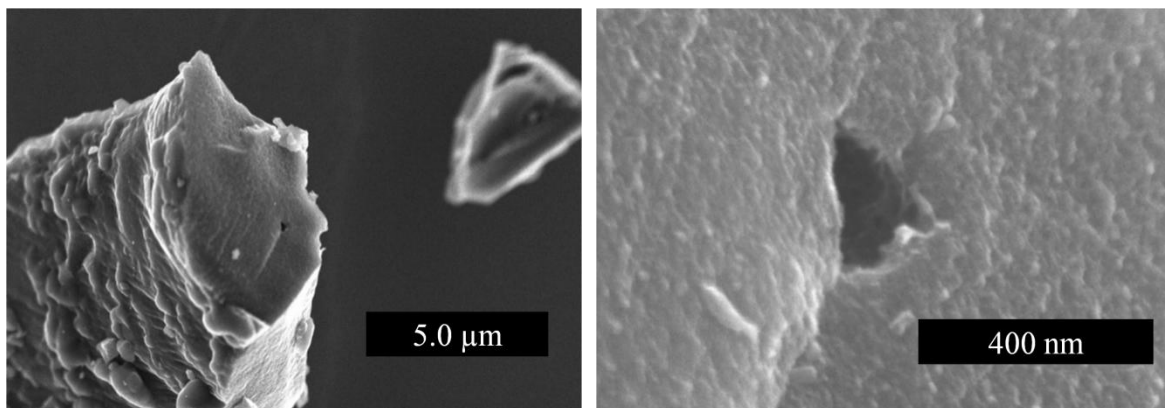
Figure 5.1.1. Secondary electron SEM images showing the hierarchy of pores. Left: Sample S-33/k at 10,000x. Right: Pore seen in center of left image at 130,000x. Width of the black box is the length it contains. Both images were with 5 keV electrons and 3 mm working distance.
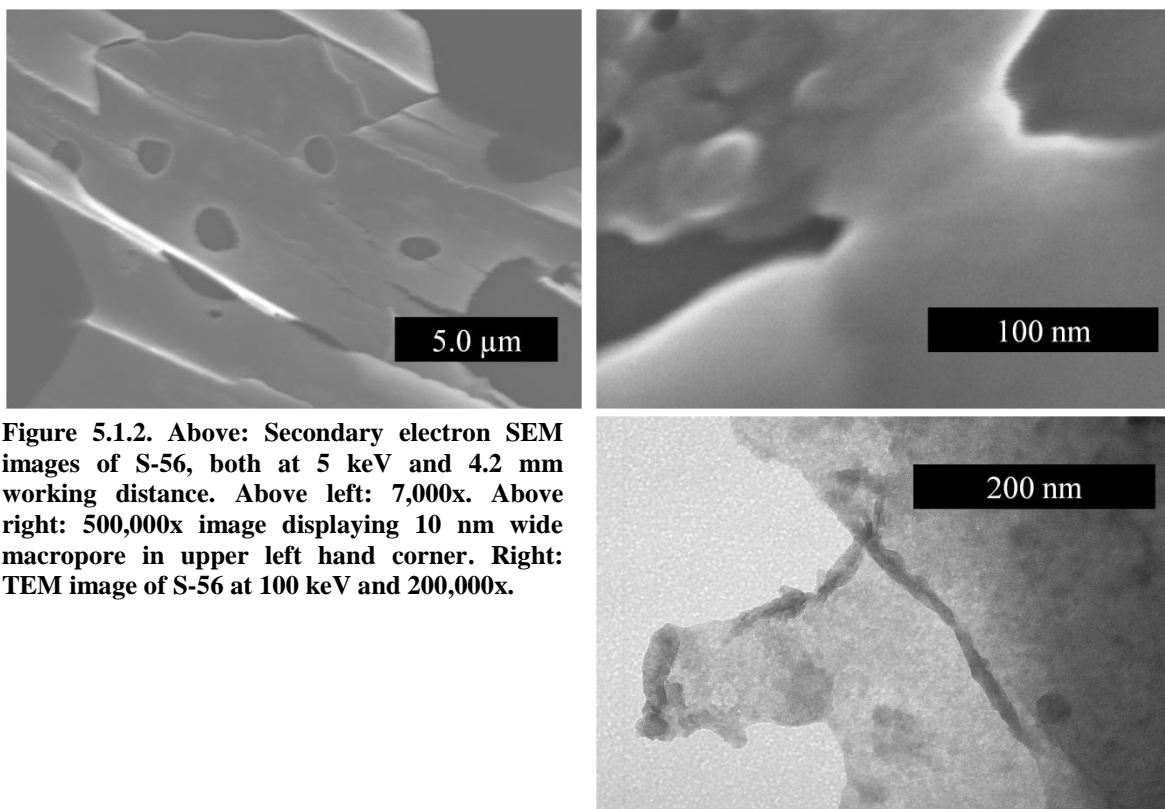
Figure 5.1.2. Above: Secondary electron SEM images of S-56, both at 5 keV and 4.2 mm working distance. Above left: 7,000x. Above right: 500,000x image displaying 10 nm wide macropore in upper left hand corner. Right: TEM image of S-56 at 100 keV and 200,000x.

S-33/k. TEM images of sample S-56 from the JEOL 1200EX TEM are shown in figure

5.1.3. Unfortunately, the TEM was unable to see the porous network of the carbons as

was expected. The TEM analysis does reveal that the macropores in the sample S-56 are

round in cross-section. This is not necessarily inconsistent with the model of slit-shaped

micropores. Additionally, a large amount of macropores may help with gas kinetics into

the micropores if they act as entrances to a fractal network of pores. They will, however,

lower the mass of gas stored for volume of sample.

5.2 Chemical Composition Analysis Results

Three chemical composition analysis techniques were performed on the activated

carbons: energy dispersive spectroscopy (EDS), inductively coupled plasma-atomic

emission spectroscopy (ICP-AES), and x-ray fluorescence spectroscopy (XRF). EDS

was used to analyze only one sample, briquette 46. This sample showed some interesting structures when using the back-scatter detector on the FESEM, see figure 5.2.1. Back-scatter electrons have atomic number dependence, so different grayscales can mean different mean atomic numbers. In addition to the carbon structure, there appears to be some cubic crystals on the surface of the carbons. In order to determine the composition of these crystal structures, EDS was used on a section of the sample, the results of which are given in figure 5.2.2. Point 1 has a large carbon peak with small sodium, chlorine and oxygen peaks. Consequently, even the darkest gray regions assumed to be pure carbon are actually carbon with a small amount sodium chloride and possibly some oxide compounds. Point 2 has strong sodium and chlorine peaks with small carbon and potassium peaks. Point 3 has strong carbon, sodium, potassium, and chloride peaks and a weak oxygen peak. Comparing the chlorine peak height from points 2 and 3 reveals that
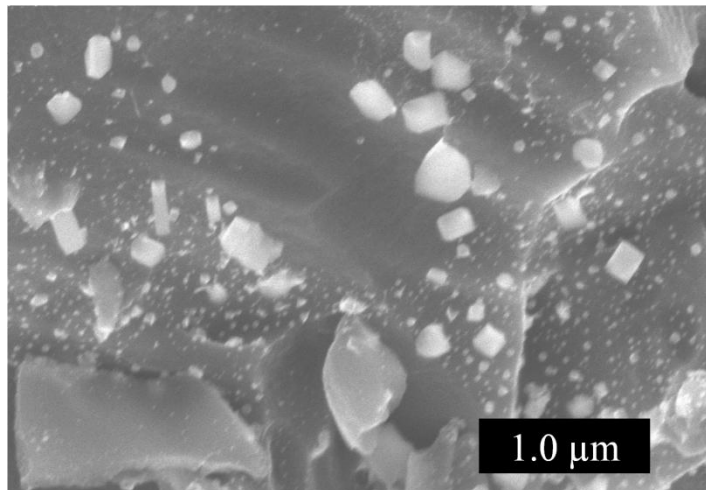
Figure 5.2.1. Back-scatter electron image of briquette 46 (5 kV, x30k), the crystals shown are assumed to be sodium chloride salt because of the results from the EDS analysis presented in figure 5.1.2.

70
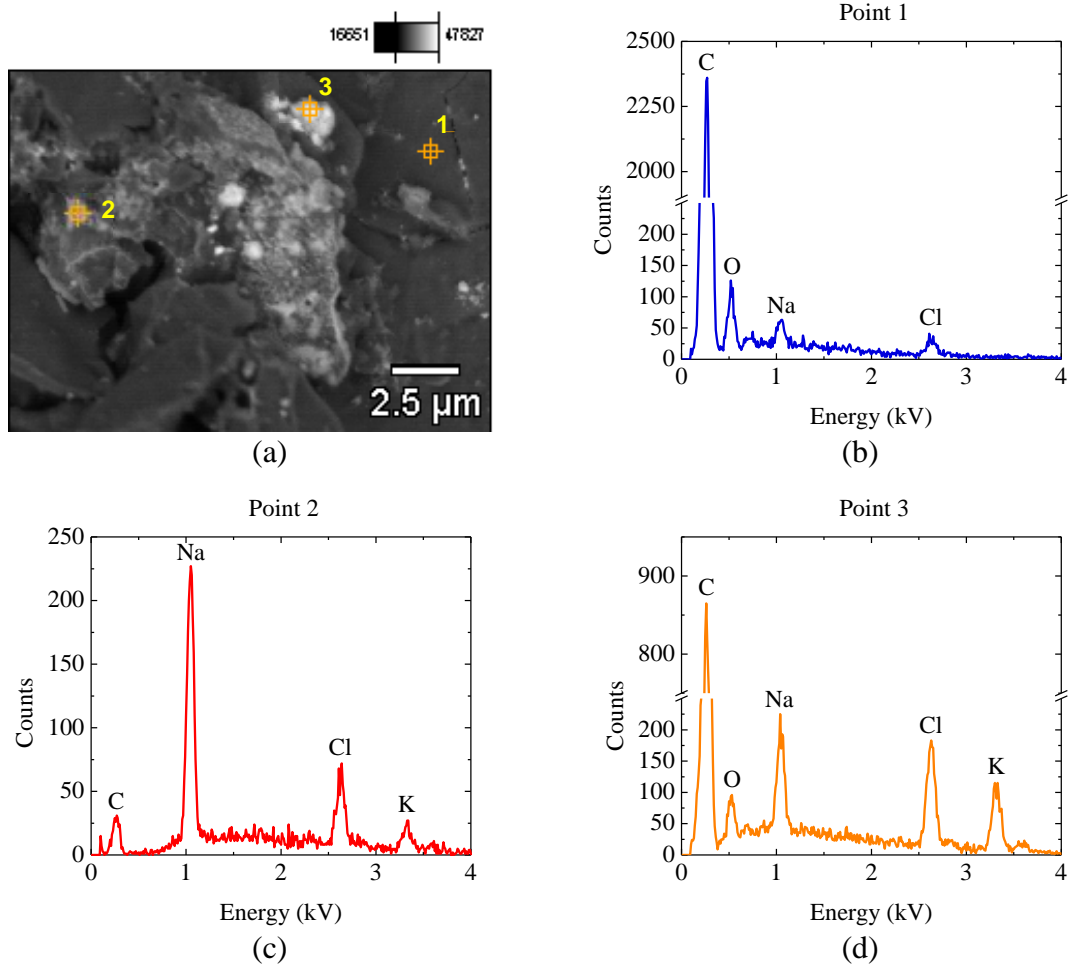
Figure 5.2.2. (a) Back-scatter electron image showing locations of EDS analysis points. (b) Point 1, very strong carbon peak. (c) Point 2, Large sodium peak, in conjunction with chlorine peak, this infers that the chemical compound is sodium chloride. (d) Point 3, This has a larger carbon peak than 2, which may be due to carbon around the point, it also has a stronger chlorine and potassium peak than 2, but a comparable sodium peak, this implies that there may be a combination of sodium chloride and potassium chloride salts.

point 2 is likely sodium chloride, whereas point 3 contains both sodium chloride and potassium chloride. Unfortunately, both sodium chloride and potassium chloride occur as cubic crystals, so it is not evident whether the crystals in figure 5.2.1 are sodium chloride or potassium chloride. The origin of the potassium and oxygen could be from the potassium hydroxide used during activation. The oxygen most likely is left in the carbon as a metal hydroxide. Although no metals were found using EDS, the limitations of the technique may be at fault. The chlorine may come from the vinylidene chloride

71

($C_2H_2Cl_2$) used as a binder in the briquette manufacture. It is more difficult to explain the presence of sodium. Sodium may come from the starter corncob, but it is unlikely. The more likely source of the sodium and chlorine is the tap water used for the activation process as well as for the final washing of the sample.

In addition to EDS work on briquette 46, ICP and XRF analysis were performed on sample S-33/k, table 5.1.1. Both analyses were performed on the ash content after the carbon C, H, O, and N matrix was burned off. Unfortunately, the XRF analysis did not determine what percentage of the sample was ash. As a result, the XRF results have been normalized using the ash percentage found by the company that performed ICP-AES, 1.469 %. As can be seen from the results, S-33/k contains fair amount of chromium and iron. These more than likely originated in the steel vessel used for the activation process. Recent activated carbons produced in alumina vessels do not show the same iron and chromium content.

Table 5.2.1. ICP-AES and XRF results on sample S-33/k. The XRF percentages were weighted using the ash percent determined during ICP-AES analysis.

Element	C	Mg	Ca	Cr	Mn	Fe	Ni	Cu
Mass percent (%)								
XRF	98.531	0.094	0.096	0.417	0.030	0.294	0.011	0.043
ICP-AES	98.531	0.143	0.112	0.876	0.065	0.819	0.029	0.146
Atomic percent (%)								
XRF	99.7	0.047	0.029	0.097	0.007	0.064	0.002	0.008
ICP-AES	99.5	0.028	0.072	0.179	0.006	0.206	0.015	0.034

5.3 Manometric Subcritical Nitrogen Sorption Results

Over 50 samples were analyzed on the Quantachrome Autosorb 1-C manometric subcritical nitrogen sorption apparatus, table 5.3.1. For the purposes of these results, the

Table 5.3.1. List of most carbons analyzed using subcritical nitrogen adsorption.

Sample Name	Nanopore Volume from NLDFT [cc/g]	Total Pore Volume from NLDFT [cc/g]	Total Pore Volume from ~0.99 p/p$_0$ [cc/g]	Porosity Direct from Isotherm [%]	Surface Area from NLDFT [m2/g]	BET Total Surface Area [m2/g]
S-56	0.77	1.78	1.97	80%	3500	3500
S-58	0.27	2.16	2.37	83%	2400	3500
S-54	0.22	2.01	2.22	82%	2200	3300
Batch 5.32	0.10	1.94	2.11	81%	3000	3200
S-62	0.34	1.62	1.80	78%	2400	3200
S-52	0.52	1.72	1.91	79%	2800	3100
S-53	0.18	2.04	2.25	82%	1900	3000
Batch 5.2	0.38	1.31	1.47	75%	2100	3000
S-59	0.20	1.85	2.02	80%	1900	3000
Batch 5.31	0.18	1.83	2.07	81%	1852	3000
B-1	0.27	1.66	1.82	78%	2088	2900
Batch 5.1	0.76	1.69	1.88	79%	3200	2600
B-21/K	0.39	1.26	1.40	74%	2100	2500
3K-5B	-	-	-		-	2400
S-55	0.43	1.13	1.26	72%	2200	2200
C7	-	-	-		-	2200
P-1	0.18	1.30	1.42	74%	1500	2000
S-33K	0.39	1.09	1.22	71%	2100	2000
B-21/K'	-	-	1.00	67%	-	1700
S-22	-	-	-		-	1500
S-20	-	-	-		-	1400
S-29	-	-	-		-	1200
C1	0.17	0.85	0.94	65%	1100	1200
S-60	0.44	0.64	0.70	58%	1600	1200
S-21	-	-	-		-	1200
S-51	0.43	0.68	0.76	60%	1600	1100
S-28	-	-	-		-	1100
S-23	-	-	-		-	1000
C3	0.16	0.65	0.72	59%	900	1000
C2 50% Acid	0.12	0.64	0.71	59%	800	1000
S-27	-	-	-		-	900
S-50	0.35	0.55	0.60	55%	1300	800
S-25	-	-	-		-	800
S-36	0.25	0.39	0.43	46%	1000	700
S-18	-	-	-		-	700
S-15	-	-	-		-	700
S-14	-	-	-		-	600
B-18	0.19	0.41	0.45	47%	500	600
S-30	0.25	0.38	0.41	45%	1100	600
S-35	0.21	0.36	0.40	44%	800	600

analysis has been limited to BET and DFT theories. In order to expedite the process of sample optimization, some of the isotherms were limited to the BET pressure range 0.01-0.03 p/p_0. DFT analysis, however, is best with isotherms containing both lower pressures, 10^{-6} p/p_0, and a desorption isotherm. Especially, in case of a type H_1 hysteresis it is extremely important to have a desorption isotherm. Furthermore, the DFT analysis does require correction for thermal transpiration to attain the most accurate results. The thermal transpiration correction was performed with a nitrogen diameter of 3.54 nm and the inner diameter of the cell used, generally 7mm.

Even before the isotherm is analyzed with any adsorption theory, determining the type of isotherm and the presence or absence of a hysteresis can reveal significant characteristics about the material. It is always best to look at the raw nitrogen isotherm before determining what type of analysis is best. Figure 5.3.1 displays two typical isotherms of different types. Sample S-33/k has a type I isotherm with no hysteresis. Consequently, just from the raw isotherm it is apparent that S-33/k is highly microporous. Since the knee is not sharp for a type I isotherm, it is classified as a type Ib. Type Ib isotherms are indicative of larger micropores that exhibit cooperative filling. Sample S7, however, displays a type IV isotherm with a type H_4 hysteresis. It follows that S7 should be mesoporous or larger microporous slit-shaped carbon. The knee on the S7 isotherm is also very sharp, so if it has any micropores, they should be narrow as it displays only primary micropore filling. Also presented in the figure are the QSDFT pore size distributions (PSD's) for the two samples with results consistent with the isotherm types.
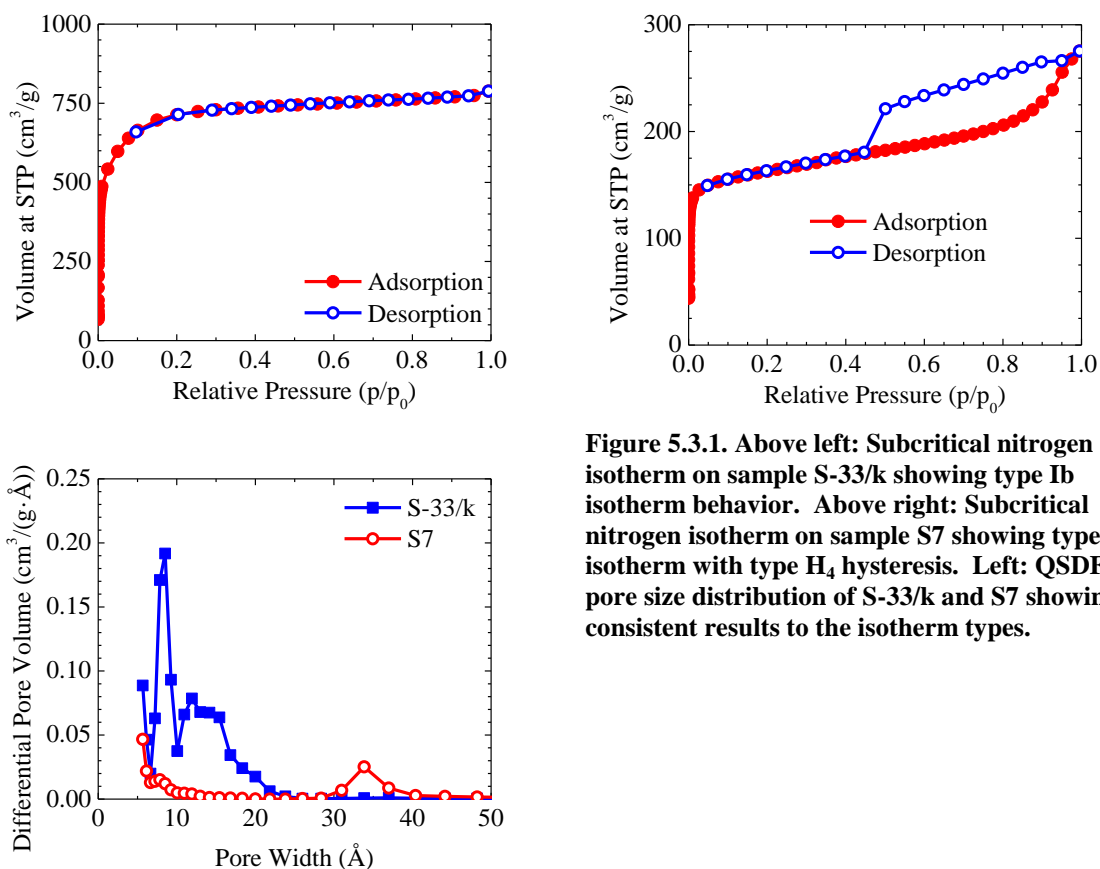
Figure 5.3.1. Above left: Subcritical nitrogen isotherm on sample S-33/k showing type Ib isotherm behavior. Above right: Subcritical nitrogen isotherm on sample S7 showing type IV isotherm with type H_4 hysteresis. Left: QSDFT pore size distribution of S-33/k and S7 showing consistent results to the isotherm types.

The consistence between the isotherms and the QSDFT PSD's is important to determining the validity of the technique. QSDFT is still considered a new technique and as such needs to be verified against expected results. As an additional means of confirmation, the QSDFT technique is used to compare the results from samples that were manufactured using the same process. This will not only verify the technique, but also the reproducibility of the carbon activation procedure. Results from three different batches of carbon treated with the same method and with 4:1 KOH:Carbon char ratio are shown in figure 5.3.2. As can be seen, the results agree quite well and as such confirm both the validity of the QSDFT method as well as the carbon manufacture.
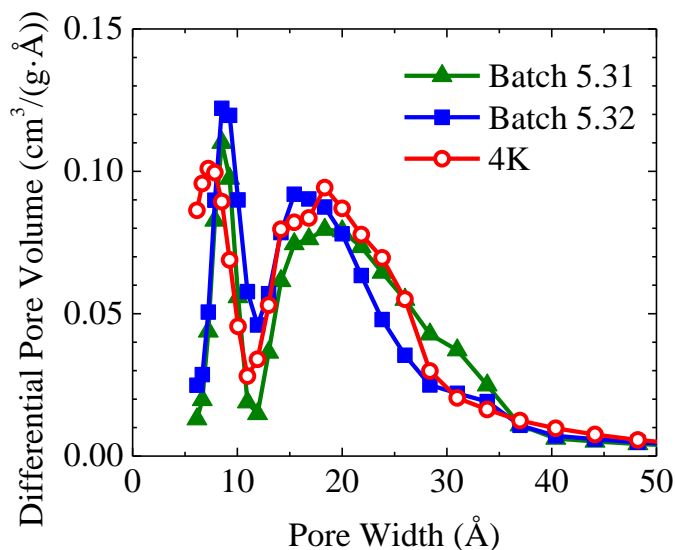
Figure 5.3.2. QSDFT PSD's for three carbons produced using the same activation process using corncob precursor.

The three methods used to analyze the nitrogen sorption isotherms (BET, NLDFT, QSDFT) are compared in table 5.3.2. The surface areas can vary as much as ~500m^2/g. Consequently, all surface areas determined by these techniques are classified only as nominal surface areas.

Table 5.3.2. Comparison of the three analysis techniques: BET, NLDFT and QSDFT on S-33/k and Batch 5.1.

	Sample					
	Batch 5.1			S-33/k		
	BET	**NLDFT**	**QSDFT**	**BET**	**NLDFT**	**QSDFT**
Surface Area (m^2/g)	3080	3160	3650	2640	2150	2420
Total Pore Volume (cm^3/g)		1.69	1.72		1.09	1.12
Porosity (%)		77	77		69	69
Pore Volume < 10 Å (cm^3/g)		0.76	0.9		0.39	0.58
Pore Width Mode (Å)		7.5	6.1		11.3	8.5

5.4 Supercritical Hydrogen Sorption Results

Hydrogen sorption analysis was performed on the rapid-screening hydrogen sorption (RHS) instrument and the Hiden HTP1-V. The results from the rapid-screening instrument are for qualitative purposes only. They are used to determine which samples

are good enough for analysis on the Hiden HTP1-V as well as other instruments in the laboratory. Results of one sample run on the RHS are presented in figure 5.4.1. It is apparent from this analysis that the RHS has the capability to reliably determine a difference in excess mass adsorbed hydrogen for mass samples as small as 1 g/kg. Unfortunately, there were a couple of runs where leaks occurred. Consequently, more work needs to be done to determine changes to the equipment as well as procedural changes that can reduce the occurrences of leaks.

For the purposes of this research, primary results will focus on only two samples: S-33/k and Batch 5.1. Sample S-33/k was not analyzed with a HTP1 instrument. It was sent to Hiden Isochema; where it was analyzed on a Hiden Isochema IGA-001. The IGA-001 is a microbalance-type gravimetric instrument. As a result, buoyancy corrections are difficult; and can cause an overestimate of the sorption. Despite this
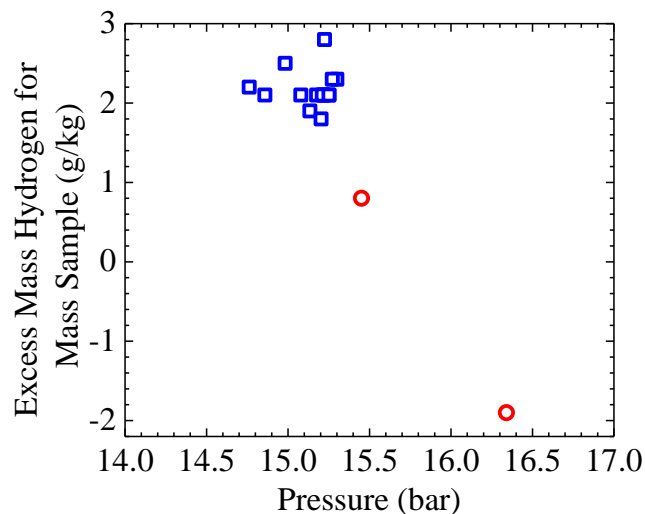
Figure 5.4.1. Results from the RHS on sample 3K. The two red circles are values from runs where leaks occurred. The cluster of blue rectangles reveals the precision of the instrument.

Table 5.4.1. Validation of H2 storage in new corncob-based nanoporous carbon from three independent laboratories. Temperatures departing from the ones in the table header are listed in parentheses.

	77 K, 50 bar	293 K, 50 bar	293 K, 80 bar
Batch 5.1, U. Missouri	–	1.0-1.1 wt%	–
Batch 5.1, Hiden	7.0 wt% (83 K)	1.1 wt% (303 K)	1.8 wt% (303 K)
S-33/k, U. Missouri	7.8-9.1 wt%	0.9-1.1 wt%	–
S-33/k, Hiden	7.6 wt%†	1.1 wt%†	1.6 wt%†
S-33/k, NREL	~8 wt%	1.4-1.6 wt%	2.1-2.4 wt%

† Values extrapolated from isotherms

concern, the results from this sample were validated in three different laboratories, see table 5.4.1. Batch 5.1 was analyzed by Hiden Isochema on an HTP1-V manometric instrument. The hydrogen isotherms for both samples are highly reversible, showing no hysteresis between the adsorption and desorption branches, see figure 5.4.2.
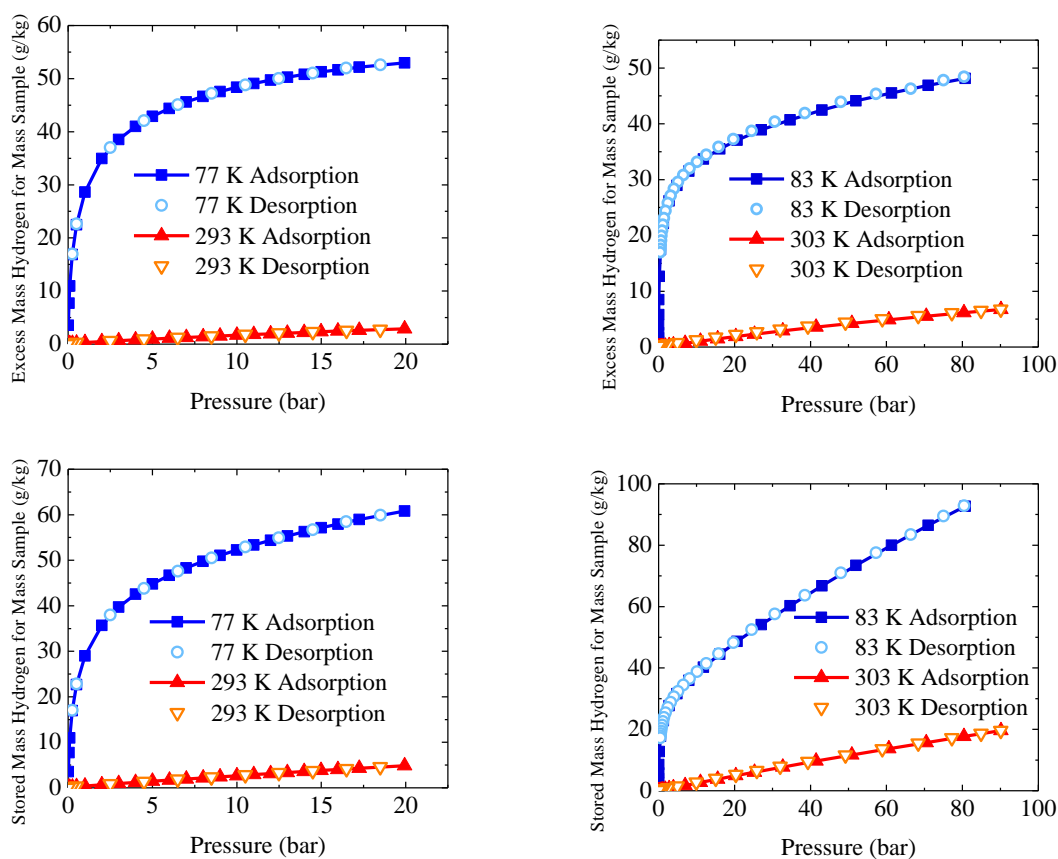
Figure 5.4.2. Excess hydrogen adsorption (top) and total amount stored (bottom) for samples S-33k (left), and Batch 5.1 (right).

One noteworthy aspect of the Batch 5.1 excess adsorption isotherm is the lack of a noticeable maxima and linear decrease thereafter. This can be explained by having a distribution of binding energies due to a distribution of pore widths, as is shown in chapter 6.

5.5 Manometric Supercritical Methane Sorption Results

The manometric supercritical methane sorption apparatus (methane test fixture) has been used to measure the methane uptake of numerous briquettes. As part of the natural gas project, a Kansas City fleet vehicle was modified to use adsorbed natural gas stored in these briquettes, see figure 2.3.2. Over 200 briquettes were produced by Dr. Galen Suppes' group. Several briquettes were selected from the batches produced for methane uptake studies. The results of one of the best briquettes, briquette 46, are given in figure 5.5.1.
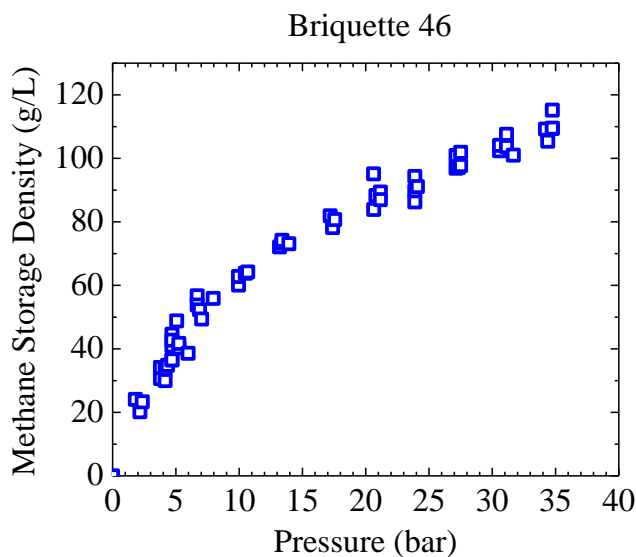
Figure 5.5.1. Manometric, room temperature stored methane isotherm on briquette 46.

The test fixture has been modified and optimized since the data for this briquette was taken. The test fixture now has a better LabVIEW interface. Furthermore, the test fixture has been modified so as to reduce the occurrences of leaks. More details of the modifications and future research planned for this instrument are detailed in chapter 7.

5.6 Gravimetric Supercritical Methane Sorption

Gravimetric supercritical methane uptake measurements were performed on over 70 samples, see table 5.6.1. The methane uptake was measured on these samples at room temperature and 35 bar. The choice of 35 bar (~500 psi) is outlined in section 1.2. The excess mass methane for mass sample was calculated assuming $\rho_{\text{Skeletal}} = 2.0\,\text{g}/\text{cm}^3$. The default value of $\rho_{\text{Apparent}} = 0.5\,\text{g}/\text{cm}^3$ was used to calculate the amount stored for mass, volume and volume for volume. More detailed analysis, as presented in chapter 6, utilized results from nitrogen isotherms to determine a better estimate of the apparent density.

Table 5.6.1. Methane uptake results for 70 samples at 35 bar and room temperature.

Sample Name	Excess Mass for Mass [g/kg]	Stored Mass for Mass [g/kg]	Stored Mass for Volume [g/L]	Stored Volume for Volume [L/L]
AN-CNPCA	205	242	121	185
4K	203	240	120	184
S-59	201	238	119	182
3K-5B-A	198	235	118	180
4K-5B	197	235	117	180
AN-Batch-F	197	234	117	179
Batch 5.32	194	232	116	177
S-33K	193	231	115	176
AN-A-2	193	230	115	176
S-52	193	230	115	176
3K-UBM	192	229	115	175
N32K	191	229	114	175
3K-BM (no H2O)	190	227	114	174
C7	186	223	112	171
S-21K	185	222	111	170
S-29K	185	222	111	170
3K-5B	182	220	110	168

Sample Name	Excess Mass for Mass [g/kg]	Stored Mass for Mass [g/kg]	Stored Mass for Volume [g/L]	Stored Volume for Volume [L/L]
S-24K	180	218	109	167
AN-A-1	180	218	109	167
S-58	179	217	108	166
2K-UBM	178	216	108	165
Batch 5.31	176	214	107	163
S-62	175	212	106	162
C6 NaOH	170	207	104	158
3NaOH	170	207	104	158
C7-2K	168	205	103	157
AN-B-2	167	204	102	156
Batch 5.4	167	204	102	156
Batch 5.2	158	195	98	150
4K-5B-A	155	193	96	147
S-56	146	183	92	140
S-40	143	180	90	138
S-55	141	179	89	137
3.5K-5B-A	136	173	87	132
Batch 5.1	135	172	86	132
AN-B-1	123	160	80	123
S-61 (No H3PO4)	122	160	80	122
Darco 2	119	157	78	120
Darco 2.25	117	154	77	118
2.5K	108	145	73	111
ATMI	92	129	65	99
GSN13 (Metal)	82	119	60	91
S-36	77	114	57	87
S-29	73	110	55	85
GSN7	69	106	53	81
S-28	68	106	53	81
3LiOH	60	97	49	74
S-27	59	96	48	74
S-49	56	94	47	72
S-13	51	88	44	68
S-16	48	85	43	65
S-18	46	83	42	64
B-14	37	75	37	57
S-14	35	73	36	56
GSN6	35	73	36	55
IS3	33	71	35	54
GSN9	32	69	35	53
GSN12 (No Metal)	27	64	32	49
GSN10	25	62	31	48
GSN2 (Granular)	22	60	30	46
GSN12 (Metal)	22	59	30	45
GSN2 (Powder)	22	59	30	45
GS-1	21	58	29	45

Sample Name	Excess Mass for Mass [g/kg]	Stored Mass for Mass [g/kg]	Stored Mass for Volume [g/L]	Stored Volume for Volume [L/L]
AN-SNPCA	20	58	29	44
S-41	16	54	27	41
GSN11	11	49	24	37
GSN4	8	46	23	35
S-12	6	44	22	33
GSN3 (Powder)	2	40	20	30
GSN5	1	38	19	29

Samples of particular interest had additional data taken to determine adsorption isotherms, see figure 5.6.1. The measurements of methane isotherm using this method are time consuming. A typical reliable methane isotherm can take as long as one week to perform the analysis. Also shown in figure 5.6.1 is a plot of the storage density isotherm for one of the best performing samples, S-33/k. From the figure, it is apparent that the use of adsorbed methane can actually store almost five times the amount that compressed natural gas can. The current best performer stores 121 grams of methane for liter of carbon. These carbons are currently the only carbon material being produced that meets or exceeds the 2001 DOE adsorbed natural gas storage goals.
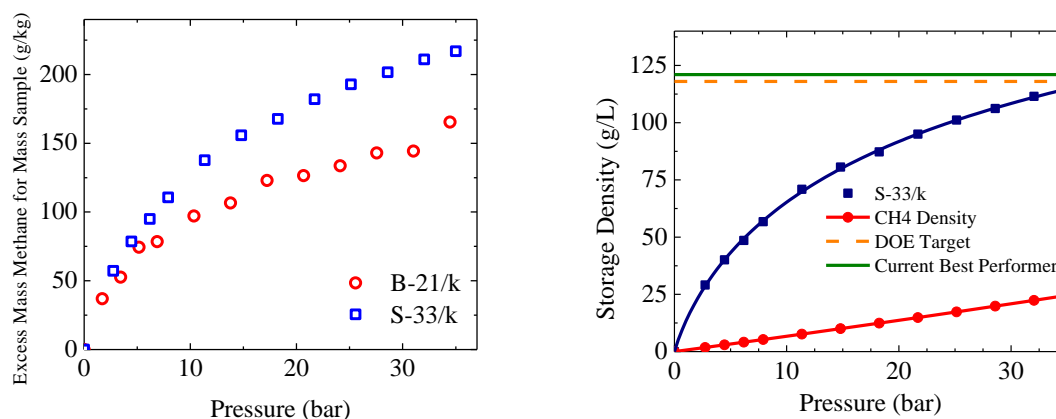
Figure 5.6.1. Left: Gravimetric, room temperature excess methane adsorbed isotherms on samples B-21/k and S-33/k. Right: Comparison of S-33/k ANG and CNG capabilities.

In addition to relaying more information about the methane sorption characteristics of the samples; the methane sorption isotherms were also analyzed using non-local density functional theory. Figure 5.6.2 shows comparisons of the pore size histograms from NLDFT applied to the supercritical methane isotherm and the subcritical nitrogen isotherms for sample S-33/k. The results of the two methods agree quite well. This is very interesting when the two methods are compared. The methane sorption isotherm is performed with supercritical gas and the adsorbate is likely only forming a monolayer of coverage. Nitrogen analysis is performed with a subcritical gas that fills the pores with liquid density nitrogen. Additionally, the size of the methane molecule is slightly smaller than the molecular size of nitrogen. This last fact may explain the small differences in the results of the two techniques. Further information about the methane sorption physics was also determined from the isotherms, see section 6.5.
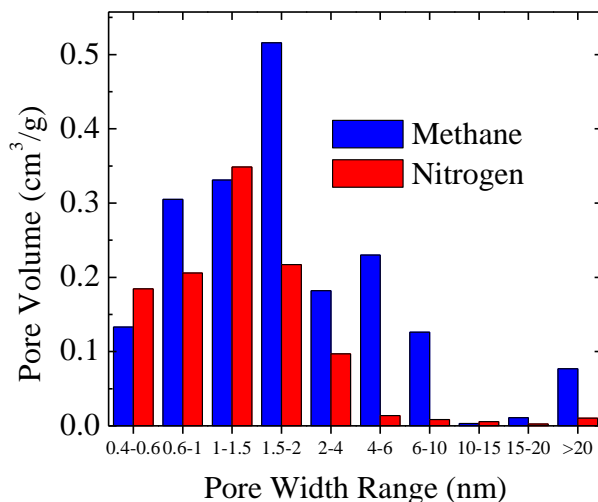
Figure 5.6.2. Comparison of methane and nitrogen pore size distributions of S-33/k as determined by applying non-local density functional theory to the two gases.

Chapter 6: Conclusions

6.1 Conclusion I: Carbon Precursors

One premise with highly KOH activated carbons is that they lose the original structure of the precursor used. If this were true, then activated carbon made from different precursors with the same activation procedure should have similar pore characteristics. As will be seen in the next section, the further activation of the precursor with increasing ratios of KOH simply modifies the pore structure and does not completely destroy it. Additionally, a polymeric precursor, vinylidene chloride ($C_2H_2Cl_2$) was chosen for comparison to the corncob precursor. Vinylidene chloride polymerizes to form polyvinylidene chloride. Once this polymer is heated, the hydrogen and chlorine escapes as hydrochloric acid (HCL) and in the process it drills pores in the carbon. Carbons produced from this precursor are typically called PVDC type or saran (named for the plastic made with PVDC) type carbons. PVDC carbons are well-known to produce small pore sized distributions of slit-shaped pores.

Figure 6.1.1 shows comparisons of the nitrogen sorption data of two carbons, 3K and S4. Sample 3K was produced using corncob precursor and S4 was produced using PVDC. The samples were both activated with 3:1 KOH:carbon ratio using the same preparation method. The only difference between the two activation processes was the production of the precursor. Corncob, like all lignocellulose materials, produces the best activated carbon when pre-treated. For sample 3K the corncob was soaked in phosphoric acid and charred prior to KOH activation. The PVDC carbon does not need to be treated with phosphoric acid, so the polymer was simply charred prior to activation.

84
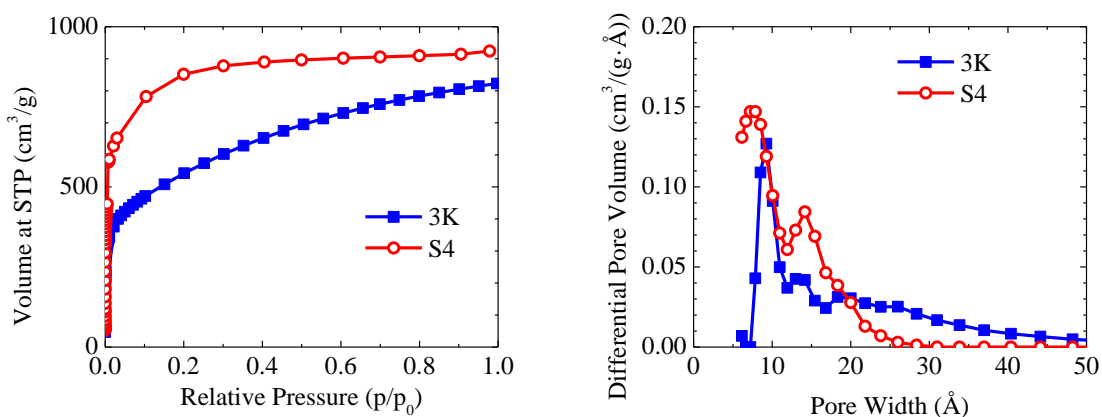
Figure 6.1.1. Left: Nitrogen sorption isotherms for samples 3K and S4. Right: Pore size distribution determined using QSDFT of the same samples.

From the comparison of these two carbons, S4 is seen to maintain a narrower pore size distribution indicative of PVDC type carbons. Sample 3K has a significant amount of mesopores which are seen in the corncob type carbons. Therefore, it is concluded that different precursors will in fact produce activated carbons with substantially different characteristics even if the activation process is the same. The belief held by some in the field is that with this amount of KOH activation, there should not be as much of an influence by the precursor chosen. These results show that this is not the case. The carbons produced from corncob have remarkable characteristics not seen in carbons produced using other precursors. These results lend credit to the usefulness of corncob as a precursor.

6.2 Conclusion II: KOH Activation Effect on Pore Structure

The pore characteristics should depend strongly on the concentration of KOH used to activate the carbons. The generally held assumption is that KOH causes the widening of pores through the expansion of carbon monoxide and carbon dioxide gas at the high temperatures used. Consequently, more KOH should cause the pores to increase

in size. This should result in a decrease in the nanoporosity. Results showing this effect are shown in figure 6.2.1. It was also hypothesized that increasing the KOH would increase the porosity; the results, however, show no noticeable dependence of porosity on the KOH concentration, up to 4:1 KOH ratio. More results are needed to confirm this fact. If it holds true, it is a very interesting result. It means that although the KOH is widening the pores, the percent of the apparent volume occupied by pores is not noticeably changing. This can happen if the KOH treatment is actually causing the apparent volume to increase as it is increasing the pore volume. This is consistent with the idea that the KOH activation widens the pores and does not simply remove carbon from the structure. For example, if the KOH activation increased the pore space by 20%, if the apparent volume also increases by 20%, the change in porosity can be 5%.

The full nitrogen isotherms of samples with different KOH ratio are shown in figure 6.2.2. The 2:1 KOH ratio carbon isotherm shows primary micropore filling due to
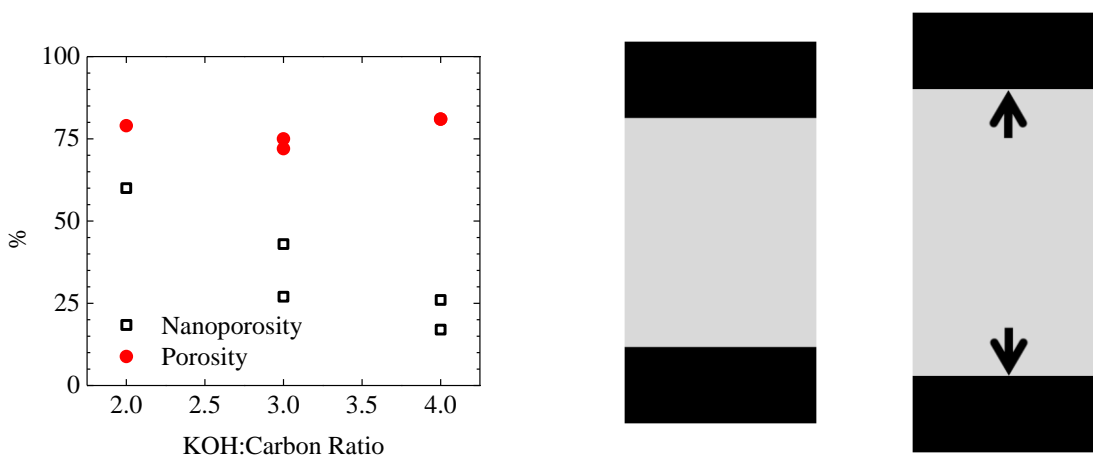
Figure 6.2.1. Left: Nanoporosity and porosity dependence on KOH concentration. Right: Cartoon depicting the KOH increasing the pore volume as well as the apparent volume. The pore volume increases by 20%, but the porosity only increases by 5%.
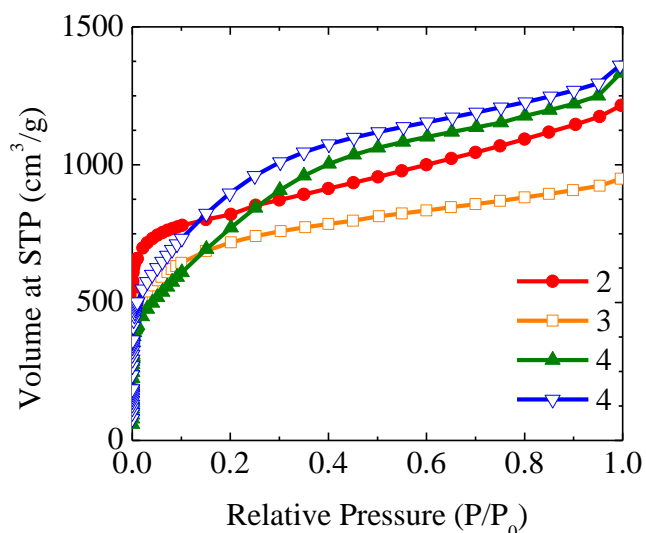
Figure 6.2.2. Subcritical nitrogen isotherms of samples with differing KOH concentrations. It is apparent that with increasing KOH concentration, the samples become less microporous.

small micropores and some mesoporosity; due to the sharp knee and gradual increase after 0.1 p/p_0, respectively. The 3:1 KOH ratio carbon shows cooperative micropore filling due to larger micropores and some mesoporosity; due to the soft knee and gradual increase after 0.1 p/p_0, respectively. The 4:1 KOH ratio carbons show cooperative micropore filling due to larger micropores and strong mesoporosity; due to soft knees and the large increase from 0.01 to 0.4 p/p_0, respectively. The isotherm analysis agrees well with the QSDFT results of the carbons, see figure 6.2.3. As the ratio of KOH to carbon precursor is increased, the pore sizes are seen to widen. The 2K type carbon has a large volume of small micropores and some mesoporosity. The 3K type carbon has less micropores at a larger width than the 2K as well as an increase in mesoporosity. The 4K type carbon has even less micropore volume and even more mesopores. One interesting point is that the small mesoporosity that the 2K carbon has for pores larger than 25 Å
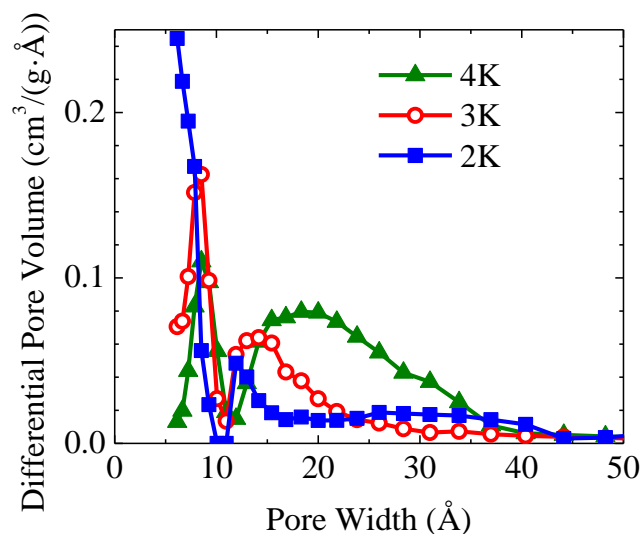
Figure 6.2.3. QSDFT PSD's for carbons of increasing KOH ratio. The micropore volume decreases and the mesopore volume increases. The larger mesopore "humps" and pore size shift to increasing pore widths is consistent with the idea of KOH pushing the pore walls apart.

seemingly disappears with the 3K. This can be explained if some pores that are increasing in width crush some of the larger mesopores. The results from this QSDFT analysis are consistent with the idea that the KOH activation pushes the pore walls apart.

The final pore characteristic of interest is the surface area for mass sample. The results show that there is a direct dependence of BET surface area on KOH concentration up to a ratio of 4:1, figure 6.2.4. The lack of confidence in the accuracy of applying the BET theory to the isotherms and the limited number of data points lessens the conclusion that this is a reliable conclusion. Further studies need to be done, perhaps using QSDFT areas, before concrete conclusions can be drawn about the KOH ratio effect on nominal surface area.

Further studies should be done to compare the effect of other activation parameters on the pore structure. Additionally, higher and more varied KOH ratios should also be tested.
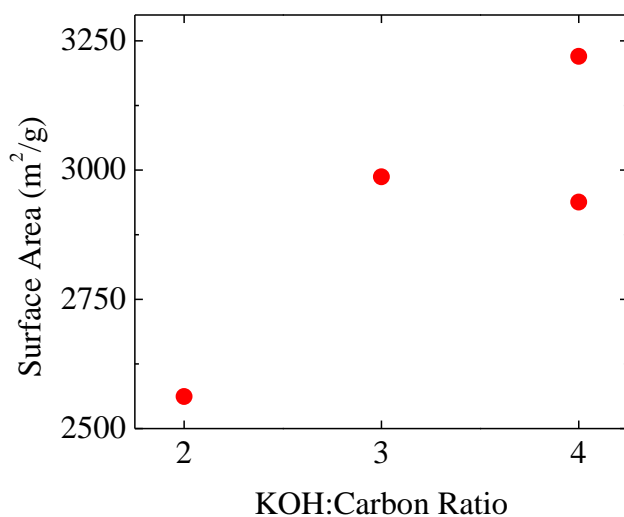
Figure 6.2.4. Nominal BET surface area dependence on KOH concentration.

6.3 Conclusion III: Pore Optimization for Gas Storage

The gas uptake should also depend directly upon the pore characteristics. As was discussed in section 3.1.3, there is an optimal pore width for methane and hydrogen uptakes. For methane at room temperature, it is assumed to be approximately 11 Å. This may be the same optimal pore width for hydrogen at 77 K. Figure 6.3.1 shows comparisons of the excess methane uptake with nanoporosity, porosity, nanopore volume for mass sample, and pore volume between 10 and 20 Å for mass sample. For these comparisons, the excess mass of methane for mass sample was chosen because it depends on the skeletal density. As a consequence, if there is a correlation between the excess mass adsorbed and a pore characteristic it means that it is a result of more pores with higher film density. As will be seen later in this section, a high excess mass adsorbed for mass sample will not necessarily relate to a high mass stored for mass sample or a high mass stored for volume of sample.

From these results, there is no apparent correlation between methane uptake and porosity or nanopore volume for mass sample. There is a strong direct correlation between the pore volume between 10 and 20 Å and the methane excess adsorbed. This is consistent with the theories that say a pore width of 11 Å leads to a higher methane uptake. The nanopore and 10 to 20 Å pore characteristics for these samples were determined using NLDFT, which may have an artifact at 10 Å. Therefore, this analysis should be redone using QSDFT as well.
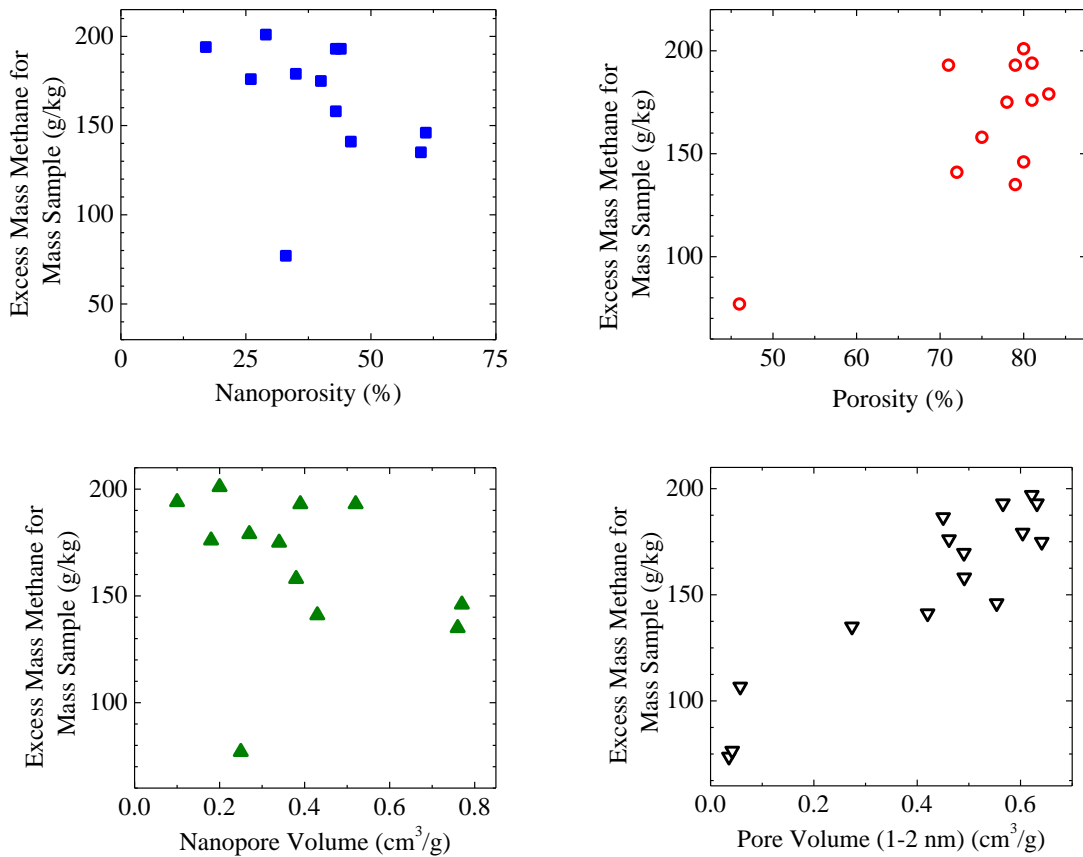
Figure 6.3.1. Excess mass adsorbed methane for mass sample compared with nanoporosity (top left) , porosity (top right), nanopore volume (bottom left), and pore volume between 10 and 20 Å (bottom right). The pore volume between 10 and 20 Å is the only one showing a reliable trend.
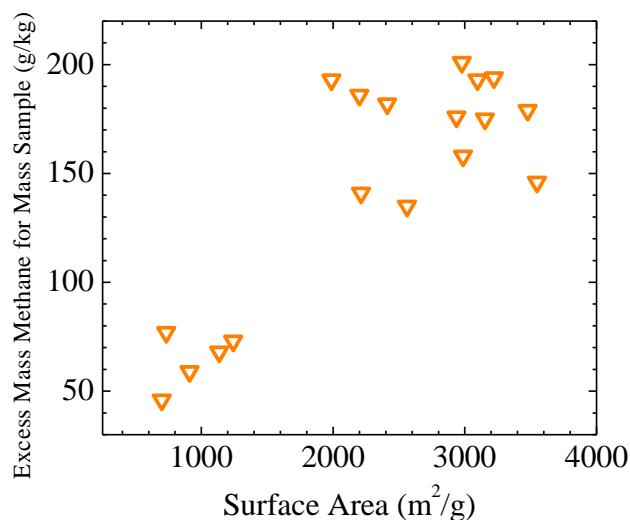
Figure 6.3.2. Excess mass adsorbed methane for mass sample compared with surface area.

There is also a strong correlation between nominal BET surface area and the methane uptake, see figure 6.3.2. As a corollary to the Chahine rule for hydrogen uptake (every 1000 m^2/g extra relates to an additional 10 g/kg hydrogen), it appears as though for every additional 1000 m^2/g surface area there is an increase of ~50 g/kg in the methane uptake at 35 bar and room temperature, (this holds true for amount stored as well, not shown in figure).

In conclusion I, it was proven that the ratio of KOH affects the pore structure. Consequently, there should be an optimum ratio of KOH that produces the optimum pore characteristics. Figure 6.3.3 shows comparison between the KOH uptake and the excess mass adsorbed, amount stored for mass and amount stored for volume. A ratio of 4:1 appears to have the highest excess methane uptake, this is consistent with assuming that this is also the ration which provides the highest percentage of pores between 10 and 20 Å. The values of more interest, however, are the amount stored for mass sample and the amount stored for volume sample. The direct dependence on porosity by the amount

stored for mass sample and the inverse dependence of mass stored for volume of sample on the porosity complicates the optimization process. The more important of the two characteristics is the mass stored for volume of sample, also called the storage density. As is shown in the figure 6.3.3, the mass stored for mass sample continues to increase with increasing KOH ratio. This is consistent with the decrease in apparent density caused by the higher KOH ratios. The storage density, however, has a maximum KOH ratio of 3:1. Accordingly, a 3:1 KOH ratio must lead to a high percentage of pores in the correct width range. Higher KOH ratios may have more pore volume in the proper width range, but they will also have more pore volume in larger pores that are not beneficial for methane storage. Analysis of carbon with higher KOH ratios and more varied KOH ratios is again needed to draw firm conclusions, however.
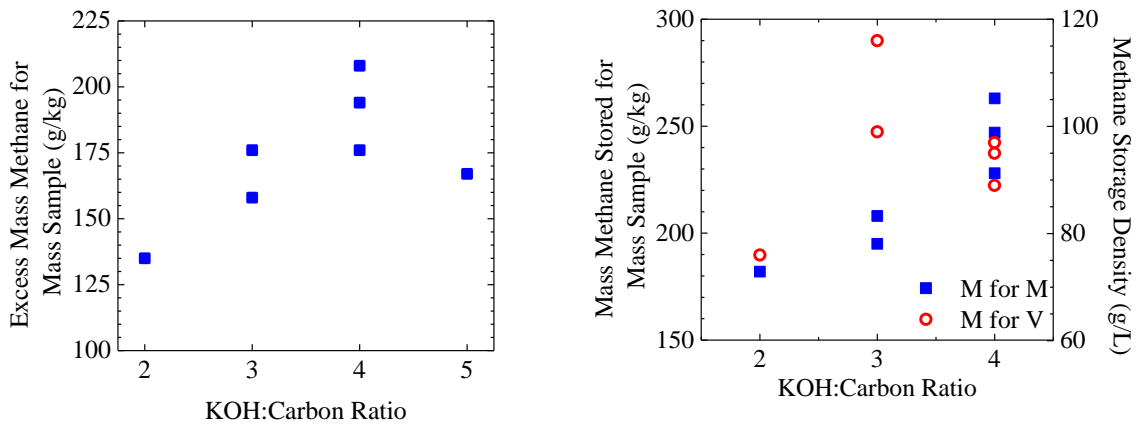
Figure 6.3.3. Left: Comparison of KOH ratio to excess mass methane for mass sample. Right: Comparison of KOH ratio and stored mass methane for mass sample and stored mass of methane for volume of sample.

6.4 Conclusion IV: Pore Optimization for Surface Area

A quantity which is of interest not only for gas storage, but also for other activated carbon uses is the surface area for mass sample, Σ. The smaller the pores, the more they will contribute to the surface area of the samples. Due to this nature of the surface area, the samples that have the largest nanoporosity, ϕ_{Nano}, should have the largest surface areas. Upon comparison of these pore characteristics with the nominal surface area, the results were not necessarily what was expected.
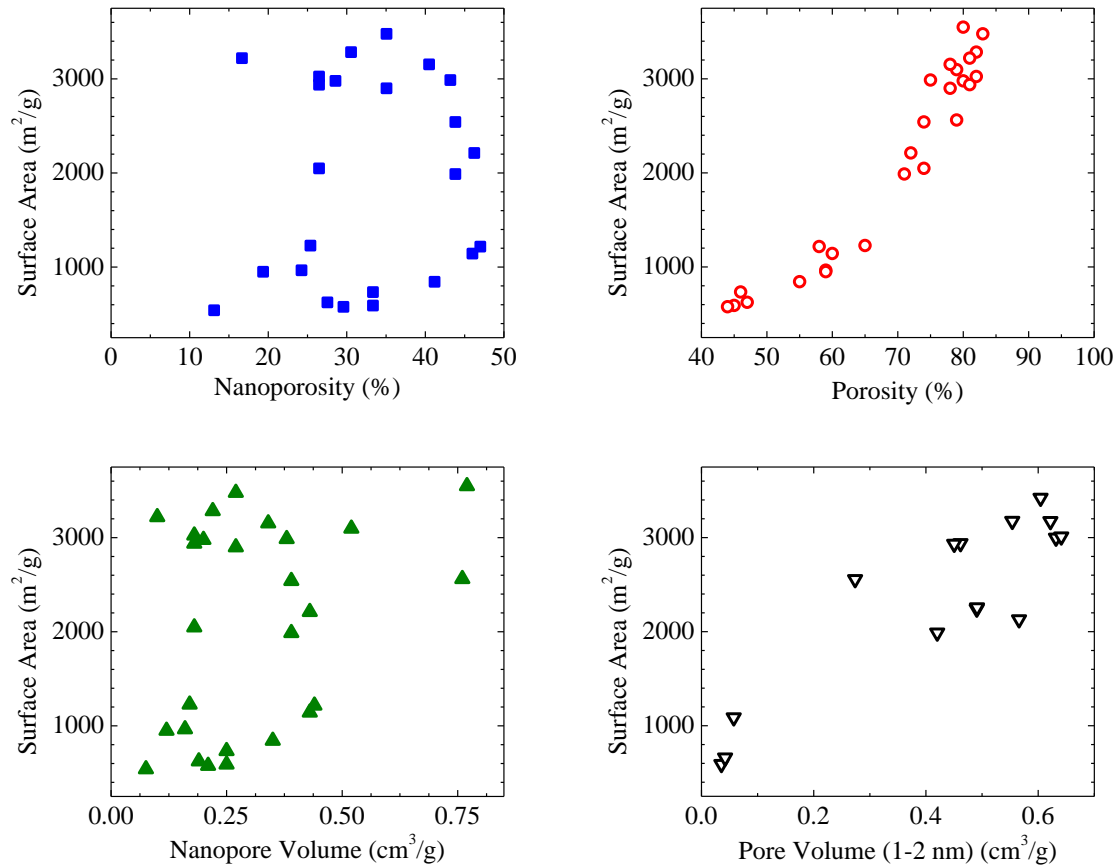
Figure 6.4.1. Surface area compared to nanoporosity (above left), porosity (above right), nanopore volume (below left) and pore volume between 1 and 2 nm (below right).

Figure 6.4.1 shows the results from comparing the nanoporosity, porosity, nanopore volume and pore volume between 10 and 20 Å to the nominal surface area. The nanoporosity and nanopore volume do not show any significant correlation to the surface area. This may be caused by the limitations of the two models used. The NLDFT model is known to have an artifact at 10 Å which may lead to an underestimate of the nanopore volume. The BET theory is designed for surfaces that can adsorb multiple layers of nitrogen, but nanopores can only fit one layer of nitrogen. The pore volume between 10 and 20 Å shows a linear correlation to the surface area. This is consistent with the limitations of the two models. It can be concluded that the hypothesis that a higher pore volume in smaller pores results in a higher surface area, within the limitations of the models applied. The surface area does seem to increase exponentially as the porosity approaches 100%. The more pores the sample has, the more surface area it can have. Further research needs to be done with other methods of surface area determination as well as QSDFT instead of NLDFT. One self-consistent approach would be to use QSDFT for both surface area determination and pore size distributions.

6.5 Conclusion V: Adsorption Physics

By applying the Langmuir model described in section 3.2, additional physics of adsorption of methane and hydrogen will be discovered. This further understanding of the physics behind the adsorption of these gases will lead to new ways of optimizing the samples. By comparison of experimental isotherms to theoretical generated isotherms, the adsorbed gas behavior, i.e. localized or mobile, will be determined for the cases of room temperature methane and hydrogen and 77 K hydrogen. Once this is known, the binding energies of the samples can be found by fitting (3.3) to the experimental

isotherms and then solving (3.4) and/or (3.5). Further, an experimental limit to the area per adsorbed molecule, $\alpha(T)$ can be found using inequality (3.8).

6.5.1 Hydrogen: Adsorption Equilibria

The two models of surface kinetics, localized and mobile, see section 3.2, were experimentally validated on sample S-33/k. Figure 6.5.1 shows excess adsorption isotherms calculated at 77 K and 298 K. . Excess adsorption drops with increasing pressure if the gas density increases more rapidly than the density of the adsorbed film (mobile adsorption at 77 K), and can turn negative (localized adsorption at 293 K) if the gas density exceeds the film density. The localized adsorption model at 77 K and the mobile adsorption model at 293 K, calculated with E_B = 5.3 kJ/mol (wide pores), agree qualitatively well with experimental data over a broad of pressures. However, the Langmuir calculation for 77 K falls below the experimental data for sample S-33/k at low
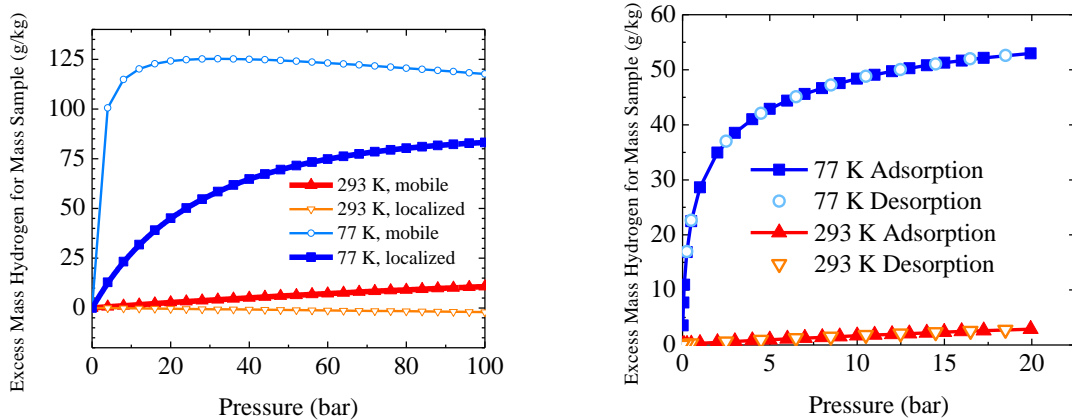
Figure 6.5.1. Left: Theoretical H2 excess adsorption isotherms computed from the Langmuir isotherm for localized and mobile adsorption in sample S-33/k. Localized and mobile adsorption at 77 K and 293 K, respectively (thick lines), are in good agreement with experimental data (right S-33/k). Localized and mobile adsorption at 293 K and 77 K, respectively (thin lines), are ruled out by the experimental data

95
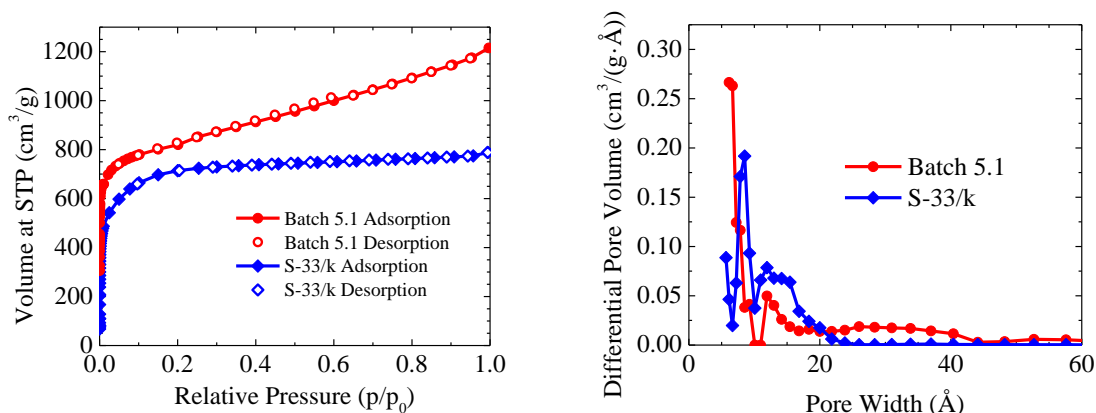
Figure 6.5.2. Left: Nitrogen sorption isotherms for S-33/k and Batch 5.1. Right: QSDFT PSD's for S-33/k and Batch 5.1.

pressures, consistent with the picture that sites with binding energies larger 5.0 kJ/mol, undoubtedly present in S-33/k, are occupied first and lead to higher coverage than what 5.0 kJ/mol entails, see also section 6.5.2. This agreement is remarkable in view of the experimental and theoretical input from widely different sources. Moreover, it allows experimental discrimination between two vastly opposed situations of how molecules do or do not move along the surface. For these samples, 77 K is localized and 293 K is mobile. All further analysis of the hydrogen isotherms will assume that the hydrogen is localized near cryogenic temperatures and is mobile near room temperature. In future research, a more inclusive approach should be used which allows for a progression between the two models.

6.5.2 Hydrogen: Binding Energies

Now that the surface kinetics are differentiated between mobile and localized adsorption, the binding energies at the cryogenic and room temperatures can be determined. A case study was performed on sample S-33/k and Batch 5.1. Figure 6.5.2

compares the nitrogen isotherms and the QSDFT pore size distributions of the two samples.

Figure 6.5.3 shows experimental absolute hydrogen sorption isotherms for samples S-33/k (left) and Batch 5.1 (right). The top row shows the best fit by a single Langmuir adsorption isotherm ((3.3), with a single binding energy). The bottom row shows a two binding energy fit:

$$\frac{M_{\text{Ads}}(p,T)}{M_{\text{S}}} = \frac{M_{\text{Mono}}}{M_{\text{S}}}\left[(1-f_{\text{high}})\theta(p,E_{\text{B,low}}) + f_{\text{high}}\theta(p,E_{\text{B,high}})\right], \qquad (6.1)$$

where θ is coverage, from which the low and high binding energy, $E_{\text{B,low}}$ and $E_{\text{B,high}}$, and fraction of high-energy sites, f_{high}. The binding energies from the fits are collected in table 6.5.1. The room-temperature isotherms are so close to linear that they allow only for a low-pressure, high-binding-energy fit. The distinct values for $E_{\text{B,high}}$ and $E_{\text{B,low}}$ from the isotherms at cryogenic temperatures are remarkably similar in the two samples, considering how different the isotherms of the two samples look. The steep rise of Batch 5.1 at low pressure might suggest that $E_{\text{B,high}}$ for Batch 5.1 is considerably larger than for S-33/k. But table 6.5.1 shows that this is not so; instead the two samples have very similar high binding energies and a similar number of high-energy binding sites per mass of sample. The values for $E_{\text{B,high}}$ in table 6.5.1 from the cryogenic isotherms agree very well with the prediction obtained via molecular
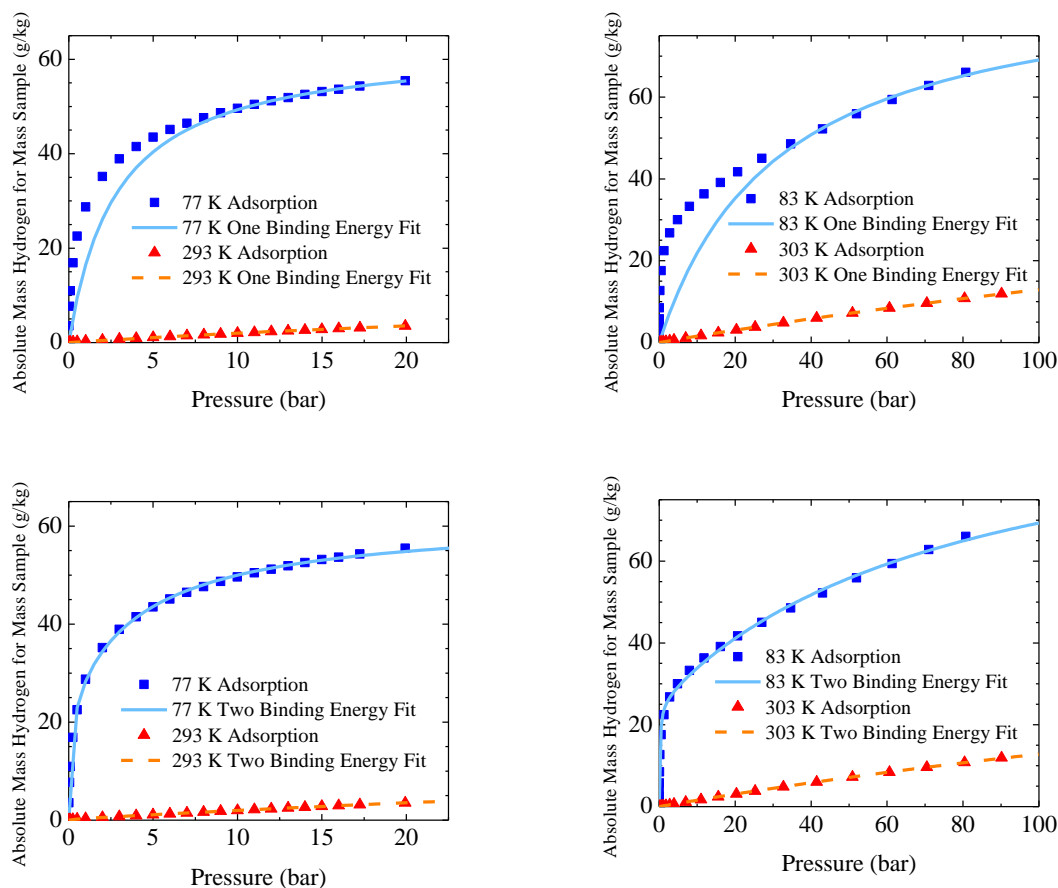
Figure 6.5.3. Absolute hydrogen adsorption for sample S-33k (left) and Batch 5.1 (right). The surface areas were 2600 m²/g and 3200 m²/g, respectively; the nanopore volumes (pores of width ≤10 Å) were 0.39 cm³/g and 0.76 cm³/g. Points are experimental, lines represent single-energy fits (top) and two-binding energy fits (bottom)

simulations. The values for $E_{B,low}$ are somewhat on the high side compared to the prediction, which may be explained in terms of variations expected in the presence of surface defects and impurity atoms, which our samples may carry.

The low binding energy is consistent with the ~5.0 kJ/mol assumed for a single graphite surface. The high binding energies are consistent with narrow pores having

Table 6.5.1. Low and high binding energies and respective fractions of sites for S-33/k and Batch 5.1. The fraction of high-energy sites, ~25-40%, is consistent with that a large fraction of the pore space resides in pores of width ≤10 Å.

	Low binding energy	Fraction of low-energy sites	High binding energy	Fraction of high-energy sites
S-33/k (77 K)	6.4 kJ/mol	61%	8.6 kJ/mol	39%
Batch 5.1 (83 K)	4.8 kJ/mol	75%	9.0 kJ/mol	25%

largely overlapping surface potentials which can lead to almost twice the binding energy, ~10 kJ/mol. If we assume that the higher binding sites come from pores less than ~6 Å, then the fraction of high binding sites is consistent with the QSDFT results of the two samples. S-33/k has approximately 22% of its pore volume and Batch 5.1 has approximately 44% of its pore volume in smaller than 6 Å.

6.5.3 Hydrogen: Experimental Verification of Cross-sectional Adsorption Areas

The cross-sectional area for adsorption site was determined from molecular simulations by Wexler, Cepel et al. The cross-sectional area inequality, derived in 3.2, can be expanded with the knowledge that the excess adsorption must always be smaller than the absolute adsorption. Equation (3.8) then becomes

$$\alpha(T) < M_{H_2} \Sigma \cdot \frac{M_S}{M_{Ads}^{Ex}(p,T)}.$$

(6.2)

Applying this inequality with the highest pressure uptake values will give us the lowest cross-sectional area inequality. Comparison of theoretical and experimental values is given in table 6.5.2.

Table 6.5.2. Values of $\alpha(T)$ from computer simulations, and experimental upper bounds

T	$\alpha(T)$	$M_{H_2} \Sigma \cdot \dfrac{M_S}{M_{Ads}^{Ex}(p,T)}$ Batch 5.1, 50 bar
77 K	6.4 Å^2	13.4 Å^2
293 K	11.2 Å^2	148 Å^2

6.5.4 Hydrogen: Sorption Kinetics

The adsorption and desorption kinetics have been determined for hydrogen in carbon nanopores [56]. The rates of adsorption and desorption were determined using the kinetic theory of gases. The molecules are assumed to be in the collisionless regime where the mean free path of the hydrogen is much larger than the width of the pore. The rate of sorption is given as the change in coverage per time. For desorption, the rate of change is calculated as if the surface had 100% coverage and was then exposed to vacuum. This gives the rate of change of desorption as,

$$\frac{d\theta_{des}}{dt} = \frac{\theta_{des}}{t_{des}} \tag{6.3}$$

where t_{des} is the characteristic desorption time. The desorption coverage is given simply as,

$$\theta_{des}(t) = e^{-t/t_{des}} . \tag{6.4}$$

The rate of change of adsorption is calculated assuming that the surface has 0% coverage and is shown a specific pressure, p, of adsorptive of gas of molecular mass, m, at temperature T. From the kinetic theory of gases, the number of collisions of gas molecules with the surface is given by

$$\frac{p}{\sqrt{2\pi mkT}} \tag{6.5}$$

where k is the Boltzmann constant [57]. From this, the rate of adsorption and the adsorption coverage are calculated as

$$\frac{d\theta_{ads}}{dt} = \frac{(1-\theta_{ads})}{t_{ads}} = \frac{p}{\sqrt{2\pi mkT}}(1-\theta_{ads})\alpha(T) \tag{6.6}$$

$$\theta_{ads}(t) = 1 - e^{-t/t_{ads}}$$

t_{ads} is the characteristic time of adsorption. Assuming that at equilibrium the adsorption and desorption coverage and rates are equal, the characteristic times can be determined.

$$t_{ads} = \frac{\sqrt{2\pi mkT}}{p\alpha(T)}$$

(6.7)

$$t_{des} = \begin{cases} \dfrac{kT}{2\pi m\alpha(T)v_x v_y v_z} e^{E_B/(N_A kT)} & \text{localized; high } T \\ \dfrac{1}{v_z} e^{E_B/(N_A kT)} & \text{mobile; high } T \end{cases}$$

The parameters are the same as given in equations (3.4) and (3.5). Assuming that the adsorbate is localized at 77 K and mobile at room temperature, the characteristic times of adsorption and desorption are given in table 6.5.3. It is interesting that the adsorption times do not depend on the binding energy of the sample or on whether it is localized or mobile sorption.

Table 6.5.3. Characteristic times of adsorption and desorption at 77 K and room temperature for different binding energies.

Binding Energy	5.0 kJ/mol	14 kJ/mol	30 kJ/mol
		77 K	
Characteristic adsorption time	1.5×10^{-11} s	1.5×10^{-11} s	1.5×10^{-11} s
Characteristic desorption time	2.0×10^{-11} s	2.8×10^{-5} s	2.1×10^{6} s
		293 K	
Characteristic adsorption time	1.6×10^{-11} s	1.6×10^{-11} s	1.6×10^{-11} s
Characteristic desorption time	2.1×10^{-12} s	8.5×10^{-11} s	6.2×10^{-8} s

The values chosen for the binding energies are as follows: 5 kJ/mol is the binding energy of hydrogen on a graphite surface; 14 kJ/mol is the optimum binding energy for hydrogen storage as found in [8]; 30 kJ/mol is the maximum assumed binding energy for boron and hydrogen, it also acts as a binding energy that is high for physisorption, but not quite chemisorption.

From these times, it is obvious that in sorption experiments, the adsorption/desorption of the hydrogen molecules is not the time limiting step. The only time that would become an issue is the 30 kJ/mol at 77 K which results in a desorption time on the order of months. Yet, if the sample is simply heated to room temperature the time is back to being negligible.

6.6 General Conclusions

This project successfully answered the questions presented in section 1.2. Additionally, it has been determined that the activated carbon produced from waste corncob have very interesting characteristics. Some of these characteristics include, but are not limited to:

- Non-prohibitive cost,

- High mass of gas stored for mass of material,

- High mass of gas stored for volume of material,

- Reversibility,

- Durability,

- Fast gas kinetics.

The materials have shown record storage for methane in activated carbons, and show promise for hydrogen storage. Further research is currently taking place on these materials to improve the characteristics outlined above and to explore other uses for the materials, super-capacitors for example.

Chapter 7: Future Research and Recommendations

7.1 New Projects

There are two new projects that are being explored currently for improving the hydrogen storage ability of the carbons: elemental doping of boron and production of higher surface areas with the use of fission tracks.

7.1.1 Boron-doping

To meet the DOE's hydrogen storage goals, the hydrogen-carbon binding energy on nonporous carbon, ~5 kJ/mol, must be improved [8]. Significantly higher storage can be achieved in porous carbons by surface functionalization: (i) via creation of nanometer-sized pores which dramatically raise the surface area for adsorption (>3,000 m^2/g) and create deeper potential wells (almost doubling the adsorption energy) [9]; and/or (ii) by doping with elements capable of strengthening the hydrogen-substrate interaction (boron, iron, titanium and others) [58-61].

Work currently being done by ALL-CRAFT has explored the use of boron-doping to increase hydrogen storage. The doping of boron into the carbon is being pursued using three different methods.

The first method is the use of decaborane ($B_{10}H_{14}$). Decaborane is a novel compound and will be doped into the carbon through vapor or liquid phase deposition. The second method is copolymerization of boron containing monomers with monomers used to make high quality activated carbons, such as vinylidene chloride. The last

method is the introduction of other boron containing compounds at some stage of the activation process.

7.1.2 Fission Tracks

Another project being explored is the use of fission tracks to produce higher surface area carbons. Boron-doped carbons are exposed to high energy neutrons. When a neutron collides with a boron atom an alpha particle and a lithium atom are produced,

$$^{10}B + {}^{1}n \rightarrow \left[{}^{11}B \right] \rightarrow {}^{7}Li + {}^{4}He. \tag{7.1}$$
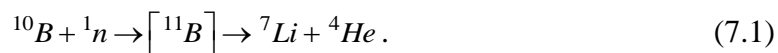
The lithium and alpha particle cause damage to the carbon matrix as fission tracks. The carbon atoms are then removed via etching. This is theorized to increase the surface area of the carbons from 3,000 to 5,000 m^2/g.

7.2 New Instrumentation

7.2.1. Manometric Supercritical Hydrogen Sorption Apparatus

A new room temperature manometric supercritical hydrogen sorption apparatus is currently being built by the Midwest Research Institute in collaboration with ALL-CRAFT. The new instrument will perform hydrogen uptake analysis on boron-doped briquettes up to 250 bar. The instrument is a reservoir type manometric instrument along the lines of the methane test fixture. Figure 7.2.1 shows a picture of the instrument. The finished apparatus will be largely automated with LabVIEW. Additionally, the briquettes will be transferred into the sample chamber under nitrogen atmosphere. If the project proves successful, a cryogenic sample chamber may be designed and built.

Figure 7.2.1. New room temperature manometric supercritical hydrogen sorption apparatus.

7.2.2. Manometric Supercritical Methane Sorption Apparatus

As part of renewed interest in the storage of methane gas, a new manometric supercritical methane sorption apparatus will be built. The new apparatus will be similar to the current methane test fixture. However, the new instrument will be completely automated and will have the ability to attain pressures up to 250 bar.

7.2.3 Advanced Outgassing Apparatus

Future research may benefit from the design and manufacture of an advanced outgassing apparatus. The new apparatus should be automated with LabVIEW and follow the controlled rate thermal analysis method [33]. This method is designed to prevent damage to the porous structure and to prevent elutriation of the powder. A turbo-molecular pump should be used to reach higher vacuum. Another recommendation for the apparatus would be the inclusion of a mass spectrometer. This will allow the identification of which chemical species are coming off the samples during outgassing.

7.3 Alternative Experimental Methods

Further research using the current methods should also be pursued. Recommendations for alternative methods of analysis as well as optimization of each set-up are presented in this section.

7.3.1 Manometric Subcritical Nitrogen Sorption

Future research may benefit from the purchase of a new six station Autosorb. The new instrument could focus on determining surface areas and porosity quickly for each sample as part of the rapid-screening process. The current Autosorb 1-C could then concentrate on more detailed nitrogen isotherms. Additionally, the Autosorb 1-C could be used to perform low-pressure, 77 K hydrogen sorption isotherms. Furthermore, the use of argon at liquid argon temperatures could be explored. Further analysis of the isotherms already produced should include reanalyzing all NLDFT with QSDFT as well as exploring alternative methods of isotherm analysis.

7.3.2 Manometric Supercritical Hydrogen Sorption: Rapid-screening Hydrogen Sorption Instrument

The RHS needs to be optimized so as to reduce leaks as well as to expedite the data collection process. This instrument holds great potential to acquire data necessary for decision making processes very quickly.

7.3.3 Manometric Supercritical Hydrogen Sorption: Hiden Isochema HTP1-V Mark II

One of the quantities that needs to be determined in order to perform reliable gas adsorption measurement is the skeletal volume and therefore skeletal density of the sample. The general way these values are found is with helium pycnometry. Unfortunately, the activated carbon samples are too good at gas adsorption and have been

found to adsorb helium at room temperature. This is a problem well-documented for some activated carbons. The way to get around this issue is to raise the temperature of the carbon and helium which will reduce the density of gas and the adsorption effects. With the new HTP instrument, we can perform high-temperature pycnometry up to 500 °C, which should eliminate this issue.

Furthermore, hydrogen isotherms need to be performed at different cryogenic temperatures so that the isosteric differential enthalpy of adsorption can be determined. This is most widely used method to determine the binding energy and will act as a good comparison to the binding energies determined via Langmuir theory of gas sorption.

Future research may benefit from the purchase of additional pressure transducers to increase the pressure range at which reliable hydrogen isotherms can be taken. Additionally, the glove box attachment for the instrument can reduce the sample exposure to air.

7.3.4 Manometric Supercritical Methane Sorption

The methane test fixture has been modified so as to reduce or eliminate leaks. The time for measurement of individual data points can possibly be reduced with further investigations. The isotherms produced can be analyzed with NLDFT to attain the pore size distributions of the samples.

7.3.5 Gravimetric Supercritical Methane Sorption

The 250 bar methane gravimetric apparatus has broadened the capabilities of methane sorption physics analysis. Additional methane isotherms should be performed on both the 35 bar and 250 bar apparatus. The 35 bar isotherms can be analyzed with NLDFT to get pore size distributions. The decrease in the excess adsorption seen in the

250 bar isotherms can be analyzed to determine not only more methane sorption physics, but allows for a different method of surface area determination [62].

Appendix A: Determination of Porosity

The porosity, ϕ, of a sample is given by:

$$Porosity = \frac{Total\ Open\ Pore\ Volume}{Apparent\ Particle\ Volume} = \frac{V_{TotalPore}}{V_{Apparent}} \tag{A.1}$$

The effective volume includes the skeletal volume of the carbon as well as the total pore volume.

$$V_{Apparent} = V_{TotalPore} + V_{Skeletal} \tag{A.2}$$

Substituting (A.2) into (A.1) gives

$$\phi = \frac{V_{TotalPore}}{V_{TotalPore} + V_{Skeletal}} \tag{A.3}$$

Experimentally we are only able to find the total pore volume per mass of sample, so dividing top and bottom with the sample mass, M_S gives

$$\phi = \frac{\dfrac{V_{TotalPore}}{M_S}}{\dfrac{V_{TotalPore}}{M_S} + \dfrac{V_{Skeletal}}{M_S}} \tag{A.4}$$

T he skeletal density of carbon is given by

$$\rho_{Skeletal} = \frac{M_S}{V_{Skeletal}} \tag{A.5}$$

So (A.4) becomes

$$\phi = \frac{\dfrac{V_{TotalPore}}{M_S}}{\dfrac{V_{TotalPore}}{M_S} + \rho_{Skeletal}^{-1}} \tag{A.6}$$

Simplifying (A.6)

$$\phi = \left[1 + \left(\rho_{Skeletal} \cdot \frac{V_{TotalPore}}{M_S} \right)^{-1} \right]^{-1} \qquad (A.7)$$

Appendix B: Gravimetric Methane Procedure

We use gravimetric measurements to calculate the methane uptake onto our activated carbons. Through the measurement of four masses throughout the procedure, we can calculate the absolute adsorption, the excess adsorption and the amount of stored methane

> **Important Note: Throughout the procedure, care must be taken not to damage any of the equipment and safety is a primary concern. To this end:**
> 1) The valve on the Sample Cell must never be opened with more than a 25 psi pressure differential across it.
> 2) The pressure transducer should never see more than a 25 psi jump in pressure.
> 3) Care must be taken with the balance so as not to damage it, never put more than 500 grams on the balance or anything not at room temperature.
> 4) When an experiment is completed or a stopping point is reached, the valve on the gas cylinder must be closed.

in the sample. A sample lab book page is at the end.

Part 1. How to Use the Balance

1) The uncertainty in the balance is about ±0.002 g

2) Make sure the balance display reads 0.000 g

   - If it isn't then press the tare button

3) Place the Sample Cell on the balance as shown

4) Wait at least 10 seconds to make sure the reading has settled before writing down measurement

5) All mass measurements are to be taken a minimum of five times after being tared or until three measurements are the same, whichever is greater

6) If the balance does not return to 0.000 g, then tare and make note of it in your lab book

   - These rarely happens, wait at least 30 seconds before taring

Part 2. Single Pressure Measurements

Latex gloves are to be worn anytime the Sample Cell is handled. If anything is on the Sample Cell (i.e. dust from oven) please wipe-off with a Kim-wipe®.

1) Please record the following at the top of the page in your lab book

   - Date
   - Time
   - Sample Name
   - Temperature
   - Humidity
   - Pressure

2) Here are some of the tools that you will use

   - Mortar & Pestle
   - Sample Bottles
   - Box Cutter
   - Allen Wrenches
   - Bolts
   - Latex Gloves
   - Glass Wool Removal Tool
   - Exacto® Knife
   - Screwdriver
   - Dissecting Needle
   - Spatula

- Tweezers
- Needle-nose Pliers

3) Turn on oven so it can be warming

   up

4) Make sure the fan switch on the back

   is on

5) The Sample Cell is made up of two pieces with a copper gasket in between, held

   together with socket (allen) head bolts

   - Sample cell parts from left to right

     - VCO-fitting
     - Valve
     - Conflat flange
     - Sample Cylinder

6) Place the Sample Cell in the high pressure set-up's aluminum Sample Cell Holder

7) Tighten at least the two diagonal socket (allen) head bolts using the 3/16" allen

   wrench

8) Cut-off about 4-6 inches (10-15 cm, ~width of hand) of glass wool using scissors

   - **<u>Wear latex gloves whenever handling glass wool</u>**

- **Glass wool can cause skin irritation**

9) Tear this in half length-wise

- If it frays too much then roll it in your hands

10) Put the glass wool in the Sample Cell using a twisting/pushing motion

- If done right this also makes it easier to get it out later

11) Place a new copper gasket in its seat in the conflat flange

- Place the flat side of the gasket down

12) Place the valve portion of the Sample Cell on top of the gasket making sure it is seated properly

13) Place the socket head bolts into the holes, coming from the valve side

- Use bolts from Used Bolt drawer first, inspect for damage to threads or socket head

14) Tighten them by hand until they are flush with the top of the flange

- The bolt should easily tighten by hand until it is flush
- If it does not, then gently loosen it and retighten
- If it is still not easy to tighten it until by hand until flush, gently loosen and remove the bolt, discard that bolt and use another one.

15) If the socket gets damaged in any way, then discard and use a different one.

16) If there is any doubt as to the integrity of the bolt, discard it. This is the only part of the procedure when this can be done. If there are any bolt-issues later on, the experiment has to be restarted. [Note: A bolt costs on the order of cents, the Sample Cell costs on the order of hundreds of dollars]

17) Tighten the bolts the rest of the way using the 9/64" allen wrench. Tighten the bolts in clockwise order. Make sure to stop at about the same torque for each bolt

as you go around. The wrench should traverse about a sixth of a turn (same as

angle between 12 and 2 on a watch). This should take at least 3-4 cycles on

tightening. The bolts should be tight, but if the bolt "skips," then the bolt is too

tight.

18) Make sure there is a polymeric o-ring on the vco-fitting. This o-ring must be

replaced every 4-5 full experiments. The o-ring can be removed using the

dissecting needle.

Male vco-fitting
showing polymeric
o-ring

[Important Note: Since the final calculations are based on mass differences of the

four measured masses, the same polymeric o-ring, copper gasket, glass wool, and

bolts have to be used the whole experiment]

19) Weigh the Sample Cell per instructions above, record in the lab manual as "M_C

(pre-outgas)"

20) Slide the long end of the Sample Cell into the top hole on the oven.

21) Open the Sample Cell Valve, by turning the green knob counter-clockwise. There is a tension change in the valve when it is fully open. The valve should be opened until just before this tension change. If the valve is opened past this point retighten until slightly before this point. Turning the knob

22) Attach the vacuum hose to the Sample Cell, first tighten by hand and then tighten with the 5/8" and 11/16" line wrenches.

23) Wait until the clock is showing the minute change and then flip the switch on the vacuum pump and record the time in your lab manual.

24) This outgassing should be done for half an hour.

25) When the half hour is up (watch the clock to be exact, and make sure you record the time) close the green valve on the Sample Cell, then turn off the vacuum pump.

Gas Line-Side Regulator Gauge

Cylinder-Side Regulator Gauge

Wall Gauge

Gas Cylinder Valve

Pressure Regulator Knob

Wall Gauge

Transducer Panel Meter

Pressure Transducer

Sample Cell Valve

Bleeder Valve

Main Line valve
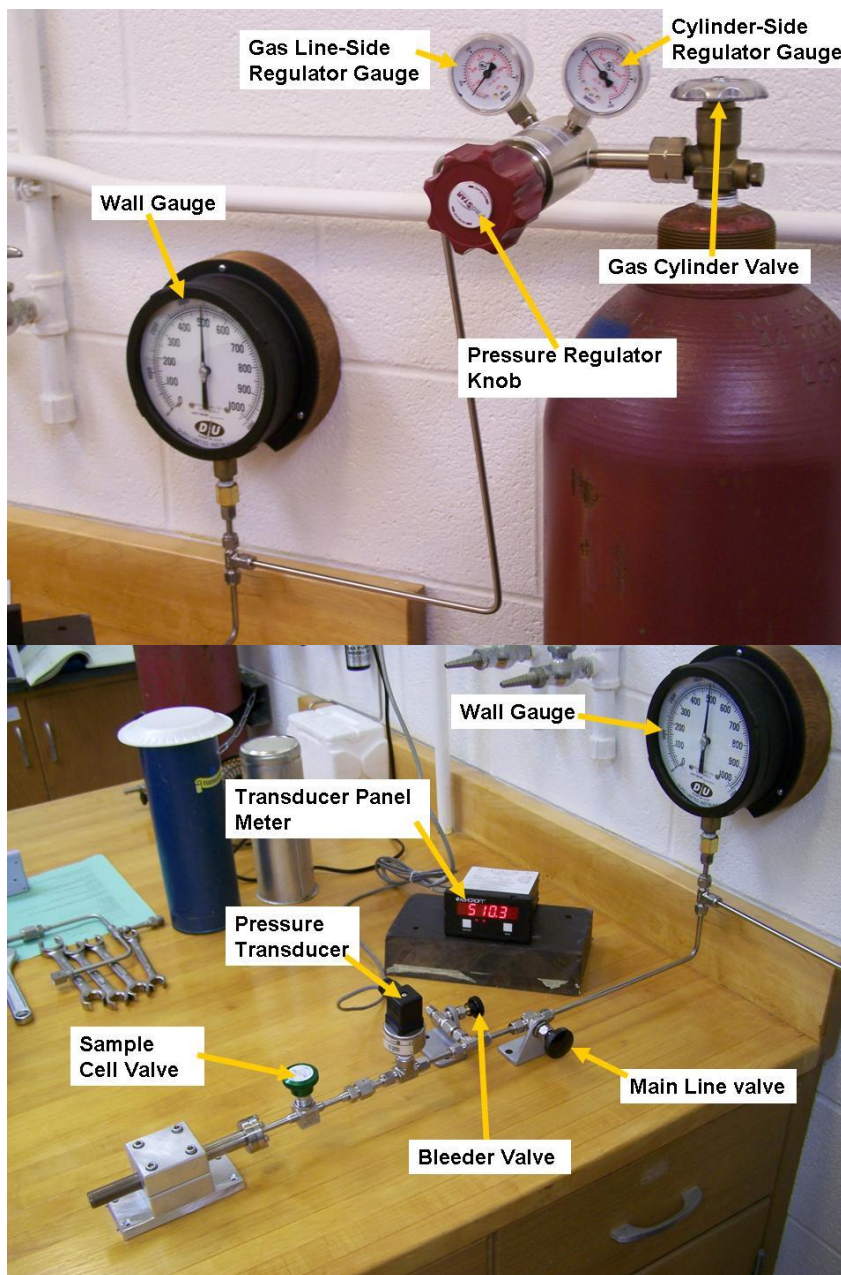
26) Use the line wrenches to first loosen the nut on the vco-fitting and then loosen the rest of the way by hand. When you remove the hose, you should hear a short hiss of air going into the hose.

27) Put on the high temperature oven gloves and remove the Sample Cell from the oven. Place the Sample Cell in either of the Sample Cell Holders and put the small desk fan blowing on it. It usually takes about ten to fifteen minutes for the Sample Cell to cool.

28) Weigh the Sample Cell (make sure it is at room temperature) and record the weight as "M_C". This is the value that will be put into the excel spreadsheet.

29) The second mass measurement is the mass of the Sample Cell with methane (no carbon).

30) Put the Sample Cell in the methane holder and tighten down at least the two diagonal socket bolts on the holder with the 3/16" allen wrench.

31) Attach the Sample Cell to the methane set-up. Use the 5/8" and 11/16" line wrenches to tighten the Sample Cell.

32) The procedure for using the methane set-up needs to be followed carefully, and extreme care needs to be taken not to allow more then a 25 psi pressure difference on the transducer or on either side of the Sample Cell valve when it is opened.

33) Usually the single pressure values taken are 500 or 25 psig, unless otherwise informed.

34) Before letting methane into the Sample Cell the line needs to be bled to remove any air in it.

35) Begin by making sure all the valves and the regulator are closed. Valves are closed by turning the knob clockwise (cw), but the regulator is the opposite, make sure it is turned all the way counter-clockwise (ccw).

36) First open the Gas Cylinder Valve on top of the cylinder (ccw), there should be a "thunk" sound and the Cylinder-Side Regulator Gauge should show a pressure of ~1000 psig.

37) Now open the Main Line Valve (ccw) one full turn.

38) Open the Pressure Regulator (cw) slowly until the Transducer Panel Meter shows ~15 psig.

39) Now open and shut the Bleeder Valve 10 times (ccw then cw) about a quarter of a turn.

40) The line is now bled.

41) Now open the Sample Cell Valve

42) Slowly increase the pressure using the Pressure Regulator Knob (cw).

43) The pressure read-out on the Transducer Panel Meter shouldn't change by more than 20 psig each time it refreshes.

44) Increase the pressure to the value desired.

45) The pressure should be within 1 psig of the desired value (i.e. 500 ± 1 psig)

46) If you overshoot the desired pressure, back the regulator off a little (ccw) and then use the Bleeder Valve to bring the pressure back down and use the regulator again to bring the pressure back up.

47) Record the time that the Sample Cell Valve was opened (5.6) in your lab book.

48) Record the initial pressure from the Transducer Panel Meter in your lab book.

49) Close the Sample Cell Valve tightly after 30 minutes. Record the time that you closed the valve and the final pressure before you closed the valve.

50) Fully close the Pressure Regulator (ccw).

51) Open the Bleeder Valve one-eighth of a turn and allow the pressure to return to ~ 1 psig. Then close the Bleeder Valve.

52) Close the Main Line Valve.

53) Remove the Sample Cell using the line wrenches to first loosen the female vco-fitting.

54) Weigh the Sample Cell per Part 1 Section 2. Record the mass as "$M_{C,M}$".

55) Reattach the Sample Cell to the methane set-up and tighten with the line wrenches.

56) Bring the pressure back up to ~500 psig.

57) There is no need to bleed the line this time.

58) Open the Main Line Valve and bring the pressure up to 500 ± 5 psig slowly (again at most a 20 psig jump every refresh) using the Pressure Regulator.

59) Open the Sample Cell Valve.

60) Close the Gas Cylinder Valve.

61) Open the Bleeder Valve one-eighth turn. Allow the pressure to return to ~1 psig.

62) Close the Bleeder Valve, Main Line Valve and Pressure Regulator.

63) Remove the Sample Cell from the set-up.

64) The nest three mass measurements are pretty much done the same way as above except with a sample (carbon) in the Sample Cell.

65) Carefully take the Sample Cell apart. It is again useful to have the Sample Cell in the hydrogen set-up's Sample Cell Holder.

66) Remove the glass wool from the Sample Cell using the large tweezers.

67) If the glass wool starts to tear, use the glass wool removing tool to remove it.

68) Insert the copper end of the tool into the glass wool and gently push down and turn clockwise a few turns.

69) Gently pull the tool out and remove the glass wool.

70) Place the sample into the Sample Cell, with powder samples; use the small, white funnel.

71) Place the glass wool back into the Sample Cell. (4.2)

72) Put the Sample Cell back together. (4.5-4.6)

73) Weigh the Sample Cell and record in lab book as "$M_{C,S}$ (pre-outgas)"

74) Outgas the sample using steps 4.9-4.16. Only this time outgas the cell without it in the oven for 10 minutes followed by outgassing in the oven for 2 hours.

75) Weigh the Sample Cell and record as "$M_{C,S}$"

76) Take the next measurement with methane, follow instructions 5.1-5.14.

77) Weigh the Sample Cell and record as "$M_{C,S,M}$"

78) Let the methane out per 5.16-5.22

79) Make sure that all valves and the regulator are shut and that there are no sections of line under pressure. Shut off the oven and the fan on its back.

80) Take the Sample Cell apart and remove and discard the glass wool. The copper gasket goes into the recyclable copper drawer. The polymeric o-ring needs to be left in its seat for at least 4-5 full experiments. Return the sample to its container and place in the sample drawer.

Appendix C Processing of Gravimetric Data

Measure the following four masses:

m_C : Mass of evacuated chamber.

Vacuum
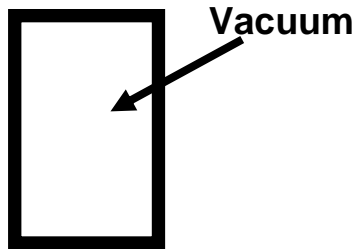
$m_{C,M}$: Mass of chamber and methane.
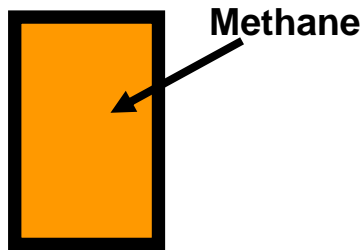
Methane

$m_{C,S}$: Mass of chamber and outgassed sample.

Vacuum
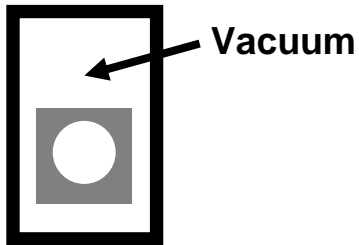
$m_{C,S,M}$: Mass of chamber, sample, and methane.

Methane
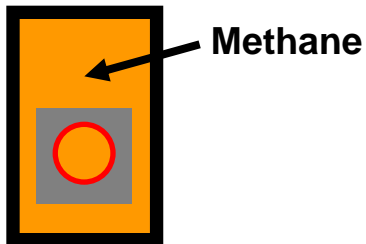
In addition, assume as known:

ρ_S : Skeletal density of sample (no pores included).

- Value for amorphous carbon is $2 \, {}^{g}\!/_{cm^3}$.

- Value for calixerine (p-tert-butyl-calix[4]arene) is $1.0265 \, {}^{g}\!/_{cm^3}$.

ρ_P : Piece density of sample (all pores included).

- Values taken from table or use $0.500 \, {}^{g}\!/_{cm^3}$ to be a good estimate.

ρ_{CH_4} : Density of methane at measured pressure.

- Value at 500 psi is $0.024074 \, {}^{g}\!/_{cm^3}$.

- Value at 25 psi is $0.0011338 \, {}^{g}\!/_{cm^3}$.

ρ_{ads} : Density of adsorbed film.

- Value from Monte Carlo simulations $0.17 \, {}^{g}\!/_{cm^3}$.

$V_{Nanopore}$: Volume of nanopores.

- Taken to be volume of pores < 20 Angstroms in diameter.

- Values gotten from DFT analysis of nitrogen isotherm.

Find:

V_S : Skeletal volume of sample (no pores included).

V_P : Piece volume of sample (all pores included).

V_{ads} : Volume of adsorbed film.

m_{ads} : Mass of adsorbed CH_4.

m_{ads}/m_S : Mass of adsorbed CH_4 per mass of sample.

m_{ads}^e : Excess adsorption defined to be the difference between the mass of the adsorbed

film and the mass of an equal volume of non-adsorbed gas.

m_{ST} : Mass of methane stored in sample, in both adsorbed and non-adsorbed phases.

m_{ST}/m_S : Mass of methane stored per mass of sample.

ρ_{ST} : Volumetric methane storage density, mass of methane stored per volume of

sample.

Solution:

$$V_S = \frac{\left(m_{C,S} - m_C\right)}{\rho_S} \tag{C.1}$$

$$V_P = V_{All\ Pores} + V_S = \frac{\left(m_{C,S} - m_C\right)}{\rho_P} \tag{C.2}$$

$$V_{ads} = \frac{m_{ads}}{\rho_{ads}} \tag{C.3}$$

$$\begin{aligned} m_{ads} = m\left(chamber + sample + CH_4\right) - m\left(chamber + sample\right) - \\ m\left("supernatant"\ CH_4\right) \end{aligned} \tag{C.4}$$

$$m\left(chamber + sample + CH_4\right) = m_{C,S,M} \tag{C.5}$$

$$m(chamber + sample) = m_{C,S} \tag{C.6}$$

$$
\begin{aligned}
m\left("\text{supernatant}"CH_4\right) &= m\left(CH_4 \text{ in chamber in absence of sample}\right) \\
&\quad -m\left(CH_4 \text{ displaced by sample}\right) - m\left(\text{displaced by adsorbed film}\right)
\end{aligned} \tag{C.7}
$$

$$m\left(CH_4 \text{ in chamber in absence of sample}\right) = m_{C,M} - m_C \tag{C.8}$$

$$m\left(CH_4 \text{ displaced by sample}\right) = V_S \rho_{CH_4} \tag{C.9}$$

$$m\left(\text{displaced by adsorbed film}\right) = V_{ads} \rho_{CH_4} \tag{C.10}$$

or,

$$m\left(\text{displaced by adsorbed film}\right) = V_{Nanopore} \rho_{CH_4} \tag{C.11}$$

using eq. (C.10) gives,

$$m\left("\text{supernatant}"CH_4\right) = m_{C,M} - m_C - V_S \rho_{CH_4} - V_{ads} \rho_{CH_4} \tag{C.12}$$

125

therefore,

$$m_{ads} = m_{C,S,M} - m_{C,S} - \left[m_{C,M} - m_C - V_S \rho_{CH_4} - V_{ads} \rho_{CH_4} \right] \qquad \text{(C.13)}$$

combined with eq. (C.1) and eq. (C.3),

$$m_{ads} = m_{C,S,M} - m_{C,S} - \left[m_{C,M} - m_C - \frac{\left(m_{C,S} - m_C \right)}{\rho_S} \rho_{CH_4} - \frac{m_{ads}}{\rho_{ads}} \rho_{CH_4} \right] \qquad \text{(C.14)}$$

therefore,

$$m_{ads} \left(1 - \frac{\rho_{CH_4}}{\rho_{ads}} \right) = m_{C,S,M} - m_{C,S} - m_{C,M} + m_C + \left(m_{C,S} - m_C \right) \frac{\rho_{CH_4}}{\rho_S} \qquad \text{(C.15)}$$

solving for m_{ads},

$$m_{ads} = \frac{m_{C,S,M} - m_{C,M} - \left(m_{C,S} - m_C \right) \left(1 - \dfrac{\rho_{CH_4}}{\rho_S} \right)}{\left(1 - \dfrac{\rho_{CH_4}}{\rho_{ads}} \right)} \qquad \text{(C.16)}$$

therefore,

$$m_{ads} = \left(m_{C,S,M} - m_{C,M} \right) \left(1 - \frac{\rho_{CH_4}}{\rho_{ads}} \right)^{-1} - \left(m_{C,S} - m_C \right) \left(1 - \frac{\rho_{CH_4}}{\rho_S} \right) \left(1 - \frac{\rho_{CH_4}}{\rho_{ads}} \right)^{-1} \qquad \text{(C.17)}$$

now,

$$m_{ads} \Big/ m_S = \frac{\left(m_{C,S,M} - m_{C,M} \right) - \left(m_{C,S} - m_C \right) \left(1 - \dfrac{\rho_{CH_4}}{\rho_S} \right)}{\left(m_{C,S} - m_C \right) \left(1 - \dfrac{\rho_{CH_4}}{\rho_{ads}} \right)} \qquad \text{(C.18)}$$

now we estimate that the volume of adsorbed methane is the same as the nanopores volume, therefore solve using eq. (C.11) instead of eq. (C.10),

$$m\left("\text{supernatant}"CH_4\right) = m_{C,M} - m_C - V_S\rho_{CH_4} - V_{Nanopore}\rho_{CH_4} \tag{C.19}$$

therefore,

$$m_{ads} = m_{C,S,M} - m_{C,S} - \left[m_{C,M} - m_C - V_S\rho_{CH_4} - V_{Nanopore}\rho_{CH_4} \right] \tag{C.20}$$

combined with eq. (C.1),

$$m_{ads} = m_{C,S,M} - m_{C,S} - \left[m_{C,M} - m_C - \left(\frac{\left(m_{C,S} - m_C\right)}{\rho_S} + V_{Nanopore} \right)\rho_{CH_4} \right] \tag{C.21}$$

therefore,

$$m_{ads} = m_{C,S,M} - m_{C,S} - m_{C,M} + m_C + \left(m_{C,S} - m_C\right)\frac{\rho_{CH_4}}{\rho_S} + V_{Nanopore}\rho_{CH_4} \tag{C.22}$$

or,

$$m_{ads} = m_{C,S,M} - m_{C,M} - \left(m_{C,S} - m_C\right)\left(1 - \frac{\rho_{CH_4}}{\rho_S}\right) + V_{Nanopore}\rho_{CH_4} \tag{C.23}$$

now,

$$m_{ads}\Big/m_S = \frac{m_{C,S,M} - m_{C,M} - \left(m_{C,S} - m_C\right)\left(1 - \frac{\rho_{CH_4}}{\rho_S}\right) + V_{Nanopore}\rho_{CH_4}}{\left(m_{C,S} - m_C\right)} \tag{C.24}$$

Now find m_{ads}^e:

$$m_{ads}^e = m(adsorbed\ methane) - m(methane\ displaced\ by\ adsorbed\ film) \quad (C.25)$$

$m_{ads}^e = $ -

using eq. (C.23),

$$m_{ads}^e = m_{C,S,M} - m_{C,M} - \left(m_{C,S} - m_C\right)\left(1 - \frac{\rho_{CH_4}}{\rho_S}\right) + V_{Nanopore}\rho_{CH_4} - V_{Nanopore}\rho_{CH_4} \quad (C.26)$$

therefore,

$$m_{ads}^e = m_{C,S,M} - m_{C,M} - \left(m_{C,S} - m_C\right)\left(1 - \frac{\rho_{CH_4}}{\rho_S}\right) \quad (C.27)$$

now m_{ads}^e / m_S,

$$m_{ads}^e / m_S = \frac{m_{C,S,M} - m_{C,M} - \left(m_{C,S} - m_C\right)\left(1 - \frac{\rho_{CH_4}}{\rho_S}\right)}{\left(m_{C,S} - m_C\right)} \quad (C.28)$$

Now find m_{ST}:

$$m_{ST} = m(CH_4\ adsorbed) + m(CH_4\ in\ large\ pores) \quad (C.29)$$
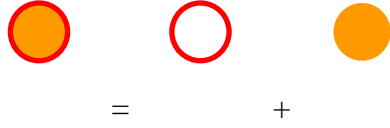
$$m_{ST} = m_{ads} + \left(V_{All\ Pores} - V_{Nanopore}\right)\rho_{CH_4} \qquad (C.30)$$

using eq. (C.20),

$$m_{ST} = m_{C,S,M} - m_{C,S} - m_{C,M} + m_C + V_S\rho_{CH_4} + V_{Nanopore}\rho_{CH_4} + \left(V_{All\ Pores} - V_{Nanopore}\right)\rho_{CH_4} \quad (C.31)$$

therefore,

$$m_{ST} = m_{C,S,M} - m_{C,S} - m_{C,M} + m_C + V_S\rho_{CH_4} + V_{All\ Pores}\rho_{CH_4} \qquad (C.32)$$

using eq. (C.2),

$$m_{ST} = m_{C,S,M} - m_{C,S} - m_{C,M} + m_C + \frac{\left(m_{C,S} - m_C\right)}{\rho_P}\rho_{CH_4} \qquad (C.33)$$

or,

$$m_{ST} = m_{C,S,M} - m_{C,M} - \left(m_{C,S} - m_C\right)\left(1 - \frac{\rho_{CH_4}}{\rho_P}\right) \qquad (C.34)$$

now,

$$m_{ST}\Big/m_S = \frac{m_{C,S,M} - m_{C,M} - \left(m_{C,S} - m_C\right)\left(1 - \dfrac{\rho_{CH_4}}{\rho_P}\right)}{\left(m_{C,S} - m_C\right)} \qquad (C.35)$$

now,

$$\rho_{ST} = \frac{m_{ST}}{V_P} \qquad (C.36)$$

129

using eq. (C.2),

$$\rho_{ST} = \frac{m_{ST}\rho_P}{\left(m_{C,S} - m_C\right)} \tag{C.37}$$

or, combined with eq. (C.34)

$$\rho_{ST} = \frac{\left[m_{C,S,M} - m_{C,M} - \left(m_{C,S} - m_C\right)\left(1 - \dfrac{\rho_{CH_4}}{\rho_P}\right)\right]\rho_P}{\left(m_{C,S} - m_C\right)} \tag{C.38}$$

Conversion of $m_{ads}^e \big/ m$ to $m_{ads} \big/ m_S$ using $V_{Nanopore}$

from eqs. (C.23) and (C.27),

$$m_{ads} - m_{ads}^e = m_{C,S,M} - m_{C,M} - \left(m_{C,S} - m_C\right)\left(1 - \frac{\rho_{CH_4}}{\rho_S}\right) + V_{Nanopore}\rho_{CH_4}$$

$$- \left[m_{C,S,M} - m_{C,M} - \left(m_{C,S} - m_C\right)\left(1 - \frac{\rho_{CH_4}}{\rho_S}\right)\right] \tag{C.39}$$

therefore,

$$\frac{m_{ads}}{m_S} - \frac{m_{ads}^e}{m_S} = \frac{V_{Nanopore}\rho_{CH_4}}{m_S} \tag{C.40}$$

now, from eqs. (C.1) and (C.2),

$$m_S = V_S\rho_S = \left(V_{AllPores} + V_S\right)\rho_P \tag{C.41}$$

solving for V_S,

130

$$V_S = \frac{V_{AllPores}\rho_P}{(\rho_S - \rho_P)} = \frac{V_{AllPores}}{\left(\dfrac{\rho_S}{\rho_P} - 1\right)} \tag{C.42}$$

and,

$$m_S = \frac{V_{AllPores}\rho_S}{\left(\dfrac{\rho_S}{\rho_P} - 1\right)} = \frac{V_{AllPores}}{\left(\dfrac{1}{\rho_P} - \dfrac{1}{\rho_S}\right)} \tag{C.43}$$

now, eq. (C.40)

$$\left. m_{ads} \middle/ m_S \right. = \left. m_{ads}^e \middle/ m_S \right. + \frac{V_{Nanopore}}{V_{AllPores}}\rho_{CH_4}\left(\frac{1}{\rho_P} - \frac{1}{\rho_S}\right) \tag{C.44}$$

Conversion of $\left. m_{ads}^e \middle/ m_S \right.$ to $\left. m_{ads} \middle/ m_S \right.$ using ρ_{ads}

combining eqs. (C.18) and (C.28) gives,

$$\left. m_{ads} \middle/ m_S \right. = \left. m_{ads}^e \middle/ m_S \right. \left(1 - \frac{\rho_{CH_4}}{\rho_{ads}}\right)^{-1} \tag{C.45}$$

Now let's find ρ_{ads} and $V_{Nanopore}$ from these equations,

from eqs. (C.44) and (C.45),

$$\left. m_{ads}^e \middle/ m_S \right. \left(1 - \frac{\rho_{CH_4}}{\rho_{ads}}\right)^{-1} = \left. m_{ads}^e \middle/ m_S \right. + \frac{V_{Nanopore}}{V_{AllPores}}\rho_{CH_4}\left(\frac{1}{\rho_P} - \frac{1}{\rho_S}\right) \tag{C.46}$$

which becomes

$$m^e_{ads}\Big/m_S = m^e_{ads}\Big/m_S + \frac{V_{Nanopore}}{V_{AllPores}}\rho_{CH_4}\left(\frac{1}{\rho_P}-\frac{1}{\rho_S}\right) - \frac{\rho_{CH_4}}{\rho_{ads}}\left[m^e_{ads}\Big/m_S + \frac{V_{Nanopore}}{V_{AllPores}}\rho_{CH_4}\left(\frac{1}{\rho_P}-\frac{1}{\rho_S}\right)\right] \quad \text{(C.47)}$$

becomes,

$$\frac{V_{Nanopore}}{V_{AllPores}}\left(\frac{1}{\rho_P}-\frac{1}{\rho_S}\right) = \frac{1}{\rho_{ads}}\left[m^e_{ads}\Big/m_S + \frac{V_{Nanopore}}{V_{AllPores}}\rho_{CH_4}\left(\frac{1}{\rho_P}-\frac{1}{\rho_S}\right)\right] \quad \text{(C.48)}$$

solving for ρ_{ads},

$$\rho_{ads} = \frac{\left[m^e_{ads}\Big/m_S + \frac{V_{Nanopore}}{V_{AllPores}}\rho_{CH_4}\left(\frac{1}{\rho_P}-\frac{1}{\rho_S}\right)\right]}{\frac{V_{Nanopore}}{V_{AllPores}}\left(\frac{1}{\rho_P}-\frac{1}{\rho_S}\right)} \quad \text{(C.49)}$$

$$\rho_{ads} = \rho_{CH_4} + m^e_{ads}\Big/m_S \frac{V_{AllPores}}{V_{Nanopore}}\left(\frac{1}{\rho_P}-\frac{1}{\rho_S}\right)^{-1} \quad \text{(C.50)}$$

solving for $V_{Nanopore}$,

$$V_{Nanopore} = m^e_{ads}\Big/m_S \frac{V_{AllPores}}{\rho_{ads}-\rho_{CH_4}}\left(\frac{1}{\rho_P}-\frac{1}{\rho_S}\right)^{-1} \quad \text{(C.51)}$$

Finally we will also determine how to convert $m^e_{ads}\Big/m_S$ to $m_{ST}\Big/m_S$:

Taking equation (C.28) and subtracting equation (C.35) gives,

$$\frac{m^e_{ads}}{m_S} - \frac{m_{ST}}{m_S} = \frac{\left(m_{C,S} - m_C\right)\left(\dfrac{\rho_{CH_4}}{\rho_S} - \dfrac{\rho_{CH_4}}{\rho_P}\right)}{\left(m_{C,S} - m_C\right)} \tag{C.52}$$

which becomes,

$$\frac{m^e_{ads}}{m_S} = \frac{m_{ST}}{m_S} + \left(\frac{\rho_{CH_4}}{\rho_S} - \frac{\rho_{CH_4}}{\rho_P}\right) \tag{C.53}$$

or,

$$\frac{m_{ST}}{m_S} = \frac{m^e_{ads}}{m_S} + \rho_{CH_4}\left(\frac{1}{\rho_P} - \frac{1}{\rho_S}\right) \tag{C.54}$$

133

Appendix D: Processing of Manometric Data

The test fixture has the following two states during the experiment.

Initially the storage tank is at a pressure about 2 times the desired final pressure [i.e. 1000 psi for a desired final pressure of 500 psi]. The test tank is under vacuum.
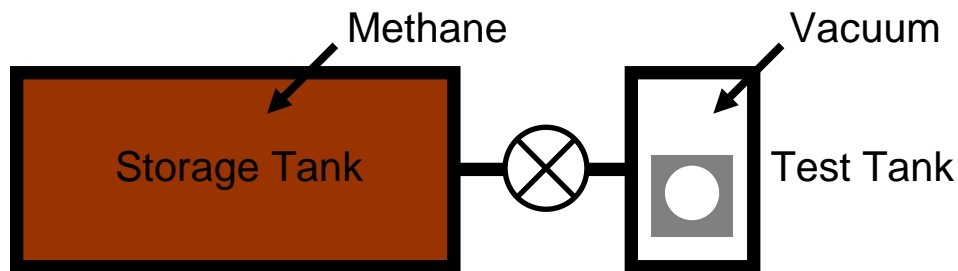
Then the valve is opened and the storage tank pressure drops as the methane is released into the test tank. The final pressure for the storage tank is still higher than that of the test tank. The methane in the test tank includes methane both in the surrounding dead space as well as bulk gas in the pores and adsorbed.
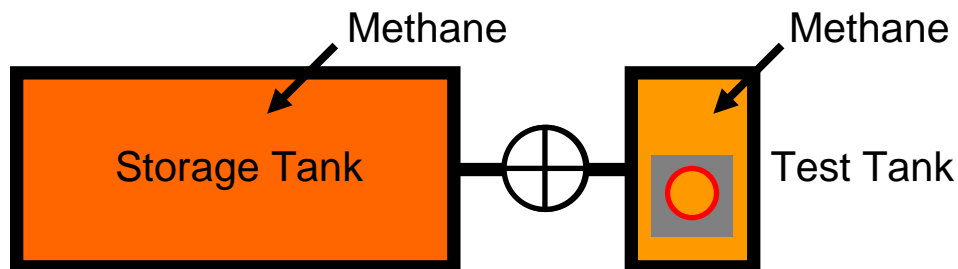
The following values are measured during the experiment:

$P_{Initial}^{ST}$: Initial pressure for storage tank.

$P_{Initial}^{TT}$: Initial pressure for the test tank [assumed to be zero].

134

P_{Final}^{ST} : Final pressure for storage tank.

P_{Final}^{TT} : Final pressure for the test tank.

$m^{Briquette}$: Mass of briquette.

$V^{Briquette}$: Volume of briquette.

T : Temperature of system.

The following values are assumed as known:

V^{ST} : Volume of storage tank.

- Determined experimentally to be $2275.25 \ cm^3$.

V^{TT} : Volume of test tank.

- Determined experimentally to be $589.45 \ cm^3$.

$\rho_{Initial}^{ST} = \rho_{Initial}^{ST}\left(P_{Initial}^{ST}, T\right)$: Density of methane in storage tank initially.

- Density is a function of the measured pressure, $P_{Initial}^{ST}$, and the temperature, T.

- Values are taken from NIST tables.

$\rho_{Initial}^{TT} = 0$: Density of methane in test tank initially.

- Value taken to be zero.

$\rho_{Final}^{ST} = \rho_{Final}^{ST}\left(P_{Final}^{ST}, T\right)$: Density of methane in storage tank finally.

- Density is a function of the measured pressure, P_{Final}^{ST}, and the temperature, T.

- Values are taken from NIST tables.

$\rho_{Final}^{TT} = \rho_{Final}^{TT}\left(P_{TT}^{TT}, T\right)$: Density of methane in test tank finally.

- Density is a function of the measured pressure, P_{Final}^{TT}, and the temperature, T.

- Values are taken from NIST tables.

ρ_S : Skeletal density of sample (no pores included).

- Value for amorphous carbon is $2\ {}^g\!/_{cm^3}$.

ρ_P : Piece density of sample (all pores included).

- Values taken from table or use $0.500\ {}^g\!/_{cm^3}$ to be a good estimate.

The value that is directly measured by the experiment is the amount stored in both adsorbed and non-adsorbed phases, m_{ST} .

The mass of methane initially in the storage tank is given by,

$$m_{Initial}^{ST} = \rho_{Initial}^{ST} V^{ST} \tag{D.1}$$

The mass of methane finally in the storage tank is given by,

$$m_{Final}^{ST} = \rho_{Final}^{ST} V^{ST} \tag{D.2}$$

Therefore the total amount of mass of methane given to the test tank during the experiment is given by the difference of these two,

$$m_{Final}^{TT} = \rho_{Initial}^{ST} V^{ST} - \rho_{Final}^{ST} V^{ST} \tag{D.3}$$

This mass, however includes methane not only in the briquette, but also in the dead space surrounding it, i.e.
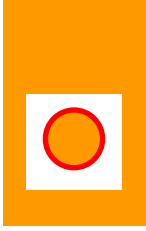
So we want to subtract the mass of methane that is not in the briquette. Since we know the total volume of the briquette and the total volume of the test tank, we can find this mass.

$$m_{Final}^{DeadSpace} = \rho_{Final}^{TT} \left(V^{TT} - V^{Briquette} \right) \tag{D.4}$$

So the amount of methane stored in the briquette is given by,
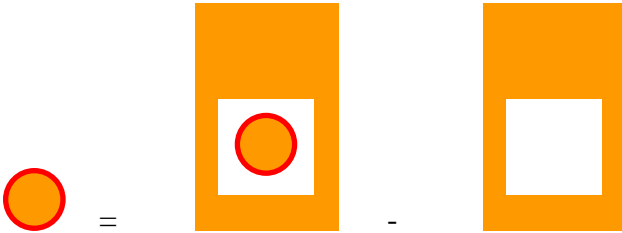
$$m_{ST} = m_{Final}^{TT} - m_{Final}^{DeadSpace} \tag{D.5}$$

Which gives,

$$m_{ST} = V^{ST} \left(\rho_{Initial}^{ST} - \rho_{Final}^{ST} \right) - \rho_{Final}^{TT} \left(V^{TT} - V^{Briquette} \right) \tag{D.6}$$

Or, more formally, to emphasize the densities dependence on pressure and temperature,

$$m_{ST} = V^{ST} \left(\rho_{Initial}^{ST} \left(P_{Initial}^{ST}, T \right) - \rho_{Final}^{ST} \left(P_{Final}^{ST}, T \right) \right) - \rho_{Final}^{TT} \left(P_{Final}^{TT}, T \right) \left(V^{TT} - V^{Briquette} \right) \tag{D.7}$$

137

Appendix E: Hydrogen Test Fixture Procedure
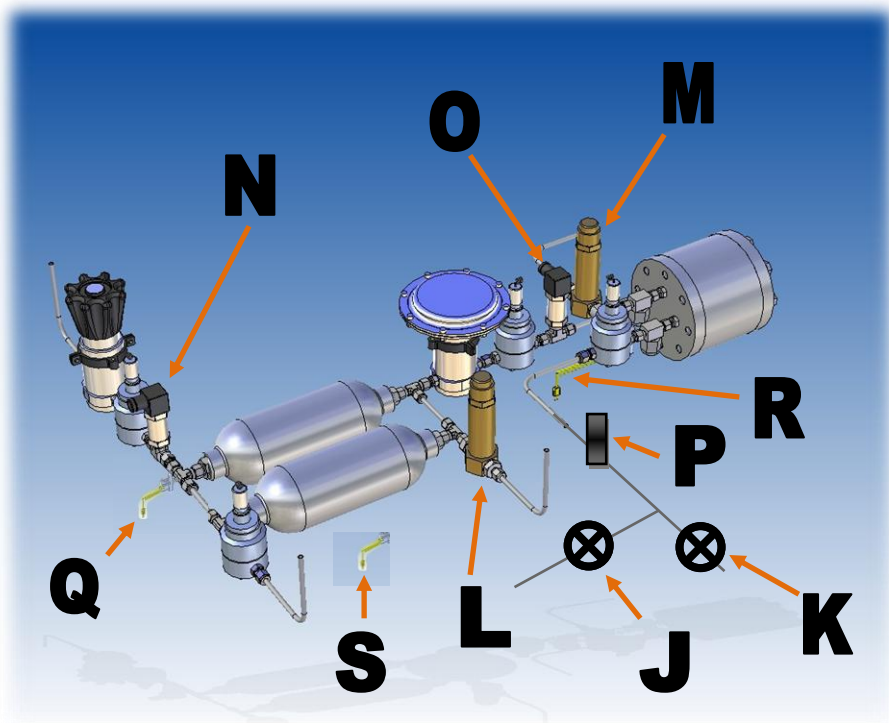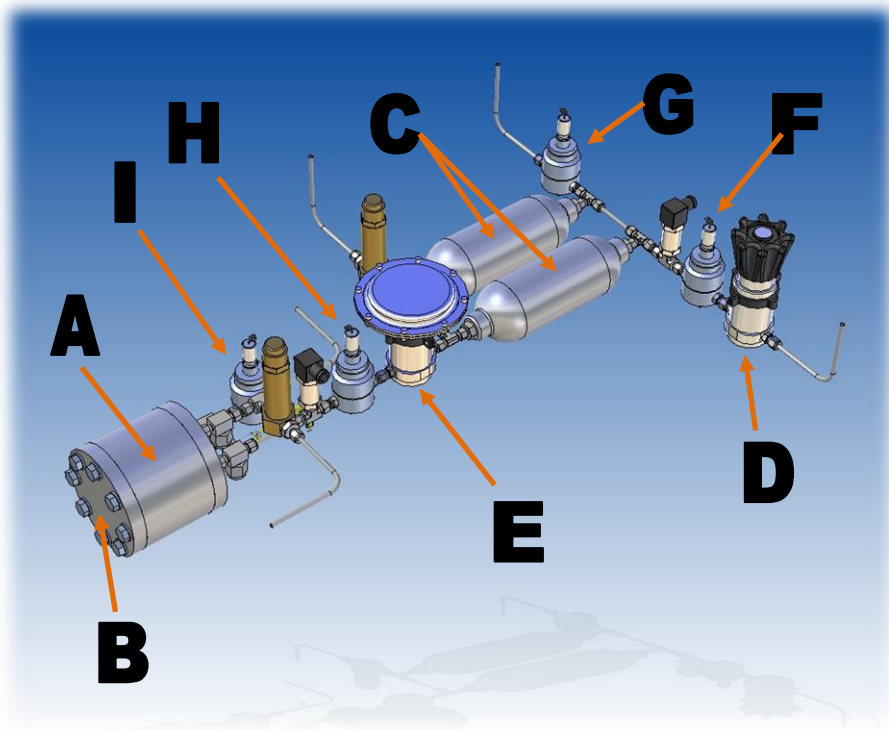
A) Sample Tank
B) Sample Tank Face-plate
C) Supply Tanks
D) Main-line Regulator
E) System Regulator
F) Main-line Valve
G) Supply-side Bleeder Valve
H) System Valve
I) Sample-side Bleeder Valve
J) Vacuum Valve
K) Vent Valve
L) Supply-side Relief Valve
M) Sample-side Relief Valve
N) Supply-side Pressure Transducer
O) Sample-side Pressure Transducer
P) Vacuum Pressure Transducer
Q) Supply-side Thermocouple
R) Sample-side Thermocouple
S) External Thermocouple

During the entire experimental procedure, the values from all the pressure transducers [N, O, P] and the thermocouples [Q, R, S] needs to be recorded to a text file. At certain steps it would be useful to have it insert text [e.g. Supply-side pressurization begins, Supply-side equilibrated, etc…]. When the adsorption begins, we need the pressure and temperature values written to a excel file. These are simple suggestions and I assume that as we use the set-up repeatedly we may need to change the program as it seems fit.

The following will have LabVIEW® control/acquire data from: E, F, H, I, N, O, P, Q, R, and S

The following will be controlled manually: D, G, J, and K

In the steps below [Manual] refers to physically adjusting a regulator or valve, [LabVIEW®] refers to a LabVIEW® program controlled action, [LabVIEW® Manual] refers to the operator using a LabVIEW® control to open a valve

System Start-up and Sample Exchange

1. All valves and regulators start fully-closed

2. Remove briquette from transfer fixture [not shown]

3. Remove *Sample Tank Face-plate [B]*

4. Place briquette in *Sample Tank [A]*

5. Put *Sample Tank Face-plate* back on using 10 bolts. Remember to tighten in a star pattern.

6. Evacuate *Sample Tank*

   6.1. Open *Sample-side Bleeder Valve [I]* [LabVIEW® Manual]

   6.2. Open *Vacuum Valve [J]* [Manual]

139

6.3. Turn on Vacuum

6.4. Read out pressure from *Vacuum Pressure Transducer [P]* [LabVIEW®]

6.5. Evacuate Sample Tank for a set amount of time [e.g. 15-30 minutes]

6.6. Close *Sample-side Bleeder Valve [*LabVIEW® Manual] and *Vacuum Valve* [Manual]

7. Open *Vent Valve* [Manual]

Typical 50 bar [~700 psig] measurement

See end of document for modifications to procedure for full isotherm

8. Open *Main-line Valve* [F] [LabVIEW®]

9. Read out pressure from *Supply-side Pressure Transducer* [N] [LabVIEW®]

10. Adjust *Main-line Regulator* [D] [Manual] until pressure reads out at 100 bar [~1500 psig]

11. Close *Main-line Valve* [LabVIEW®]

12. Wait until the pressure stabilizes and the temperatures from the *Supply-side Thermocouple* [Q] [LabVIEW®] and the *External Thermocouple* [S] [LabVIEW®] are equal [~30 minutes]

13. Open *System Valve* [H] [LabVIEW®]

14. Read out pressure from *Sample-side Pressure Transducer* [O] [LabVIEW®]

15. Record pressure [LabVIEW®] from *Sample-side Pressure Transducer* and *Supply-side Pressure Transducer* for uptake calculation purposes

16. Increase *Sample Tank* pressure to 50 bar using *System Regulator* [E] [LabVIEW®]

17. Maintain 50 bar using *System Regulator* [it will need to be adjusted as the pressure in the *Supply Tanks* [C] drops]

18. Wait for equilibration in both pressure [*Supply-side Pressure Transducer, Sample-side Pressure Transducer*] and temperature [*Supply-side Thermocouple, Sample-side Thermocouple, External Thermocouple*] [1-2 hours]

19. Calculate the uptake

20. Close the *System Valve* and the *System Regulator* [LabVIEW®]

21. Open the *Sample-side Bleeder Valve* [LabVIEW®]

22. The *Vent Valve* should be open from step 7

23. Allow pressure in *Sample Tank* to drop to just above atmospheric pressure [i.e. 2 bar or ~15 psig]

24. Close *Sample-side Bleeder Valve* [LabVIEW®]

25. Simultaneous to Step 21, open *Main-line Valve* [LabVIEW®]

26. *Main-line Regulator* should still be adjusted for the *Supply Tanks* to come to ~100 bar

27. Repeat steps 11-25 for as many data points as is desired

28. The last time this is repeated stop at step 19

29. Open the *Sample-side Bleeder Valve* and allow the *Supply-side Tanks* to reach near atmospheric pressure [2 bar] [LabVIEW®] [this may not be necessary every time unless the supply-side equipment cannot handle long periods of high pressure (e.g. 75 bar)]

30. Close the *System Valve* and *System Regulator* [LabVIEW®]

31. Allow pressure in *Sample Tank* to come to atmosphere

32. LabVIEW® closes all of the valves/regulators it has control of

33. Operator closes all manual valves/regulators

34. Remove **Sample Face-plate**

35. Remove briquette

36. Place briquette back in transfer vessel

37. Put **Sample Face-plate** back on

For a full isotherm, follow the same steps above, but instead of starting out at 50 bar, it will start at the lowest pressure desired for the isotherm [e.g. 7 bar]

When the above procedure repeats for multiple measurements, now simply increase the pressure in the **Sample Tank** using the **System Regulator** to the next desired pressure [e.g. 14 bar] [**Supply Tanks** do not need to be refilled]. This repeats until the final pressure and then it follows the same steps 29-37

Appendix F: Buoyancy Corrections

[† denotes values not corrected for buoyancy]

Mass of the cell before outgassing: $M_C^{\text{pre-outgas}}$

Mass of the cell after outgassing: $M_C^{\dagger}$

Mass of cell and 500 psig methane: $M_{C,M}^{\dagger}$

Mass of cell and sample before outgassing: $M_{C,S}^{\dagger\,\text{pre-outgas}}$

[Note: you cannot use this the same way as $M_C^{\text{pre-outgas}}$ because the amount of water in

sample is non-negligible]

Mass of cell and sample after outgassing: $M_{C,S}^{\dagger}$

Mass of cell, sample and methane [bulk and adsorbed]: $M_{C,S,M}^{\dagger}$

Density of methane at 500 psig: $\rho_{CH_4} = 0.024839 \; {}^{g}\!/\!_{ml}$

Density of stainless steel: $\rho_{SS} = 8.0 \; {}^{g}\!/\!_{ml}$

Density of air: $\rho_{Air} = 0.0011922 \; {}^{g}\!/\!_{ml}$

Skeletal density of carbon: $\rho_S = 2.0 \; {}^{g}\!/\!_{ml}$

Effective particle density of carbon: $\rho_{EP} = 0.5 \; {}^{g}\!/\!_{ml}$

Internal volume of sample cell: $V_{IC} = 23 \; ml$

We have the equation for buoyancy corrections

$$M = M^{\dagger} \frac{\left(1 - \rho_{Air} / \rho_{Cal}\right)}{\left(1 - \rho_{Air} / \rho\right)} \tag{F.1}$$

Where ρ_{Cal} is the density of the calibration mass, which will be taken as the density of stainless steel, and ρ is the density of the object being weighed.

Mass of the cell after outgassing: M_C

We begin by assuming the density of the sample cell is that of stainless steel. This is still only an approximation because this density should actually include the density of the glass wool, plastic valve knob, etc…

Therefore we can calculate the volume of the solid part of the cell as

$$V_{SS} = \frac{M_C^{\text{pre-outgas}}}{\rho_{SS}} \tag{F.2}$$

Now we can add the internal volume of the cell to get the total cell volume and assuming that there is a perfect vacuum

$$V_C = V_{SS} + V_{IC}$$
$$\rho_C = \frac{M_C^{\text{pre-outgas}}}{V_C} \tag{F.3}$$

Equations (F.2) and (F.3) give

$$\rho_C = \frac{1}{\dfrac{1}{\rho_{SS}} + \dfrac{V_{IC}}{M_C^{\text{pre-outgas}}}} \tag{F.4}$$

Now with equation (F.1)

144

$$M_C = M_C^\dagger \frac{\left(1 - \rho_{Air}\middle/\rho_{Cal}\right)}{\left(1 - \rho_{Air}\left[\frac{1}{\rho_{SS}} + \frac{V_{IC}}{M_C^{\text{pre-outgas}}}\right]\right)} \tag{F.5}$$

Excess Mass Adsorbed Buoyancy Correction

The equation for excess mass adsorbed is given by [from Jacob and Peter's write-up]

$$M_{Adsorbed}^{Excess} = M_{C,S,M} - M_{C,M} - \left(M_{C,S} - M_C\right)\left(1 - \frac{\rho_{CH_4}}{\rho_S}\right) \tag{F.6}$$

Modify equation (F.1) using the fact that we know the total volume of the cell

$$M = M^\dagger\left(1 - \rho_{Air}\middle/\rho_{SS}\right) + \rho_{Air}V_C \tag{F.7}$$

Using equation (F.7) to correct the masses in equation (F.6)

$$M_{Adsorbed}^{Excess} = \left[M_{C,S,M}^\dagger - M_{C,M}^\dagger - \left(M_{C,S}^\dagger - M_C^\dagger\right)\left(1 - \frac{\rho_{CH_4}}{\rho_S}\right)\right]\left(1 - \rho_{Air}\middle/\rho_{SS}\right) \tag{F.8}$$

where

$$\rho_{Air}\middle/\rho_{SS} \cong 0.000149 \tag{F.9}$$

A typical value for $M_{Adsorbed}^{Excess}{}^\dagger$ for methane is 0.8 grams; the correction to this value is

0.00012 grams

A buoyancy correction this small is negligible compared to the uncertainty from the

balance of ~0.004 grams.

Therefore it is my conclusion that buoyancy corrections are not sizeable compared to the

end result or the uncertainties inherent in the experiment and can therefore be neglected.

References

1. *U.S. Department of Energy*. 2008 [cited 2008 November 24]; Available from: http://www.energy.gov/.
2. Brownstone, D., D.S. Bunch, and K. Train, *Joint mixed logit models of stated and revealed preferences for alternative-fuel vehicles.* Transportation Research Part B, 2000. **34**(5): p. 315-338.
3. Olson, T., M. Addy, and D. Schwyzer, *State Alternative Fuels Plan*, California Air Resources Board and California Energy Commission, Editor. 2007: Sacremento, CA.
4. Addy, M., P. Ward, and J. Wiens, *AB1007 State Alternative Fuels Plan: Natural Gas Scenario*, California Energy Commission and California Air Resources Board, Editor. 2007: Sacramento, CA.
5. *Hydrogen Posture Plan-An Integrated Research, Development and Demonstration Plan*, U.S. Department of Energy and U.S. Department of Transportation, Editor. 2006: Washington D.C.
6. *2007 Annual Energy Review*. 2008, Energy Information Administration.
7. Satyapal, S., J. Petrovic, C. Read, G. Thomas, and G. Ordaz, *The US Department of Energy's National Hydrogen Storage Project: Progress towards meeting hydrogen-powered vehicle requirements.* Catalysis Today, 2007. **120**(3-4): p. 246-256.
8. Bhatia, S.K. and A.L. Myers, *Optimum Conditions for Adsorptive Storage.* Langmuir, 2006. **22**(4): p. 1688-1700.
9. Patchkovskii, S., J.S. Tse, S.N. Yurchenko, L. Zhechkov, T. Heine, and G. Seifert, *Graphene nanostructures as tunable storage media for molecular hydrogen.* Proceedings of the National Academy of Sciences, 2005. **102**(30): p. 10439-10444.
10. Gigras, A., S.K. Bhatia, A.V. Anil Kumar, and A.L. Myers, *Feasibility of tailoring for high isosteric heat to improve effectiveness of hydrogen storage in carbons.* Carbon, 2007. **45**(5): p. 1043-1050.
11. Keller, J.U. and R. Staudt, *Gas Adsorption Equilibria: Experimental Methods And Adsorptive Isotherms*. 2005: Springer.
12. Düren, T., L. Sarkisov, O.M. Yaghi, and R.Q. Snurr, *Design of New Materials for Methane Storage.* Science, 2001. **291**: p. 1021.
13. Eddaoudi, M., et al., *Systematic Design of Pore Size and Functionality in Isoreticular MOFs and Their Application in Methane Storage.* Science, 2002. **295**(5554): p. 469-472.
14. Ginzburg, Y. *ANG Storage as a Technological Solution for the 'Chicken-and-Egg' Problem of NGV Refueling Infrastructure Development.* in *23rd World Gas Conference*. 2006. Amsterdam: Internation Gas Union.
15. Ma, S., D. Sun, J.M. Simmons, C.D. Collier, D. Yuan, and H.C. Zhou, *Metal-Organic Framework from an Anthracene Derivative Containing Nanoscopic*

Cages Exhibiting High Methane Uptake. J. Am. Chem. Soc, 2008. **130**(3): p. 1012-1016.

16. *2009 Annual Energy Review*. 2009, Energy Information Administration.

17. Cracknell, R.F., P. Gordon, and K.E. Gubbins, *Influence of pore geometry on the design of microporous materials for methane storage.* The Journal of Physical Chemistry, 1993. **97**(2): p. 494-499.

18. Lozano-Castelló, D., D. Cazorla-Amorós, A. Linares-Solano, and D.F. Quinn, *Activated carbon monoliths for methane storage: influence of binder.* Carbon, 2002. **40**(15): p. 2817-2825.

19. Perrin, A., A. Celzard, A. Albiniak, J. Kaczmarczyk, J.F. Marêché, and G. Furdin, *NaOH activation of anthracites: effect of temperature on pore textures and methane storage ability.* Carbon, 2004. **42**(14): p. 2855-2866.

20. Molina-Sabio, M., C. Almansa, and F. Rodríguez-Reinoso, *Phosphoric acid activated carbon discs for methane adsorption.* Carbon, 2003. **41**(11): p. 2113-2119.

21. Bénard, P. and R. Chahine, *Determination of the adsorption isotherms of hydrogen on activated carbons above the critical temperature of the adsorbate over wide temperature and pressure ranges.* Langmuir, 2001. **17**(6): p. 1950-1955.

22. Poirier, E., R. Chahine, A. Tessier, and T.K. Bose, *Gravimetric and volumetric approaches adapted for hydrogen sorption measurements with in situ conditioning on small sorbent samples.* Review of Scientific Instruments, 2005. **76**: p. 055101.

23. Ricca, A. and C.W. Bauschlicher Jr, *The physisorption of CH4 on graphite and on a (9,0) carbon nanotube.* Chemical Physics, 2006. **324**(2-3): p. 455-458.

24. Mattera, L., F. Rosatelli, C. Salvo, F. Tommasini, U. Valbusa, and G. Vidali, *Selective adsorption of 1H2 and 2H2 on the (0001) graphite surface.* Surface Science, 1980. **93**(2-3): p. 515-525.

25. Pfeifer, P., et al., *Nearly Space-Filling Fractal Networks of Carbon Nanopores.* Physical Review Letters, 2002. **88**(11): p. 115502.

26. Wennerberg, A.N. and T.M. O'Grady, *Active carbon process and composition.* 1978, US Patent 4,082,694.

27. Hashimoto, K., K. Miura, F. Yoshikawa, and I. Imai, *Change in Pore Structure of Carbonaceous Materials during Activation and Adsorption Performance of Activated Carbon.* Industrial & Engineering Chemistry Process Design and Development, 1979. **18**(1): p. 72-80.

28. Baker, F.S., *Highly microporous carbon.* 1998, US Patent 5,710,092.

29. Otowa, T., Y. Nojima, and T. Miyazaki, *Development of KOH activated high surface area carbon and its application to drinking water purification.* Carbon, 1997. **35**(9): p. 1315-1319.

30. Evans, M.J.B., E. Halliop, and J.A.F. MacDonald, *The production of chemically-activated carbon.* Carbon, 1999. **37**(2): p. 269-274.

31. Guo, J. and A.C. Lua, *Textural and chemical characterisations of activated carbon prepared from oil-palm stone with H2SO4 and KOH impregnation.* Microporous and Mesoporous Materials, 1999. **32**(1-2): p. 111-117.

32.   Molina-Sabio, M. and F. Rodríguez-Reinoso, *Role of chemical activation in the development of carbon porosity.* Colloids and Surfaces A: Physicochemical and Engineering Aspects, 2004. **241**(1-3): p. 15-25.

33.   Rouquerol, F., J. Rouquerol, and K. Sing, *Adsorption by Powders and Porous Solids: Principles, Methodology and Applications*. 1999: Academic Press. New York. US.

34.   Steele, W., *The interaction of gases with solid surfaces*. 1974: Pergamon Press.

35.   Nicholson, D., *Simulation studies of methane transport in model graphite micropores.* Carbon, 1998. **36**(10): p. 1511-1523.

36.   Sing, K.S.W., et al., *Reporting physisorption data for gas/solid systems with special reference to the determination of surface area and porosity.* Pure Appl. Chem, 1985. **57**(4): p. 603–619.

37.   Langmuir, I., *The Adsorption of Gases on Plane Surface of Glass, Mica and Platinum.* Journal of the American Chemical Society, 1918. **40**(9): p. 1361-1403.

38.   Hill, T.L., *An Introduction to Statistical Thermodynamics*. 1986: Courier Dover Publications.

39.   Brunauer, S., P.H. Emmett, and E. Teller, *Adsorption of Gases in Multimolecular Layers.* Journal of the American Chemical Society, 1938. **60**(2): p. 309-319.

40.   Brunauer, S., L.S. Deming, W.E. Deming, and E. Teller, *On a Theory of the van der Waals Adsorption of Gases.* Journal of the American Chemical Society, 1940. **62**(7): p. 1723-1732.

41.   Lowell, S., J. Shields, G. Charalambous, and J. Manzione, *Adsorbate cross-sectional area as a function of the BET C constant.* J. Colloid Interface Sci, 1982. **86**: p. 191–195.

42.   Gelb, L.D., K.E. Gubbins, R. Radhakrishnan, and M. Sliwinska-Bartkowiak, *Phase separation in confined systems.* Rep. Prog. Phys, 1999. **62**: p. 1573–1659.

43.   Dabrowski, A., *Standardization of Methods for Characterizing the Surface Geometry of Solids.* Particle & Particle Systems Characterization, 2003. **20**(5): p. 311.

44.   Ravikovitch, P.I., A. Vishnyakov, R. Russo, and A.V. Neimark, *Unified Approach to Pore Size Characterization of Microporous Carbonaceous Materials from N~ 2, Ar, and CO~ 2 Adsorption Isotherms.* Langmuir, 2000. **16**(5): p. 2311-2320.

45.   Steele, W.A., *The physical interaction of gases with crystalline solids: I. Gas-solid energies and properties of isolated adsorbed atoms.* Surface Science, 1973. **36**(1): p. 317-352.

46.   Ravikovitch, P.I. and A.V. Neimark, *Density functional theory model of adsorption on amorphous and microporous silica materials.* Langmuir, 2006. **22**(26): p. 11171-11179.

47.   Marsh, H. and F. Rodriguez-Reinoso, *Activated Carbon*. 1st ed. 2006, Amsterdam; London: Elsevier.

48.   Myers, A.L. and P.A. Monson, *Adsorption in Porous Materials at High Pressure: Theory and Experiment.* Langmuir, 2002. **18**(26): p. 10261-10273.

49.   Knudsen, M., *Ein absolutes manometer.* Annalen der Physik, 1910. **337**(9).

50. Takaishi, T. and Y. Sensui, *Thermal transpiration effect of hydrogen, rare gases and methane.* Transactions of the Faraday Society, 1963. **59**: p. 2503-2514.

51. Liang, S., *Some Measurements of Thermal Transpiration.* Journal of Applied Physics, 1951. **22**: p. 148.

52. Briant, C., *Hydrogen assisted cracking of type 304 stainless steel.* Metallurgical and Materials Transactions A, 1979. **10**(2): p. 181-189.

53. Rozenak, P., I. Robertson, and H. Birnbaum, *HVEM studies of the effects of hydrogen on the deformation and fracture of AISI type 316 austenitic stainless steel.* ACTA METALL. MATER., 1990. **38**(11): p. 2031-2040.

54. *Thermophysical Properties of Fluid Systems.* 2008 [cited 2008 November 25]; Available from: http://webbook.nist.gov/chemistry/fluid/.

55. Lastoskie, C., K.E. Gubbins, and N. Quirke, *Pore size distribution analysis of microporous carbons: a density functional theory approach.* The Journal of Physical Chemistry, 1993. **97**(18): p. 4786-4796.

56. Burress, J.W., et al., *Hydrogen storage in engineered carbon nanospaces.* Nanotechnology, 2009. **20**(204026).

57. Bruch, L., M. Cole, and E. Zaremba, *Physical Adsorption: Forces and Phenomena. Clarendon.* 1997, Oxford.

58. Yildirim, T. and S. Ciraci, *Titanium-Decorated Carbon Nanotubes as a Potential High-Capacity Hydrogen Storage Medium.* Physical Review Letters, 2005. **94**(17): p. 175501.

59. Zhao, Y., Y.H. Kim, A.C. Dillon, M.J. Heben, and S.B. Zhang, *Hydrogen Storage in Novel Organometallic Buckyballs.* Physical Review Letters, 2005. **94**(15): p. 155504.

60. Ferro, Y., F. Marinelli, A. Allouche, and C. Brosset, *Density functional theory investigation of H adsorption on the basal plane of boron-doped graphite.* The Journal of Chemical Physics, 2003. **118**: p. 5650.

61. Kim, Y.H., Y. Zhao, A. Williamson, M.J. Heben, and S.B. Zhang, *Nondissociative Adsorption of H_ {2} Molecules in Light-Element-Doped Fullerenes.* Physical Review Letters, 2006. **96**(1): p. 16102.

62. Aranovich, G. and M. Donohue, *Determining Surface Areas from Linear Adsorption Isotherms at Supercritical Conditions.* Journal of Colloid And Interface Science, 1997. **194**(2): p. 392-397.

VITA

Jacob Burress was born on April 28, 1983 in Wichita, KS. His undergraduate research was focused on computational studies of linear ion traps for quantum computing. He graduated Summa Cum Laude from Western Illinois University in 2004. He received his Masters of Science from the University of Missouri in 2008 and his PhD in physics from the same university in 2009. As of 2009 he is a National Research Council fellow pursuing research at the National Institute of Standards and Technology Center for Neutron Research.